

CTH-NT-267

December 2012

Development of a reduced-order model  
to investigate  
global/regional/local oscillations in BWRs  
and study of new stability indicators

VICTOR DYKIN AND CHRISTOPHE DEMAZIÈRE



Division of Nuclear Engineering  
Department of Applied Physics  
Chalmers University of Technology  
SE-412 96 Gothenburg, Sweden 2012



## ABSTRACT

This report presents the results of some investigations performed at Chalmers University of Technology within the Nordic Thermal-Hydraulic Network (NORTHNET) in the area of stability of Boiling Water Reactors (BWRs). Such systems are known to possibly become unstable under certain conditions, and thus the characterization of their stability properties is of prime importance. Due to the complexity of the problem at hand, a Reduced-Order Model (ROM) was developed, as an alternative to using three-dimensional solvers. The main advantage of using a ROM is that ROMs represent fast running models aimed at catching in a qualitative manner the physical phenomena of importance. In addition, the relative simplicity of ROMs compared with three-dimensional solvers leads to the possibility of providing some physical insight into the stability mechanisms. The ROM developed in this project is unique since it has the ability to model global, regional, and local oscillations, and it is based on four heated channels. The four heated channels are necessary to properly represent the possible excitation of the two first azimuthal modes in case of regional oscillations. A careful examination of the ROM demonstrated that the stability behavior of the system is entirely defined by so-called  $C_{mn}$ -coefficients (assuming that there is no pure density wave oscillation). These coefficients represent the effect of a change of the void fraction on pairs of eigenmodes of the nuclear core. When these coefficients are positive, the system is clearly unstable because of the corresponding positive void feedback. When negative, it was demonstrated, both using the developed ROM and SIMULATE-3K, that the system becomes less stable for  $C_{mn}$  coefficients becoming more negative. A closer examination of the dependence of the Decay Ratio (DR) on the  $C_{mn}$  coefficients using the ROM also demonstrated that for small negative values of the coefficients, a non-monotonic relationship between the DR and the  $C_{mn}$  coefficients exists. Nevertheless, for realistic values of the void reactivity feedback, such a non-monotonic behavior cannot be noticed, because the  $C_{mn}$  coefficients are sufficiently negative. As a consequence, the estimation of the  $C_{mn}$  coefficients opens up the possibility of using such coefficients as a qualitative measure of core stability in a predictive manner. This could be used for instance as a means to compare the relative stability of several core loadings without the need of running lengthy time-dependent three-dimensional core calculations, and could be of great help to nuclear engineers when designing cores.

*Keywords:* boiling water reactor stability, decay ratio, space-dependent neutron noise, reduced order models, density wave oscillations



# Contents

List of publications	1
<b>1 INTRODUCTION</b>	<b>3</b>
<b>2 DEVELOPMENT OF A NUMERICAL TOOL FOR ESTIMATING NEUTRONIC RESPONSES TO GLOBAL/REGIONAL/LOCAL OSCILLATIONS</b>	<b>5</b>
2.1 Description of the neutronic models . . . . .	5
2.1.1 Neutron transport modelling . . . . .	5
2.1.2 Algorithm used for the spatial discretisation . . . . .	7
2.2 Modelling of static core configurations . . . . .	10
2.2.1 Subcritical systems with source . . . . .	10
2.2.2 Critical systems . . . . .	13
2.3 Modelling of dynamic core configurations . . . . .	19
2.3.1 Subcritical systems with source . . . . .	19
2.3.2 Critical systems . . . . .	20
2.4 Use and demonstration of the tool . . . . .	24
<b>3 MODELING OF GLOBAL AND REGIONAL INSTABILITIES VIA ROM</b>	<b>27</b>
3.1 Neutron kinetic model . . . . .	27
3.2 Heat transfer model . . . . .	29
3.3 Thermo-hydraulic model . . . . .	30
3.3.1 Single-phase region . . . . .	30
3.3.2 Two-phase region . . . . .	31
3.4 ROM modifications . . . . .	31
3.4.1 Adjustment of the homogeneous equilibrium model to a higher order model (drift flux model) . . . . .	32
3.4.2 Introduction of a non-uniform power profile . . . . .	33
3.4.3 Iterative procedure for steady-state calculations . . . . .	33
3.5 Analysis of the numerical results . . . . .	34
3.5.1 Case of a stable system . . . . .	35
3.5.2 Case of a global instability . . . . .	36
3.5.3 Case of a combined instability . . . . .	38

<b>4</b>	<b>MODELING OF LOCAL INSTABILITIES VIA ROM</b>	<b>43</b>
4.1	ROM modifications to account for the effect of local instabilities . . . . .	43
4.2	Analysis of the measurements . . . . .	46
4.3	ROM simulation of the local instabilities . . . . .	47
<b>5</b>	<b>INVESTIGATION OF BWR STABILITY INDICATORS OTHER THAN THE DE- CAY RATIO</b>	<b>53</b>
5.1	Qualitative analysis of the stability properties as a function of $C_{mn}$ coeffi- cients. . . . .	53
5.2	Quantitative analysis of the stability properties as a function of $C_{mn}$ coef- ficients. . . . .	56
5.2.1	Dependence of the decay ratio on the reactivity coefficients ( $C_{mn}$ coefficients) . . . . .	56
5.2.2	Estimation of the dynamical properties of the system (amplitude, phase, frequency and decay ratio) . . . . .	56
<b>6</b>	<b>Conclusions</b>	<b>59</b>
	<b>Acknowledgements</b>	<b>61</b>
	<b>Nomenclature</b>	<b>63</b>
	<b>References</b>	<b>65</b>

# LIST OF PUBLICATIONS

This report is based on several peer-reviewed journal articles, conference proceedings, and reports that have been produced via the NORTHNET support received for the project. Such publications are listed in chronological order as follows:

- Dykin V., "The effect of different perturbations on the stability analysis of Light Water Reactors," *Licentiate Dissertation*, CTH-NT-235, Chalmers University of Technology, Sweden (2010).
- Dykin V. and Demazière C., "Development of a Reduced Order Model and its application to the Forsmark-1 instability event of 1996/1997," CTH-NT-236, Chalmers University of Technology (2010).
- Demazière C., "CORE SIM: A multi-purpose neutronic tool for research and education," *XV Mtg. Reactor Physics Calculations in the Nordic Countries*, Helsinki, Finland, April 12-13, 2011 (2011).
- Dykin V., Demazière C., Lange C. and Hennig D., "Simulation of local instabilities with the use of Reduced Order Models," *Proc. Int. Conf. on Mathematics and Computational Methods Applied to Nuclear Science and Engineering (M&C 2011)*, Rio de Janeiro, RJ, Brazil, May 8-12, 2011, Latin American Section/American Nuclear Society (2011).
- Demazière C., "CORE SIM: A multi-purpose neutronic tool for research and education," *Annals of Nuclear Energy*, **38** (12), pp. 2698-2718 (2011).
- Demazière C., "Description of the models and algorithms used in the CORE SIM neutronic tool," CTH-NT-241, Chalmers University of Technology (2011).
- Demazière C., "Validation and demonstration of the CORE SIM neutronic tool," CTH-NT-242, Chalmers University of Technology (2011).
- Demazière C., "User's manual of the CORE SIM neutronic tool," CTH-NT-243, Chalmers University of Technology (2011).
- Dykin V. and Demazière C., "Development of a fully-consistent Reduced Order Model to study instabilities in Boiling Water Reactors," *Proc. Int. Conf. on Advances in Reactor Physics - Linking Research, Industry, and Education (PHYSOR 2012)*, Knoxville, TN, USA, April 15-20, 2012, American Nuclear Society (2012).

- 
- Lange C., Hennig D., Hurtado A., Dykin V. and Demazière C., "Comments on local power oscillation phenomenon at BWRs," *Progress in Nuclear Energy*, **60**, pp. 73-88 (2012).
  - Dykin V., "Noise applications in Light Water Reactors with traveling perturbations," *PhD thesis*, CTH-NT-263, Chalmers University of Technology, Gothenburg, Sweden (2012).
  - Dykin V., Demazière C. and Vinai P., "On the possible dependence of the Decay Ratio on the void reactivity feedback," *Transactions of the American Nuclear Society*, **107**, San Diego, CA, USA, November 11-15, 2012 (2012).
  - Dykin V., Demazière C., Lange C. and Hennig D., "Investigation of global and regional instabilities with a four heated-channel Reduced Order Model," *Annals of Nuclear Energy*, **53**, pp. 381-400 (2013).
  - Dykin V., Demazière C., Lange C. and Hennig D., "Investigation of local BWR instabilities with a four-heated channel Reduced Order Model," *Annals of Nuclear Energy*, **53**, pp. 320-330 (2013).

# INTRODUCTION

A specificity of Boiling Water Reactors (BWRs) is the very strong coupling between the neutron kinetics and the thermal-hydraulics, and the resulting instabilities that can arise. BWRs can experience unstable conditions during start-up, i.e. at reduced core flow and relatively high power level, as well as during nominal operating conditions in case of an abnormal event (equipment malfunction). Calculations are thus performed via adequate coupled neutronic/thermal-hydraulic codes to verify conditions under which the reactor becomes unstable. If the margin to instabilities is not large enough, a new core loading should be designed, or an exclusion zone should be defined, i.e. a set of operating conditions that the reactor operator should always avoid should be determined. During the start-up tests of the reactor, measurements of the in-core neutron noise are usually performed. The goal of these measurements is to verify that there is a good agreement with the calculations. One parameter of interest is the Decay Ratio (DR), which characterizes the stability of BWRs.

Despite all these precautions, many instability events have occurred in the past in BWRs worldwide. The occurrence of these instability events might be attributed to two main deficiencies in the actual way to analyze and predict the stability of BWRs. The first one is simply related to the lack of proper understanding of some of the key phenomena. The second one is related to the inadequacy of the actual system codes to reproduce complicated instability patterns.

In Sweden, one of the most spectacular events was the Oskarshamn-3 in-phase instability oscillation in February 1998, where very large power oscillations (more than 40% of the nominal power from peak to peak) were undetected by the reactor operator before the plant protection system automatically shut the reactor down [1].

Another example is the Forsmark-1 channel instability event in 1996/1997. The curiosity of that event was that an analysis of the decay ratios, as calculated from the individual LPRMs (Local Power Range Monitors), showed a large spatial variation of the DR, with one half of the core appearing to be stable ( $DR \approx 0.6$ ) and the other half appearing to be unstable ( $DR > 0.9$ ) [2]. Stability calculations could not reproduce such spatially-dependent DR and furthermore could not at all predict an unstable core configuration. The corresponding operating point in the power-flow map was thus excluded and the reactor was run until its expected end of cycle. Thereafter, a visual inspection of some of the fuel assemblies revealed that there was one unseated fuel assembly. Post-calculations showed that this unseated fuel assembly could drive a Density Wave Oscillation (DWO), a purely thermo-hydraulic type of instability. There are indications that other fuel assem-

blies were unseated, but no visual inspection of those could be performed.

Further, it was demonstrated during some stability tests performed in 1990 at Ringhals-1 that relying on the decay ratio for predicting the margin to instabilities was unreliable [3]. Two neighboring operating points on the power-flow map could have very different DRs. It is thus hazardous to use the decay ratio as a means to characterize the core stability, since a slight change in the operating conditions from a stable core configuration could result in an unstable configuration. Combined modes of oscillations are also complicating the determination of the core stability, since a close-to-unstable mode can be shadowed by a stable mode having a larger amplitude.

Clearly, the modeling of instability events with system codes is a very challenging task. Although system codes represent state-of-the-art modeling techniques, the complexity of the models, algorithms, and systems considered makes it very difficult to understand the possible root-cause of given instability events. In addition, gaining physical understanding of the possible oscillations predicted by such codes is also limited. This is why complementing such codes by models/tools that are simple enough but still allow catching the main physical phenomena occurring in BWR instabilities is of prime interest. During the past years, Reduced-Order Models (ROMs) have been developed with this objective in mind, and several ROMs exist (see for instance [4–6]). The most advanced models of the earlier developed ROMs are able to represent the effect of global oscillations, as well as regional oscillations not involving any rotation of the so-called symmetry line (i.e. the line delimiting the positive from the negative lobes of the azimuthal neutronic mode).

In this project, the intention was to develop an as general as possible ROM able to represent all stability patterns encountered in BWRs. In addition to the above mentioned types of instabilities (global and regional), local oscillations might also be encountered. Furthermore, some past instabilities events also demonstrated that regional oscillations might exhibit a rotation of the symmetry line. As a consequence, the ROM developed hereafter is able to simulate global, regional (with or without rotation of the symmetry line), and local oscillations, as well as their interdependence. The developed ROM represents the only ROM capable of accounting for these three types of oscillations, and can thus be used to gain physical insight into the complex phenomena occurring in BWR instabilities. Moreover, the developed ROM can also be used to either investigate the dependence of the dynamical behavior of the system on different system parameters, or to possibly derive new stability indicators. The latter was actually the original purpose of the project, and an attempt to propose a new stability indicator was also made in this project.

It has to be emphasized that ROMs should only be used to provide a qualitative behavior of the system in case of BWR oscillations, and cannot provide a quantitative evaluation of any stability parameter.

The present report is structured as follows. First, the numerical tools and methods necessary to estimate the pure neutronic response to global, regional, and local oscillations are presented. Thereafter, a ROM capable of accounting for the effect of both global and regional oscillations, with the latter possibly exhibiting a rotating symmetry line, is described. Its extension to represent the effect of local oscillations is then touched upon. Finally, the possibility of using another stability indicator than the DR for predictive core stability evaluation is investigated.

# DEVELOPMENT OF A NUMERICAL TOOL FOR ESTIMATING NEUTRONIC RESPONSES TO GLOBAL/REGIONAL/LOCAL OSCILLATIONS

A tool, named CORE SIM, aimed at estimating the relevant neutronic responses in case of global, regional, and local oscillations was developed and is reported hereafter. The two first types of oscillation patterns require the determination of the so-called neutronic eigenfunctions of the considered nuclear core, whereas the neutron fluctuations induced a local oscillation requires the estimation of the Green's function of the system. In this chapter, the neutronic models are first described, with emphasis on the equations solved and the spatial discretization scheme adopted. Thereafter, the modelling of static core configurations is considered, followed by the modelling of dynamic core configurations. In both cases, subcritical systems with source and critical systems are respectively considered.

## 2.1 Description of the neutronic models

In this section, the equations governing the modelling of neutron transport are presented, together with the spatial discretisation scheme implemented in the tool.

### 2.1.1 Neutron transport modelling

The tool is based on diffusion theory with two energy groups and one group of delayed neutrons. In this formalism, the time- and space-dependent fast neutron flux, thermal neutron flux, and precursor density, can be expressed, respectively, as:

$$\frac{1}{v_1} \frac{\partial}{\partial t} \phi_1(\bar{r}, t) = \nabla \cdot [D_{1,0}(\bar{r}) \nabla \phi_1(\bar{r}, t)] + [(1 - \beta) v \Sigma_{f,1}(\bar{r}, t) - \Sigma_{a,1}(\bar{r}, t) - \Sigma_r(\bar{r}, t)] \phi_1(\bar{r}, t) + (1 - \beta) v \Sigma_{f,2}(\bar{r}, t) \phi_2(\bar{r}, t) + \lambda C(\bar{r}, t) + S_1(\bar{r}, t) \quad (2.1)$$

$$\frac{1}{v_2} \frac{\partial}{\partial t} \phi_2(\bar{r}, t) = \nabla \cdot [D_{2,0}(\bar{r}) \nabla \phi_2(\bar{r}, t)] + \Sigma_r(\bar{r}, t) \phi_1(\bar{r}, t) - \Sigma_{a,2}(\bar{r}, t) \phi_2(\bar{r}, t) + S_2(\bar{r}, t) \quad (2.2)$$

$$\frac{\partial C(\bar{r}, t)}{\partial t} = \beta v \Sigma_{f,1}(\bar{r}, t) \phi_1(\bar{r}, t) + \beta v \Sigma_{f,2}(\bar{r}, t) \phi_2(\bar{r}, t) - \lambda C(\bar{r}, t) \quad (2.3)$$

and where the macroscopic removal cross-section is defined as:

$$\Sigma_r(\bar{r}, t) = \Sigma_{s0,1 \rightarrow 2}(\bar{r}, t) - \frac{\Sigma_{s0,2 \rightarrow 1}(\bar{r}, t) \phi_2(\bar{r}, t)}{\phi_1(\bar{r}, t)} \quad (2.4)$$

In the previous equations, all the symbols have their usual meaning. The equations were obtained by assuming that both the prompt and delayed neutrons only contribute to the fast energy group.  $S_1(\bar{r}, t)$  and  $S_2(\bar{r}, t)$  represent possible external neutron sources in the fast and thermal groups, respectively, and as such, the tool has the ability to model both critical systems, for which  $S_1(\bar{r}, t) = 0, \forall(\bar{r}, t)$  and  $S_2(\bar{r}, t) = 0, \forall(\bar{r}, t)$ , or subcritical systems with external sources. All the macroscopic cross-sections and possible external neutron sources might be time-dependent. It was earlier demonstrated in [8] that allowing the diffusion coefficients to be time-dependent lead to dynamical results essentially identical to keeping such diffusion coefficients time-independent. Since the computational burden introduced by letting the diffusion coefficients vary with time increases drastically, the diffusion coefficients are kept time-independent in the tool reported hereafter.

In case of non-steady-state conditions, the time-dependent terms, generically expressed as  $X(\bar{r}, t)$ , can be split into a mean value  $X_0(\bar{r})$  (corresponding to the steady-state configuration of the system) and a fluctuating part  $\delta X(\bar{r}, t)$  around the mean value as:

$$X(\bar{r}, t) = X_0(\bar{r}) + \delta X(\bar{r}, t) \quad (2.5)$$

The dynamic configurations are investigated in the frequency-domain. The equations describing the dynamic behavior are obtained by removing the static equations from the dynamic ones, then performing a temporal Fourier-transform, and finally neglecting second-order terms (linear theory).

In many occurrences, the determination of the solution to an adjoint problem associated to the direct or forward static problem, frequency-dependent dynamic problem, respectively, is of high interest. In order to properly define the concept of adjoint, the space on which the previous quantities were defined needs to be given an inner product. In two-group theory, any space-dependent function can be represented as a column vector, where the first component corresponds to the fast energy group, and the second component corresponds to the thermal energy group. One can then define the inner product of two space-dependent functions  $\bar{\psi}(\bar{r}) = [\psi_1(\bar{r}) \ \psi_2(\bar{r})]^T$  and  $\bar{\varphi}(\bar{r}) = [\varphi_1(\bar{r}) \ \varphi_2(\bar{r})]^T$ , where the superscript  $T$  represents the transpose operator, as the integral of the scalar product between the two vectors  $\bar{\psi}(\bar{r})$  and  $\bar{\varphi}(\bar{r})$  on the whole volume  $V$  of the system. This reads as:

$$(\bar{\psi}, \bar{\varphi}) = \int_V \bar{\psi}^T(\bar{r}) \cdot \bar{\varphi}(\bar{r}) d\bar{r} = \int_V [\psi_1(\bar{r}) \varphi_1(\bar{r}) + \psi_2(\bar{r}) \varphi_2(\bar{r})] d\bar{r} \quad (2.6)$$

Operators to any function defined on the previous space can be formally considered as 2x2 matrices, and the application of such operators on any space-dependent function

(considered as a vector), can be regarded as the multiplication of a matrix and a vector. The adjoint  $\bar{\bar{L}}^+$  of any operator  $\bar{\bar{L}}$  can then be defined as the one which satisfies the relationship:

$$\left(\bar{\psi}^+, \bar{\bar{L}} \times \bar{\varphi}\right) = \left(\bar{\bar{L}}^+ \times \bar{\psi}^+, \bar{\varphi}\right) \quad (2.7)$$

where  $\bar{\psi}^+$  and  $\bar{\varphi}$ , which are the adjoint and forward or direct functions respectively, satisfy certain boundary and continuity conditions. In two-group diffusion theory, it could be further demonstrated that the adjoint operator is the transposed of the direct operator [9], that is:

$$\bar{\bar{L}}^+ = \bar{\bar{L}}^T \quad (2.8)$$

### 2.1.2 Algorithm used for the spatial discretisation

In the developed tool, any three-dimensional system is assumed to be made of adjacent volumes or nodes. In a cartesian coordinate system, a given node  $n$  can be represented by the triplet of indexes  $(I, J, K)$ , where the indexes  $I$ ,  $J$ , and  $K$  refer to the  $x$ -,  $y$ -, and  $z$ -directions, respectively. With the notations and conventions used throughout this section and defined in Figs. 2.1 and 2.2, the equations presented in Section 2.1.1 are spatially-averaged on each of these nodes.

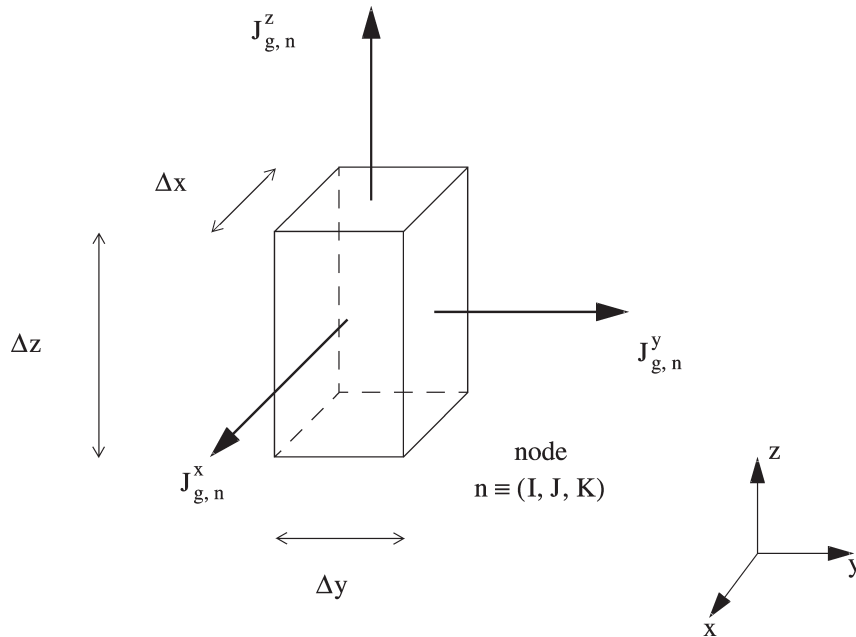


**Figure 2.1:** Principles and conventions used for the spatial discretisation of a node  $n$ .

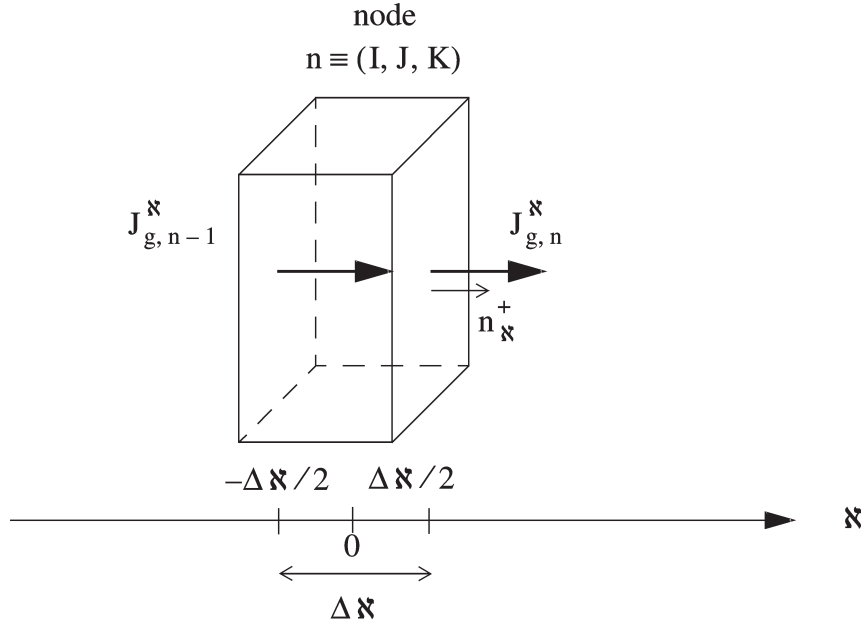


**Figure 2.2:** Generic notations relative to a node  $n$  used in the spatial discretisation along a direction  $\aleph$ .

One then introduces the following node-averaged quantities:

$$\phi_{g,n}(t) = \frac{1}{V_n} \int_{V_n} \phi_g(\bar{r}, t) d\bar{r} \quad (2.9)$$

$$\Sigma_{g,n}(t) = \frac{\frac{1}{V_n} \int_{V_n} \Sigma_g(\bar{r}, t) \phi_g(\bar{r}, t) d\bar{r}}{\phi_{g,n}(t)} \quad (2.10)$$

$$S_{g,n}(t) = \frac{1}{V_n} \int_{V_n} S_g(\bar{r}, t) d\bar{r} \quad (2.11)$$

with  $\Sigma_g$  having the generic meaning of a macroscopic cross-section, and with  $V_n$  representing the volume of the node  $n$ . This way of defining the node-averaged data, which preserves the actual reaction rates per node, is consistent with the group constants provided by any static core calculator. Using a spatial discretisation scheme based on finite differences and assuming that the scalar neutron flux in the middle of the nodes is equal to the node-averaged scalar neutron flux (box-scheme), the node-averaged streaming terms can be approximated as [10]:

$$\begin{aligned} \frac{1}{V_n} \int_V \bar{\nabla} \cdot [D_{g,0}(\bar{r}, t) \bar{\nabla} \phi_g(\bar{r}, t)] d\bar{r} &= - \sum_{\aleph=x,y,z} \frac{J_{g,n}^{\aleph}(t) - J_{g,n-1}^{\aleph}(t)}{\Delta \aleph} \\ &= - \sum_{\aleph=x,y,z} \left[ a_{g,n}^{\aleph}(t) \phi_{g,n}(t) + b_{g,n}^{\aleph}(t) \phi_{g,n+1}(t) + c_{g,n}^{\aleph}(t) \phi_{g,n-1}(t) \right] \end{aligned} \quad (2.12)$$

In this equation,  $\aleph$  represents the direction  $x$ ,  $y$ , or  $z$ ,  $\Delta \aleph$  is the node width in the  $\aleph$ -direction. In the following, the subscripts “+1” and “-1” represent the nodes adjacent to

the node  $n$  along the  $\aleph$ -direction for increasing, decreasing, respectively,  $\aleph$  values (see Fig. 2.2). In this equation, the surface-averaged net neutron current relative to the node  $n$  in the  $\aleph$ -direction, with  $\bar{n}_{\aleph}^+$  being the outward normal relative to node  $n$  (as represented in Fig. 2.2), is defined as:

$$J_{g,n}^{\aleph} = \frac{1}{\Delta\aleph \cdot \Delta\wp} \int_{-\Delta\aleph/2}^{\Delta\aleph/2} \int_{-\Delta\wp/2}^{\Delta\wp/2} \bar{J}_g(\bar{r}_{\aleph}) \cdot \bar{n}_{\aleph}^+ d\aleph d\wp \quad (2.13)$$

with  $r_{\aleph}$  representing the position of any point belonging to the surface normal to  $n_{\aleph}^+$  and defined as:

$$\begin{cases} \aleph = \Delta\aleph/2 \\ \wp \in [-\Delta\wp/2, \Delta\wp/2] \\ \wp \in [-\Delta\wp/2, \Delta\wp/2] \end{cases}$$

The expressions of the coupling coefficients  $a_{g,n}^{\aleph}(t)$ ,  $b_{g,n}^{\aleph}(t)$ , and  $c_{g,n}^{\aleph}(t)$  are given in Table 2.1. At the boundary of the system, Marshak boundary conditions are used, which in the case of multigroup diffusion theory, read as:

$$\bar{J}_g(\bar{r}_{\aleph}) \cdot \bar{n}_{\aleph} = \frac{1}{2} \varphi_g^b \quad (2.14)$$

where  $\bar{r}_{\aleph}$  represents a spatial point on the boundary with  $\bar{n}_{\aleph}$  being the outward normal to the boundary and  $\varphi_g^b$  represents the scalar neutron flux at the boundary. The derivation of the coupling coefficients is detailed in [11].

**Table 2.1:** Coupling coefficients in the  $\aleph$ -direction used for the spatial discretisation.

	$a_{g,n}^{\aleph}(t)$	$b_{g,n}^{\aleph}(t)$	$c_{g,n}^{\aleph}(t)$
If the node $n-1$ does not exist	$\frac{2D_{g,0,n}D_{g,0,n+1}}{(\Delta\aleph)^2(D_{g,0,n}+D_{g,0,n+1})} + \frac{1/2}{\Delta\aleph + \frac{(\Delta\aleph)^2}{4D_{g,0,n}}}$	$-\frac{2D_{g,0,n}D_{g,0,n+1}}{(\Delta\aleph)^2(D_{g,0,n}+D_{g,0,n+1})}$	0
If the nodes $n-1$ and $n+1$ both exist	$\frac{2D_{g,0,n-1}D_{g,0,n}}{(\Delta\aleph)^2(D_{g,0,n-1}+D_{g,0,n})} + \frac{2D_{g,0,n}D_{g,0,n+1}}{(\Delta\aleph)^2(D_{g,0,n}+D_{g,0,n+1})}$	$-\frac{2D_{g,0,n}D_{g,0,n+1}}{(\Delta\aleph)^2(D_{g,0,n}+D_{g,0,n+1})}$	$-\frac{2D_{g,0,n-1}D_{g,0,n}}{(\Delta\aleph)^2(D_{g,0,n-1}+D_{g,0,n})}$
If the node $n+1$ does not exist	$\frac{2D_{g,0,n-1}D_{g,0,n}}{(\Delta\aleph)^2(D_{g,0,n-1}+D_{g,0,n})} + \frac{1/2}{\Delta\aleph + \frac{(\Delta\aleph)^2}{4D_{g,0,n}}}$	0	$-\frac{2D_{g,0,n-1}D_{g,0,n}}{(\Delta\aleph)^2(D_{g,0,n-1}+D_{g,0,n})}$

After spatial discretisation, the time- and space-dependent fast neutron flux, thermal neutron flux, and precursor density, can be expressed, respectively, as:

$$\begin{aligned} \frac{1}{v_1} \frac{\partial}{\partial t} \phi_{1,n}(t) = & - \sum_{\aleph=x,y,z} \left[ a_{1,n}^{\aleph}(t) \phi_{1,n}(t) + b_{1,n}^{\aleph}(t) \phi_{1,n+1}(t) + c_{1,n}^{\aleph}(t) \phi_{1,n-1}(t) \right] \\ & + [(1-\beta)v\Sigma_{f,1,n}(t) - \Sigma_{a,1,n}(t) - \Sigma_{r,n}(t)] \phi_{1,n}(t) + (1-\beta)v\Sigma_{f,2,n}(t) \phi_{2,n}(t) \\ & + \lambda C_n(t) + S_{1,n}(t) \end{aligned} \quad (2.15)$$

$$\frac{1}{v_2} \frac{\partial}{\partial t} \phi_{2,n}(t) = - \sum_{\aleph=x,y,z} \left[ a_{2,n}^{\aleph}(t) \phi_{2,n}(t) + b_{2,n}^{\aleph}(t) \phi_{2,n+1}(t) + c_{2,n}^{\aleph}(t) \phi_{2,n-1}(t) \right] \quad (2.16)$$

$$+ \Sigma_{r,n}(t) \phi_{1,n}(t) - \Sigma_{a,2,n}(t) \phi_{2,n}(t) + S_{2,n}(t)$$

$$\frac{\partial C_n(t)}{\partial t} = \beta v \Sigma_{f,1,n}(t) \phi_{1,n}(t) + \beta v \Sigma_{f,2,n}(t) \phi_{2,n}(t) - \lambda C_n(t) \quad (2.17)$$

## 2.2 Modelling of static core configurations

### 2.2.1 Subcritical systems with source

If the system contains an external neutron source (case of a subcritical system driven by an external neutron source), Eqs. (2.1) - (2.3) written in steady-state conditions reduce to the following matrix equation:

$$\left[ \nabla \cdot \overline{\overline{D}}(\bar{r}) \nabla + \overline{\overline{\Sigma}}_{sta}(\bar{r}) - \overline{\overline{F}}(\bar{r}) \right] \times \begin{bmatrix} \phi_{1,0}(\bar{r}) \\ \phi_{2,0}(\bar{r}) \end{bmatrix} = - \begin{bmatrix} S_{1,0}(\bar{r}) \\ S_{2,0}(\bar{r}) \end{bmatrix} \quad (2.18)$$

with

$$\overline{\overline{D}}(\bar{r}) = \begin{bmatrix} D_{1,0}(\bar{r}) & 0 \\ 0 & D_{2,0}(\bar{r}) \end{bmatrix} \quad (2.19)$$

$$\overline{\overline{\Sigma}}_{sta}(\bar{r}) = \begin{bmatrix} -\Sigma_{a,1,0}(\bar{r}) - \Sigma_{r,0}(\bar{r}) & 0 \\ \Sigma_{r,0}(\bar{r}) & -\Sigma_{a,2,0}(\bar{r}) \end{bmatrix} \quad (2.20)$$

$$\overline{\overline{F}}(\bar{r}) = \begin{bmatrix} -\nu \Sigma_{f,1,0}(\bar{r}) & -\nu \Sigma_{f,2,0}(\bar{r}) \\ 0 & 0 \end{bmatrix} \quad (2.21)$$

and where the subscript 0 refers to the static values of the different variables.

An adjoint problem associated with the forward problem as given by Eq. (2.18) can then be formally written as:

$$\left[ \nabla \cdot \overline{\overline{D}}(\bar{r}) \nabla + \overline{\overline{\Sigma}}_{sta}^T(\bar{r}) - \overline{\overline{F}}^T(\bar{r}) \right] \times \begin{bmatrix} \phi_{1,0}^\dagger(\bar{r}) \\ \phi_{2,0}^\dagger(\bar{r}) \end{bmatrix} = - \begin{bmatrix} S_{1,0}^\dagger(\bar{r}) \\ S_{2,0}^\dagger(\bar{r}) \end{bmatrix} \quad (2.22)$$

From a mathematical viewpoint, the static forward problem of a subcritical source-driven system as given by Eq. (2.18) is represented by a non-homogeneous equation. Likewise, the corresponding adjoint problem as given by Eq. (2.19) is also represented by a non-homogeneous equation.

After spatial discretisation, both equations reduce to:

$$\overline{\overline{M}}_{sta}^{sub} \times \overline{\overline{\phi}}_0 = \overline{\overline{S}}_0 \text{ and } \overline{\overline{M}}_{sta}^{sub\dagger} \times \overline{\overline{\phi}}_0^\dagger = \overline{\overline{S}}_0^\dagger \quad (2.23)$$

Due to the very large number of nodes used in reactor calculations, the direct determination of the inverse of  $\overline{\overline{M}}_{sta}^{sub}$  and  $\overline{\overline{M}}_{sta}^{sub\dagger}$  is usually impossible. Instead, the matrices  $\overline{\overline{M}}_{sta}^{sub}$  and  $\overline{\overline{M}}_{sta}^{sub\dagger}$ , which are sparse, are first factorized into unit lower triangular matrices  $\overline{\overline{L}}$  and  $\overline{\overline{L}}^\dagger$ , and upper triangular matrices  $\overline{\overline{U}}$  and  $\overline{\overline{U}}^\dagger$ , such that:

$$\overline{\overline{L}} \times \overline{\overline{U}} = \overline{\overline{P}} \times \overline{\overline{M}}_{sta}^{sub} \times \overline{\overline{Q}} \text{ and } \overline{\overline{L}}^\dagger \times \overline{\overline{U}}^\dagger = \overline{\overline{P}}^\dagger \times \overline{\overline{M}}_{sta}^{sub\dagger} \times \overline{\overline{Q}}^\dagger \quad (2.24)$$

where  $\overline{P}$  and  $\overline{P}^\dagger$  are row permutation matrices, and  $\overline{Q}$  and  $\overline{Q}^\dagger$  are column reordering matrices. The matrix factorization as given by Eq. (2.23) is directly performed in *MatLab* via the built-in UMFPACK package [12]. The factorization is carried out while preserving as much as possible the sparsity of the matrices. Once the factorization of the matrices has been performed, the solution to the problem can be readily obtained by forward and backward substitutions as:

$$\bar{\phi}_0 = \overline{Q} \times \left\{ \overline{U} \setminus \left[ \overline{L} \setminus \left( \overline{P} \times \overline{S}_0 \right) \right] \right\} \quad \text{and} \quad \bar{\phi}_0^\dagger = \overline{Q}^\dagger \times \left\{ \overline{U}^\dagger \setminus \left[ \overline{L}^\dagger \setminus \left( \overline{P}^\dagger \times \overline{S}_0^\dagger \right) \right] \right\} \quad (2.25)$$

Further details about the procedure used in the tool to solve non-homogeneous equations can be found in [11].

In order to benchmark the numerical algorithms used for estimating the solution to non-homogeneous equations, a one-dimensional one-region subcritical system was considered. The size of the system was set to  $2a = 300$  cm, and the homogeneous macroscopic cross-sections and diffusion coefficients were chosen to be representative of a typical LWR. The subcriticality was then obtained by decreasing the macroscopic fission cross-section in the thermal group. The material data thus used in the benchmark are given in Table 2.2. An external fast neutron source was introduced as a point-like source located at  $z' = -50$  cm. The numerical solution was estimated with a node size of  $\Delta z = 1$  cm.

**Table 2.2:** Values of the material data used in the static benchmark in case of a one-dimensional one-region subcritical system.

$D_{1,0}$ [cm]	$D_{2,0}$ [cm]	$\Sigma_{a,1,0}$ [cm <sup>-1</sup> ]	$\Sigma_{a,2,0}$ [cm <sup>-1</sup> ]	$\Sigma_r$ [cm <sup>-1</sup> ]	$\nu\Sigma_{f,1,0}$ [cm <sup>-1</sup> ]	$\nu\Sigma_{f,2,0}$ [cm <sup>-1</sup> ]
1.4376	0.3723	0.0115	0.1019	0.0151	0.0057	0.1283

The reference solution to the forward problem [i.e. Eq. (2.18)], defined on  $z \in [-a_{ext}; a_{ext}]$ , was derived from [13,14] and is given by:

$$\begin{bmatrix} \phi_{1,0}(z) \\ \phi_{2,0}(z) \end{bmatrix} = \begin{bmatrix} 1 \\ c_\mu \end{bmatrix} G_\mu(z, z') + \begin{bmatrix} 1 \\ c_\nu \end{bmatrix} G_\nu(z, z') \quad (2.26)$$

with

$$G_\mu(z, z') = \begin{cases} E_- \times \sin\{\mu \times [z + a_{ext}]\}, & \text{for } z < z' \\ E_+ \times \sin\{\mu \times [z - a_{ext}]\}, & \text{for } z > z' \end{cases} \quad (2.27)$$

$$G_\nu(z, z') = \begin{cases} F_0 \times \sinh\{\nu \times [z + a_{ext}]\}, & \text{for } z < z' \\ F_+ \times \sinh\{\nu \times [z - a_{ext}]\}, & \text{for } z > z' \end{cases} \quad (2.28)$$

with the extrapolated distance  $a_{ext}$  defined as:

$$a_{ext} = a + 2D_{1,0} \quad (2.29)$$

The coupling coefficients  $c_\mu$  and  $c_\nu$  are expressed as:

$$c_\mu = \frac{\Sigma_{r,0}}{\Sigma_{a,2,0} + D_{2,0}\mu^2} \quad \text{and} \quad c_\nu = \frac{\Sigma_{r,0}}{\Sigma_{a,2,0} - D_{2,0}\nu^2} \quad (2.30)$$

with

$$\mu^2 = \frac{1}{2} \left[ - \left( \frac{1}{l_1^2} + \frac{1}{l_2^2} \right) + \sqrt{\left( \frac{1}{l_1^2} + \frac{1}{l_2^2} \right)^2 + \frac{4[\alpha - 1]}{l_1^2 \cdot l_2^2}} \right] \quad (2.31)$$

$$\nu^2 = \frac{1}{2} \left[ \left( \frac{1}{l_1^2} + \frac{1}{l_2^2} \right) + \sqrt{\left( \frac{1}{l_1^2} + \frac{1}{l_2^2} \right)^2 + \frac{4[\alpha - 1]}{l_1^2 \cdot l_2^2}} \right] \quad (2.32)$$

and

$$l_1^2 = \frac{D_{1,0}}{\Sigma_{a,1,0} + \Sigma_{r,0} - \nu \Sigma_{f,1,0}} \quad (2.33)$$

$$l_2^2 = \frac{D_{2,0}}{\Sigma_{a,2,0}} \quad (2.34)$$

$$\alpha = \frac{\Sigma_{r,0} \times \nu \Sigma_{f,2,0}}{(\Sigma_{a,1,0} + \Sigma_{r,0} - \nu \Sigma_{f,1,0}) \times \Sigma_{a,2,0}} \quad (2.35)$$

The coefficients  $E_-$ ,  $E_+$ ,  $F_-$ , and  $F_+$  are solutions of the following equation:

$$\begin{bmatrix} \sin \mu [z' - a_{ext}] & -\sin \mu [z' + a_{ext}] & \sinh \nu [z' - a_{ext}] & -\sinh \nu [z' + a_{ext}] \\ c_\mu \sin \mu [z' - a_{ext}] & -c_\mu \sin \mu [z' + a_{ext}] & c_\nu \sinh \nu [z' - a_{ext}] & -c_\nu \sinh \nu [z' + a_{ext}] \\ \mu \cos \mu [z' - a_{ext}] & -\mu \cos \mu [z' + a_{ext}] & \nu \cosh \nu [z' - a_{ext}] & -\nu \cosh \nu [z' + a_{ext}] \\ c_\mu \mu \cos \mu [z' - a_{ext}] & -c_\mu \mu \cos \mu [z' + a_{ext}] & c_\nu \nu \cosh \nu [z' - a_{ext}] & -c_\nu \nu \cosh \nu [z' + a_{ext}] \end{bmatrix} \times \begin{bmatrix} E_+ \\ E_- \\ F_+ \\ F_- \end{bmatrix} = \begin{bmatrix} 0 \\ 0 \\ -1/D_{1,0} \\ 0 \end{bmatrix} \quad (2.36)$$

The analytical and numerical solutions are given in Fig. 2.3. Although the results are presented in arbitrary units, the analytical and numerical solutions were not scaled between each other. A very good agreement can be noticed in terms of the computed space-dependence of the fast and thermal static neutron fluxes, as well as of the computed eigenvalue (for which the solution procedure is explained in Section 2.2.2). The exponential decrease of the static neutron away from the neutron source is typical of subcritical systems.

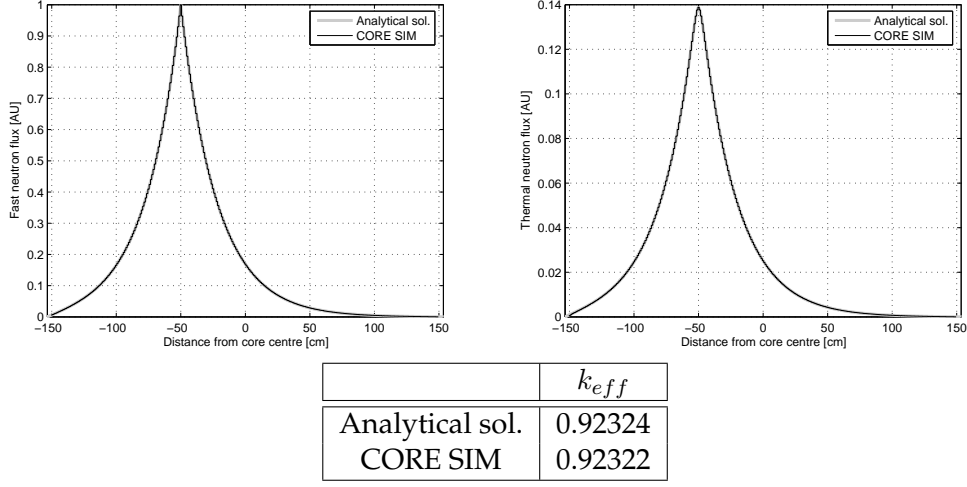


**Figure 2.3:** Results of the static benchmark in case of a one-dimensional one-region subcritical system (forward problem).

### 2.2.2 Critical systems

If the system does not contain any external neutron source, a steady-state solution to Eqs. (2.1) - (2.3) only exists if the system is critical. Eqs. (2.1) - (2.3) written in steady-state conditions then reduce to the following matrix equation:

$$\left[ \nabla \cdot \overline{\overline{D}}(\bar{r}) \nabla + \overline{\overline{\Sigma}}_{sta}(\bar{r}) \right] \times \begin{bmatrix} \phi_{1,0}(\bar{r}) \\ \phi_{2,0}(\bar{r}) \end{bmatrix} = \overline{\overline{F}}(\bar{r}) \times \begin{bmatrix} \phi_{1,0}(\bar{r}) \\ \phi_{2,0}(\bar{r}) \end{bmatrix} \quad (2.37)$$

If the system is not critical, a steady-state solution can still be obtained by re-normalizing the fission source terms by a factor  $k_m$ , and thus Eqs. (2.1) - (2.3) reduce to:

$$\left[ \nabla \cdot \overline{\overline{D}}(\bar{r}) \nabla + \overline{\overline{\Sigma}}_{sta}(\bar{r}) \right] \times \begin{bmatrix} \phi_{1,m}(\bar{r}) \\ \phi_{2,m}(\bar{r}) \end{bmatrix} = \frac{1}{k_m} \overline{\overline{F}}(\bar{r}) \times \begin{bmatrix} \phi_{1,m}(\bar{r}) \\ \phi_{2,m}(\bar{r}) \end{bmatrix} \quad (2.38)$$

Both the eigenfunctions  $\phi_{1,m}(r)$  and  $\phi_{2,m}(r)$  and the corresponding eigenvalue  $1/k_m$  have to be determined. There is an infinite number of solutions, i.e. an infinite number of pairs of solutions  $[\phi_{1,m}(\bar{r}) \ \phi_{2,m}(\bar{r})]$  and  $k_m$ , where the index  $m$  represents the mode number. The eigenfunctions having the same sign throughout the entire system corresponds to the static fluxes denoted as  $[\phi_{1,0}(\bar{r}) \ \phi_{2,0}(\bar{r})]$  (fundamental mode) and the associated factor  $k_0$  is then the effective multiplication factor of the system, i.e.

$$k_0 = k_{eff} \quad (2.39)$$

All other eigenfunctions change sign throughout the system, and their associated factor  $k_m$  is strictly smaller than  $k_{eff}$ . It is customary to order the eigenmodes in increasing order of their eigenvalue  $1/k_m$  (thus in decreasing order of the factor  $k_m$ ):

$$k_{eff} = k_0 > k_1 > k_2 > \dots > k_m \quad (2.40)$$

It has to be noted that Eq. (2.37) is a sub-case of Eq. (2.38) obtained with  $k_0 = k_{eff} = 1$ .

As before, an adjoint problem associated with the forward problem as given by Eq. (2.38) can be formally written as:

$$\left[ \nabla \cdot \overline{\overline{D}}(\vec{r}) \nabla + \overline{\overline{\Sigma}}_{sta}^T(\vec{r}) \right] \times \begin{bmatrix} \phi_{1,m}^\dagger(\vec{r}) \\ \phi_{2,m}^\dagger(\vec{r}) \end{bmatrix} = \frac{1}{k_m^\dagger} \overline{\overline{F}}^T(\vec{r}) \times \begin{bmatrix} \phi_{1,m}^\dagger(\vec{r}) \\ \phi_{2,m}^\dagger(\vec{r}) \end{bmatrix} \quad (2.41)$$

It could be demonstrated that in two-group diffusion theory [9]:

$$k_m^\dagger = k_m \quad (2.42)$$

From a mathematical viewpoint, the static forward problem of a critical system as given by Eq. (2.38) is represented by an eigenvalue equation. Likewise, the corresponding adjoint problem as given by Eq. (2.41) is also represented by an eigenvalue equation.

After spatial discretisation, both equations reduce to:

$$\overline{\overline{M}}_{sta}^{crit} \times \overline{\phi}_m = \frac{1}{k_m} \overline{\overline{F}} \times \overline{\phi}_m \text{ and } \overline{\overline{M}}_{sta}^{crit\dagger} \times \overline{\phi}_m^\dagger = \frac{1}{k_m^\dagger} \overline{\overline{F}}^T \times \overline{\phi}_m^\dagger \quad (2.43)$$

Iterative techniques are required to solve the above problems, which can be generically rewritten as:

$$\overline{\overline{A}} \times \overline{x}_m = \lambda_m \overline{x}_m \quad (2.44)$$

with

$$\overline{\overline{A}} = \overline{\overline{M}}_{sta}^{crit}{}^{-1} \times \overline{\overline{F}} \text{ or } \overline{\overline{A}} = \overline{\overline{M}}_{sta}^{crit\dagger}{}^{-1} \times \overline{\overline{F}}^T \quad (2.45)$$

$$\lambda_m = k_m \text{ or } \lambda_m = k_m^\dagger \quad (2.46)$$

and

$$\overline{x}_m = \overline{\phi}_m \text{ or } \overline{x}_m = \overline{\phi}_m^\dagger \quad (2.47)$$

As earlier explained in Section 2.2.1, the calculation of the inverse of  $\overline{\overline{M}}_{sta}^{crit}$  or  $\overline{\overline{M}}_{sta}^{crit\dagger}$  is avoided by first performing a LU factorization with full pivoting as:

$$\overline{\overline{L}} \times \overline{\overline{U}} = \overline{\overline{P}} \times \overline{\overline{M}}_{sta}^{crit} \times \overline{\overline{Q}} \text{ or } \overline{\overline{L}}^\dagger \times \overline{\overline{U}}^\dagger = \overline{\overline{P}}^\dagger \times \overline{\overline{M}}_{sta}^{crit\dagger} \times \overline{\overline{Q}}^\dagger \quad (2.48)$$

leading for Eq. (2.44) to:

$$\overline{\overline{Q}} \times \left\{ \overline{\overline{U}} \setminus \left[ \overline{\overline{L}} \setminus \left( \overline{\overline{P}} \times \overline{\overline{F}} \times \overline{x}_m \right) \right] \right\} = \lambda_m \overline{x}_m \text{ or } \overline{\overline{Q}}^\dagger \times \left\{ \overline{\overline{U}}^\dagger \setminus \left[ \overline{\overline{L}}^\dagger \setminus \left( \overline{\overline{P}}^\dagger \times \overline{\overline{F}}^\dagger \times \overline{x}_m \right) \right] \right\} = \lambda_m \overline{x}_m \quad (2.49)$$

In the developed computational tool, two techniques have been implemented in order to be able to determine any eigenmode  $m$  (not only the fundamental mode). Namely, the explicitly-restarted Arnoldi method and the power iteration method with Wielandt's shift have been used.

#### *Explicitly-restarted Arnoldi method*

Some of the most efficient techniques to solve eigenvalue problems are based on Krylov subspace methods. The explicitly-restarted Arnoldi method belongs to this class of techniques [15]. The Arnoldi method is based on the fact that useful information is

lost during the application of the classical power iteration method. Namely, only the latest estimates of the eigenvector and eigenvalue are used for subsequently calculating a new estimate of the eigenvector and eigenvalue. In the Arnoldi method instead, a Krylov subspace containing an estimate of the eigenvectors of the matrix  $\overline{\overline{A}}$  obtained during the application of the power iteration method during  $t$  iterations is first constructed, i.e. the following space is constructed:

$$\mathfrak{R}_t(\overline{\overline{A}}, \overline{\overline{v}}) = \text{span} \left\{ \overline{\overline{v}}, \overline{\overline{A}} \times \overline{\overline{v}}, \overline{\overline{A}}^2 \times \overline{\overline{v}}, \dots, \overline{\overline{A}}^{t-1} \times \overline{\overline{v}} \right\} \quad (2.50)$$

with

$$t \ll \text{dimension of } \overline{\overline{A}} \quad (2.51)$$

Thereafter, an orthonormal basis of this subspace is estimated. Finally, the eigenvectors/eigenvalues of this orthonormal basis are determined. The eigenvectors of the matrix representing the projection of the original matrix on the Krylov subspace can be used for determining the eigenvectors of the original matrix, and therefore the eigenvectors of  $\overline{\overline{A}}$  can be estimated from the eigenvectors of the matrix representing the projection of the original matrix on the Krylov subspace. The main advantage of this procedure is the fact that the projection matrix is an Hessenberg matrix of size  $t \times t$ , i.e. much smaller than the size of the original matrix. Consequently, the determination of the  $t$  eigenvectors and corresponding eigenvalues is relatively easy.

The iterative scheme of the explicitly-restarted Arnoldi method can be sketched as follows [16,17]:

- First, an orthogonal basis of  $\mathfrak{R}_t(\overline{\overline{A}}, \overline{\overline{v}})$  using the Gram-Schmidt orthogonalization process is constructed. This results in the construction of the matrix  $\overline{\overline{V}}_t = (v_{:,1}, v_{:,2}, \dots, v_{:,t})$  representing an orthogonal basis of  $\mathfrak{R}_t(\overline{\overline{A}}, \overline{\overline{v}})$ , as well as a reduced Hessenberg matrix  $\overline{\overline{H}}_r$ , such that one has:

$$\overline{\overline{V}}_t^T \times \overline{\overline{A}} \times \overline{\overline{V}}_t = \overline{\overline{H}}_r \quad (2.52)$$

- Thereafter, the pairs of eigenvectors  $x_{:,j}$  and eigenvalues  $\Lambda_j$  of the reduced Hessenberg matrix  $\overline{\overline{H}}_r$  (for  $1 \leq j \leq t$ ) are determined, resulting in:

$$\overline{\overline{H}}_r \times \overline{\overline{X}} = \overline{\overline{X}} \times \overline{\overline{\Lambda}} \quad (2.53)$$

with

$$\overline{\overline{X}} = (x_{:,1}, x_{:,2}, \dots, x_{:,t}) \quad (2.54)$$

and

$$\overline{\overline{\Lambda}} = \begin{bmatrix} \Lambda_1 & 0 & \dots & \dots & 0 \\ 0 & \Lambda_2 & 0 & \dots & \dots \\ \dots & 0 & \dots & 0 & \dots \\ \dots & \dots & 0 & \Lambda_{t-1} & 0 \\ 0 & \dots & \dots & 0 & \Lambda_t \end{bmatrix} \quad (2.55)$$

Since the reduced Hessenberg matrix is chosen to be of small size, the determination of its eigenvectors and eigenvalues is relatively easy. Such a determination is directly carried out in *MatLab* via the built-in LAPACK package [18].

- One could then demonstrate that the eigenvectors of  $\overline{\overline{A}}$  are given by the columns of  $\overline{\overline{V}}_t \times \overline{\overline{X}}$  and the corresponding eigenvalues are  $\overline{\overline{\Lambda}}$ .
- Since the eigenvalues of the reduced Hessenberg matrix  $\overline{\overline{H}}_r$  might be bad approximations of the eigenvalues of the original matrix  $\overline{\overline{A}}$ , especially if the subspace dimension  $t$  is kept small, the algorithm is (explicitly) restarted with a linear combination of the eigenvectors of  $\overline{\overline{A}}$  until some convergence criteria on the eigenvectors are fulfilled.

Further details about the Arnoldi method implemented in the numerical tool can be found in [11]. The explicitly-restarted Arnoldi method is an extremely efficient method for calculating the eigenfunctions/eigenvalues in a minimum computational time, since several eigenmodes can be estimated simultaneously. Nevertheless, it cannot be proved that the eigenvalues of  $\overline{\overline{H}}_r$  will converge to the extreme eigenvalues of  $\overline{\overline{A}}$  when  $\overline{\overline{A}}$  is non-symmetric (even if such a convergence is usually observed) [19]. In order to circumvent possible convergence problem, a power iteration method using Wielandt's shift technique was also implemented in the numerical tool, and is explained in the following.

*Power iteration method with Wielandt's shift technique*

The basic idea in Wielandt's shift technique is to modify the original problem as given by Eq. (2.43) into the following one [10]:

$$\begin{aligned} \left( \overline{\overline{M}} - \frac{1}{k_{est}} \overline{\overline{F}} \right) \times \overline{\overline{\phi}}_m &= \left( \frac{1}{k_m} - \frac{1}{k_{est}} \right) \overline{\overline{F}} \times \overline{\overline{\phi}}_m \\ \text{and } \left( \overline{\overline{M}}^\dagger - \frac{1}{k_{est}} \overline{\overline{F}}^T \right) \times \overline{\overline{\phi}}_m^\dagger &= \left( \frac{1}{k_m^\dagger} - \frac{1}{k_{est}} \right) \overline{\overline{F}}^T \times \overline{\overline{\phi}}_m^\dagger \end{aligned} \quad (2.56)$$

where  $k_{est}$  is a known (input) parameter. The above problems can be generically rewritten as:

$$\overline{\overline{A}}_W \times \overline{\overline{x}}_m = \alpha_m \overline{\overline{x}}_m \quad (2.57)$$

with

$$\overline{\overline{A}}_W = \left( \overline{\overline{M}} - \frac{1}{k_{est}} \overline{\overline{F}} \right)^{-1} \times \overline{\overline{F}} \text{ or } \overline{\overline{A}}_W = \left( \overline{\overline{M}}^\dagger - \frac{1}{k_{est}} \overline{\overline{F}}^T \right) \times \overline{\overline{F}}^T \quad (2.58)$$

$$\frac{1}{\alpha_m} = \frac{1}{k_m} - \frac{1}{k_{est}} \text{ or } \frac{1}{\alpha_m} = \frac{1}{k_m^\dagger} - \frac{1}{k_{est}} \quad (2.59)$$

and

$$\overline{\overline{x}}_m = \overline{\overline{\phi}}_m \text{ or } \overline{\overline{x}}_m = \overline{\overline{\phi}}_m^\dagger \quad (2.60)$$

As earlier explained in Section 2.2.1, the calculation of the inverse of  $\overline{\overline{M}} - \frac{1}{k_{est}} \overline{\overline{F}}$  or  $\overline{\overline{M}}^\dagger - \frac{1}{k_{est}} \overline{\overline{F}}^T$  is avoided by first performing a LU factorization with full pivoting as:

$$\overline{\overline{L}} \times \overline{\overline{U}} = \overline{\overline{P}} \times \left( \overline{\overline{M}} - \frac{1}{k_{est}} \overline{\overline{F}} \right) \times \overline{\overline{Q}} \text{ or } \overline{\overline{L}}^\dagger \times \overline{\overline{U}}^\dagger = \overline{\overline{P}}^\dagger \times \left( \overline{\overline{M}}^\dagger - \frac{1}{k_{est}} \overline{\overline{F}}^T \right) \times \overline{\overline{Q}}^\dagger \quad (2.61)$$

leading for Eq. (2.57) to:

$$\overline{\overline{Q}} \times \left\{ \overline{\overline{U}} \setminus \left[ \overline{\overline{L}} \setminus \left( \overline{\overline{P}} \times \overline{\overline{F}} \times \overline{\overline{x}}_m \right) \right] \right\} = \alpha_m \overline{\overline{x}}_m \text{ or } \overline{\overline{Q}}^\dagger \times \left\{ \overline{\overline{U}}^\dagger \setminus \left[ \overline{\overline{L}}^\dagger \setminus \left( \overline{\overline{P}}^\dagger \times \overline{\overline{F}}^\dagger \times \overline{\overline{x}}_m \right) \right] \right\} = \alpha_m \overline{\overline{x}}_m \quad (2.62)$$

The power iteration method applied to the modified equation (2.57) leads to the following iterative scheme:

$$\bar{x}_m^{(p)} = \frac{1}{\alpha_m^{(p-1)}} \bar{A}_W \times \bar{x}_m^{(p-1)} \quad (2.63)$$

and

$$\alpha_m^{(p)} = \frac{\bar{x}_m^{(p-1),T} \times [\bar{A}_W \times \bar{x}_m^{(p-1)}]}{\bar{x}_m^{(p-1),T} \times \bar{x}_m^{(p-1)}} = \alpha_m^{(p-1)} \frac{\bar{x}_m^{(p-1),T} \times \bar{x}_m^{(p)}}{\bar{x}_m^{(p-1),T} \times \bar{x}_m^{(p-1)}} \quad (2.64)$$

The iterative scheme given by Eqs. (2.63) and (2.64) completely defines the power iteration method using Wielandt's shift technique. It could be demonstrated that this iterative scheme converges to the eigenvector of the matrix  $\bar{A}$  having the eigenvalue closest to  $k_{est}$  [see for instance [11]]. The convergence of this method is directly related to how close to one of the existing eigenvalues  $k_{est}$  actually is. In the developed computational tool, a first guess of the different eigenvalues is obtained by applying the Arnoldi method outlined above without performing any restart. Thereafter, each of these estimated eigenvalues is used as the parameter  $k_{est}$  in the power iteration method with Wielandt's shift.

Further details about the procedure used in the tool to solve eigenvalue equations can be found in [11].

In order to benchmark the numerical algorithms used for estimating the solution to eigenvalue equations, a one-dimensional two-region system near to criticality was considered. The system was made of a central active core region of size  $2b = 322.5$  cm, surrounded on both sides by a reflector of thickness  $a - b = 118.25$  cm. The macroscopic cross-sections and diffusion coefficients were chosen to be representative of a typical LWR. The material data used in the benchmark are given in Table 2.3. The numerical solution was estimated with a node size of  $\Delta z = 0.5375$  cm.

**Table 2.3:** Values of the material data used in the static/dynamic benchmark in case of a one-dimensional two-region system near to criticality <sup>1</sup>.

	$D_{1,0}$ [cm]	$D_{2,0}$ [cm]	$\Sigma_{a,1,0}$ [cm <sup>-1</sup> ]	$\Sigma_{a,2,0}$ [cm <sup>-1</sup> ]	$\Sigma_r$ [cm <sup>-1</sup> ]	$v\Sigma_{f,1,0}$ [cm <sup>-1</sup> ]	$v\Sigma_{f,2,0}$ [cm <sup>-1</sup> ]
core	1.4376	0.3723	0.0115	0.1019	0.0151	0.0057	0.1425
reflector	1.3116	0.2624	-0.0098	0.0284	0.0238	0	0

<sup>1</sup> The negative value of the macroscopic absorption cross-section for the reflector region is the result of the homogenization of the material data from a three-dimensional heterogeneous system into a one-dimensional two-region system.

The reference solution, defined on  $z \in [-a - b; a + b]$ , is given by [20]:

$$\begin{bmatrix} \phi_{1,2m}(z) \\ \phi_{2,2m}(z) \end{bmatrix} = \begin{cases} A_1 \begin{bmatrix} 1 \\ c_{\mu_{2m}} \end{bmatrix} \cos(\mu_{2m}z) + A_2 \begin{bmatrix} 1 \\ c_{\eta_{2m}} \end{bmatrix} \frac{\cosh(\nu_{2m}z)}{\cosh(\nu_{2m}b)} \text{ for } -b \leq z \leq b \\ A_3 \begin{bmatrix} 1 \\ c_{\kappa} \end{bmatrix} \frac{\sinh[\kappa_1(|z|-a)]}{\sinh[\kappa_1(b-a)]} + A_4 \begin{bmatrix} 0 \\ 1 \end{bmatrix} \frac{\sinh[\kappa_2(|z|-a)]}{\sinh[\kappa_2(b-a)]} \text{ for } b < |z| < a \end{cases} \quad (2.65)$$

$$\begin{bmatrix} \phi_{1,2m+1}(z) \\ \phi_{2,2m+1}(z) \end{bmatrix} = \begin{cases} A_1 \begin{bmatrix} 1 \\ c_{\mu_{2m+1}} \end{bmatrix} \sin(\mu_{2m+1}z) + A_2 \begin{bmatrix} 1 \\ c_{\eta_{2m+1}} \end{bmatrix} \frac{\cosh(\nu_{2m+1}z)}{\cosh(\nu_{2m+1}b)} \text{ for } -b \leq z \leq b \\ A_3 \begin{bmatrix} 1 \\ c_{\kappa} \end{bmatrix} \frac{\sinh[\kappa_1(|z|-a)]}{\sinh[\kappa_1(b-a)]} + A_4 \begin{bmatrix} 0 \\ 1 \end{bmatrix} \frac{\sinh[\kappa_2(|z|-a)]}{\sinh[\kappa_2(b-a)]} \text{ for } b < |z| < a \end{cases} \quad (2.66)$$

for the forward problem [i.e. Eq. (2.38)]. Eq. (2.65) is written for the even-order eigenfunctions, whereas Eq. (2.66) is written for the odd-order eigenfunctions. In the previous equations, the different coefficients are given as:

$$\mu_m^2 = \frac{1}{2} \left[ - \left( \frac{1}{l_{1,m}^2} + \frac{1}{l_2^2} \right) + \sqrt{\left( \frac{1}{l_{1,m}^2} + \frac{1}{l_2^2} \right)^2 + \frac{4[\alpha_m - 1]}{l_{1,m}^2 \cdot l_2^2}} \right] \quad (\text{defined for } |z| < b) \quad (2.67)$$

$$\nu_m^2 = \frac{1}{2} \left[ \left( \frac{1}{l_{1,m}^2} + \frac{1}{l_2^2} \right) + \sqrt{\left( \frac{1}{l_{1,m}^2} + \frac{1}{l_2^2} \right)^2 + \frac{4[\alpha_m - 1]}{l_{1,m}^2 \cdot l_2^2}} \right] \quad (\text{defined for } |z| < b) \quad (2.68)$$

$$\kappa_1 = \sqrt{\frac{\Sigma_{a,1,0} + \Sigma_{r,0}}{D_{1,0}}} \quad (\text{defined for } b < |z| < a) \quad (2.69)$$

$$\kappa_2 = \sqrt{\frac{\Sigma_{a,2,0}}{D_{2,0}}} \quad (\text{defined for } b < |z| < a) \quad (2.70)$$

with

$$l_{1,m}^2 = \frac{D_{1,0}}{\Sigma_{a,1,0} + \Sigma_{r,0} - v\Sigma_{f,1,0}/k_m} \quad (\text{defined for } |z| < b) \quad (2.71)$$

$$l_2^2 = \frac{D_{2,0}}{\Sigma_{a,2,0}} \quad (\text{defined for } |z| < b) \quad (2.72)$$

$$\alpha_m = \frac{\Sigma_{r,0} \times v\Sigma_{f,2,0}/k_m}{(\Sigma_{a,1,0} + \Sigma_{r,0} - v\Sigma_{f,1,0}/k_m) \times \Sigma_{a,2,0}} \quad (\text{defined for } |z| < b) \quad (2.73)$$

The coupling coefficients are defined as:

$$c_{\mu_m} = \frac{\Sigma_{r,0}}{\Sigma_{a,2,0} + D_{2,0}\mu_m^2} \quad (\text{defined for } |z| < b) \quad (2.74)$$

$$c_{\nu_m} = \frac{\Sigma_{r,0}}{\Sigma_{a,2,0} - D_{2,0}\nu_m^2} \quad (\text{defined for } |z| < b) \quad (2.75)$$

$$c_{\kappa} = \frac{\Sigma_{r,0}}{D_{2,0} \times (\kappa_2^2 - \kappa_1^2)} \quad (\text{defined for } b < |z| < a) \quad (2.76)$$

The coefficients  $A_1 - A_4$  are solutions of four algebraic homogeneous equations expressing the interface conditions at  $z = \pm b$  (continuity of the flux and of the corresponding current, for both the fast and thermal groups). The determinant of the corresponding systems of equations thus needs to be equal to zero, from which  $k_m$  can be determined numerically.

The analytical and numerical solutions are given in Fig. 2.4, where a very good agreement can be noticed in terms of the computed space-dependence of the fast and thermal static neutron fluxes, as well as of the computed eigenvalue. The reflector peaks are clearly visible in the thermal group.

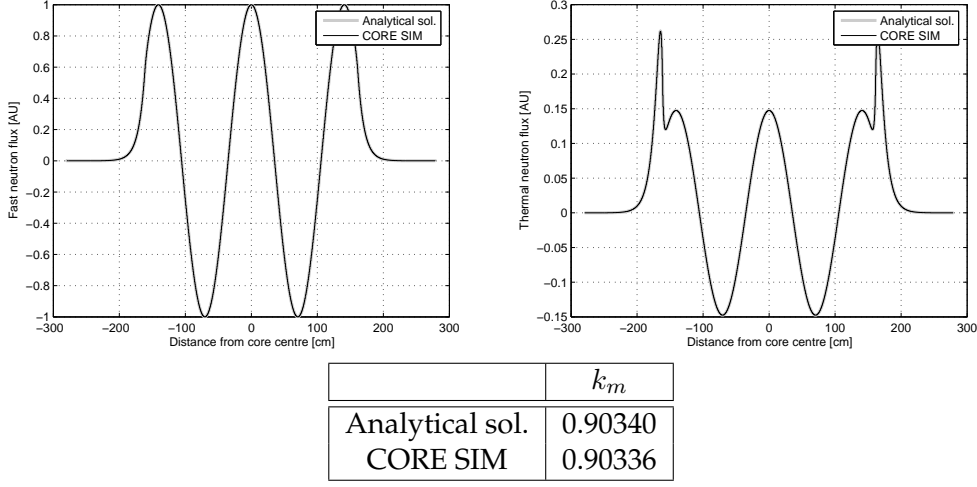


**Figure 2.4:** Results of the eigenfunction benchmark in case of a one-dimensional two-region critical system (forward problem); the results are only given for the fifth mode.

## 2.3 Modelling of dynamic core configurations

### 2.3.1 Subcritical systems with source

If the system is subcritical and driven by an external neutron source, using Eq. (2.5) for all time-dependent terms in Eqs. (2.1) - (2.3), removing the static equations [i.e. Eq. (2.18)], performing a temporal Fourier-transform, and neglecting second-order terms (linear theory), the following matrix equation is obtained:

$$\begin{aligned}
 & \left[ \nabla \cdot \overline{\overline{D}}(\bar{r}) \nabla + \overline{\overline{\Sigma}}_{dyn}^{sub}(\bar{r}, \omega) \right] \times \begin{bmatrix} \delta\phi_1(\bar{r}, \omega) \\ \delta\phi_2(\bar{r}, \omega) \end{bmatrix} \\
 & = - \begin{bmatrix} \delta S_1(\bar{r}, \omega) \\ \delta S_2(\bar{r}, \omega) \end{bmatrix} + \overline{\overline{\phi}}_r(\bar{r}) \delta\Sigma_r(\bar{r}, \omega) + \overline{\overline{\phi}}_a(\bar{r}) \begin{bmatrix} \delta\Sigma_{a,1}(\bar{r}, \omega) \\ \delta\Sigma_{a,2}(\bar{r}, \omega) \end{bmatrix} + \overline{\overline{\phi}}_f^{sub}(\bar{r}, \omega) \begin{bmatrix} \delta v\Sigma_{f,1}(\bar{r}, \omega) \\ \delta v\Sigma_{f,2}(\bar{r}, \omega) \end{bmatrix}
 \end{aligned} \tag{2.77}$$

with

$$\overline{\overline{\Sigma}}_{dyn}^{sub}(\bar{r}, \omega) = \begin{bmatrix} -\Sigma_1^{sub}(\bar{r}, \omega) & v\Sigma_{f,2,0}(\bar{r}) \left(1 - \frac{i\omega\beta}{i\omega + \lambda}\right) \\ \Sigma_{r,0}(\bar{r}) & -\left(\Sigma_{a,2,0}(\bar{r}) + \frac{i\omega}{v_2}\right) \end{bmatrix} \tag{2.78}$$

$$\overline{\overline{\phi}}_r(\bar{r}) = \begin{bmatrix} \phi_{1,0}(\bar{r}) \\ -\phi_{1,0}(\bar{r}) \end{bmatrix} \tag{2.79}$$

$$\overline{\overline{\phi}}_a(\bar{r}) = \begin{bmatrix} \phi_{1,0}(\bar{r}) & 0 \\ 0 & \phi_{2,0}(\bar{r}) \end{bmatrix} \tag{2.80}$$

$$\overline{\overline{\phi}}_f^{sub}(\bar{r}, \omega) = \begin{bmatrix} \phi_{1,0}(\bar{r}) \left(1 - \frac{i\omega\beta}{i\omega + \lambda}\right) & -\phi_{2,0}(\bar{r}) \left(1 - \frac{i\omega\beta}{i\omega + \lambda}\right) \\ 0 & 0 \end{bmatrix} \tag{2.81}$$

and with

$$\Sigma_1^{sub}(\bar{r}, \omega) = \Sigma_{a,1,0}(\bar{r}) + \frac{i\omega}{v_1} + \Sigma_{r,0}(\bar{r}) - v\Sigma_{f,1,0}(\bar{r}) \times \left(1 - \frac{i\omega\beta}{i\omega + \lambda}\right) \tag{2.82}$$

The right-hand side of Eq. (2.77) gives the neutron noise source, resulting from either the fluctuations of the external neutron source around its mean value, or from the fluctuations of the macroscopic cross-sections (removal, absorption, and fission) around their mean value. Although the effect of the fluctuations of the macroscopic fission cross-sections and of the macroscopic absorption cross-sections are given by two separate terms in Eq. (2.77), any fluctuation in the macroscopic fission cross-section has also an impact on the macroscopic absorption cross-section (since fission is a special type of absorption).

An adjoint problem associated with the forward problem as given by Eq. (2.77) can then be formally written as:

$$\left[ \nabla \cdot \overline{\overline{D}}(\bar{r}) \nabla + \overline{\overline{\Sigma}}_{dyn}^{sub\dagger}(\bar{r}, \omega) \right] \times \begin{bmatrix} \delta\phi_1^\dagger(\bar{r}, \omega) \\ \delta\phi_2^\dagger(\bar{r}, \omega) \end{bmatrix} = - \begin{bmatrix} \delta S_1^\dagger(\bar{r}, \omega) \\ \delta S_2^\dagger(\bar{r}, \omega) \end{bmatrix} \quad (2.83)$$

where

$$\overline{\overline{\Sigma}}_{dyn}^{sub\dagger}(\bar{r}, \omega) = \overline{\overline{\Sigma}}_{dyn}^{sub,T}(\bar{r}, \omega) \quad (2.84)$$

From a mathematical viewpoint, the dynamic forward problem of a subcritical source-driven system and the corresponding adjoint problem, as given by Eqs. (2.77) and (2.83), respectively, are represented after spatial discretisation by non-homogeneous equations as:

$$\overline{\overline{M}}_{dyn}^{sub} \times \overline{\delta\phi} = \overline{\delta S} \text{ and } \overline{\overline{M}}_{dyn}^{sub\dagger} \times \overline{\delta\phi}^\dagger = \overline{\delta S}^\dagger \quad (2.85)$$

The same techniques as the ones described in Section 3.1 can be used to solve such equations.

### 2.3.2 Critical systems

If the neutron noise is induced by perturbations of the macroscopic cross-sections and if there is no external neutron source, then splitting the time-dependent parameters into mean values and fluctuations according to Eq. (2.5), removing the static equations [i.e. Eq. (2.38) taken with  $n = 0$ ], performing a temporal Fourier-transform, and neglecting second-order terms (linear theory), the following matrix equation is obtained:

$$\begin{aligned} & \left[ \nabla \cdot \overline{\overline{D}}(\bar{r}) \nabla + \overline{\overline{\Sigma}}_{dyn}^{crit}(\bar{r}, \omega) \right] \times \begin{bmatrix} \delta\phi_1(\bar{r}, \omega) \\ \delta\phi_2(\bar{r}, \omega) \end{bmatrix} \\ & = \overline{\phi}_r(\bar{r}) \delta\Sigma_r(\bar{r}, \omega) + \overline{\phi}_a(\bar{r}) \begin{bmatrix} \delta\Sigma_{a,1}(\bar{r}, \omega) \\ \delta\Sigma_{a,2}(\bar{r}, \omega) \end{bmatrix} + \overline{\phi}_f^{crit}(\bar{r}, \omega) \begin{bmatrix} \delta v\Sigma_{f,1}(\bar{r}, \omega) \\ \delta v\Sigma_{f,2}(\bar{r}, \omega) \end{bmatrix} \end{aligned} \quad (2.86)$$

When deriving this equation for the neutron noise, the system is assumed to be critical without source, since the system is supposed to be stationary. This means that Eq. (2.38) is assumed to be verified with  $k_0 = k_{eff} = 1$  for  $m = 0$ . In reality, it is very unlikely that the eigenvalue of the first eigenmode is exactly equal to unity. Furthermore, Eq. (2.86) has to be spatially discretized, and such a spatial discretisation might also lead to a discretized system deviating from criticality, even if the non-discretized system was exactly critical. One way to cope with this difficulty is to re-normalize the macroscopic fission cross-sections with  $k_{eff}$ , i.e. to replace in all equations  $v\Sigma_{f,g}(\bar{r}, t)$  by  $v\Sigma_{f,g}(\bar{r}, t) / k_{eff}$ . This re-normalization guarantees that the discretized system is stationary. Therefore, the matrix

$\overline{\overline{\Sigma}}_{dyn}^{crit}$  is defined as:

$$\overline{\overline{\Sigma}}_{dyn}^{crit}(\bar{r}, \omega) = \begin{bmatrix} -\Sigma_1^{crit}(\bar{r}, \omega) & \frac{v\Sigma_{f,2,0}(\bar{r})}{k_{eff}} \left(1 - \frac{i\omega\beta}{i\omega + \lambda}\right) \\ \Sigma_{r,0}(\bar{r}) & -\left(\Sigma_{a,2,0}(\bar{r}) + \frac{i\omega}{v_2}\right) \end{bmatrix} \quad (2.87)$$

with

$$\Sigma_1^{crit}(\bar{r}, \omega) = \Sigma_{a,1,0}(\bar{r}) + \frac{i\omega}{v_1} + \Sigma_{r,0}(\bar{r}) - \frac{v\Sigma_{f,1,0}(\bar{r})}{k_{eff}} \left(1 - \frac{i\omega\beta}{i\omega + \lambda}\right) \quad (2.88)$$

and the matrix  $\overline{\overline{\phi}}_f^{crit}$  is given as:

$$\overline{\overline{\phi}}_f^{crit}(\bar{r}, \omega) = \begin{bmatrix} -\frac{\phi_{1,0}(\bar{r})}{k_{eff}} \left(1 - \frac{i\omega\beta}{i\omega + \lambda}\right) & -\frac{\phi_{2,0}(\bar{r})}{k_{eff}} \left(1 - \frac{i\omega\beta}{i\omega + \lambda}\right) \\ 0 & 0 \end{bmatrix} \quad (2.89)$$

The expressions for  $\overline{\overline{\phi}}_r(\bar{r})$  and  $\overline{\overline{\phi}}_a(\bar{r})$  are identical to the ones given by Eqs. (2.79) and (2.80), respectively. The right-hand side of Eq. (2.86) gives the neutron noise source, resulting from the fluctuations of the macroscopic cross-sections (removal, absorption, and fission) around their mean value. Although the effect of the fluctuations of the macroscopic fission cross-sections and of the macroscopic absorption cross-sections are given by two separate terms in Eq. (2.86), any fluctuation in the macroscopic fission cross-section has also an impact on the macroscopic absorption cross-section (since fission is a special type of absorption).

An adjoint problem associated with the forward problem as given by Eq. (2.86) can then be formally written as:

$$\left[ \nabla \cdot \overline{\overline{D}}(\bar{r}) \nabla + \overline{\overline{\Sigma}}_{dyn}^{crit\dagger}(\bar{r}, \omega) \right] \times \begin{bmatrix} \delta\phi_1^\dagger(\bar{r}, \omega) \\ \delta\phi_2^\dagger(\bar{r}, \omega) \end{bmatrix} = - \begin{bmatrix} \delta S_1^\dagger(\bar{r}, \omega) \\ \delta S_2^\dagger(\bar{r}, \omega) \end{bmatrix} \quad (2.90)$$

where

$$\overline{\overline{\Sigma}}_{dyn}^{crit\dagger}(\bar{r}, \omega) = \overline{\overline{\Sigma}}_{dyn}^{crit,T}(\bar{r}, \omega) \quad (2.91)$$

From a mathematical viewpoint, the dynamic forward problem of a critical system and the corresponding adjoint problem, as given by Eqs. (2.86) and (2.90), respectively, are represented after spatial discretisation by non-homogeneous equations as:

$$\overline{\overline{M}}_{dyn}^{crit} \times \overline{\delta\phi} = \overline{\delta S} \text{ and } \overline{\overline{M}}_{dyn}^{crit\dagger} \times \overline{\delta\phi}^\dagger = \overline{\delta S}^\dagger \quad (2.92)$$

The same techniques as the ones described in Section 2.2.1 can be used to solve such equations.

Although the numerical algorithms used for estimating the solution to non-homogeneous equations were already benchmarked (see Section 2.2.1), an additional dynamic benchmark is presented hereafter, since the dynamic capabilities of the tool in the frequency-domain makes the tool rather unique. The benchmark actually corresponds to the modelling of shell-mode core barrel vibrations at 20 Hz in Pressurized Water Reactors (further details about the modelling of such vibrations can be found in [21, 22]). A one-dimensional two-region system near to criticality was considered. The system was made of a central active core region of size  $2b = 322.5$  cm, surrounded on both sides by a reflector of thickness  $a - b = 118.25$  cm. The macroscopic cross-sections and diffusion coefficients were chosen to be representative of a typical LWR, and were already given in Table

2.2. The additional kinetic data required to perform the dynamic calculations are given in Table 2.4. The numerical solution was estimated with a node size of  $\Delta z = 0.05$  cm.

**Table 2.4:** Values of the kinetic data used in the dynamic benchmark in case of a one-dimensional two-region system near to criticality.

$v_1$ [cm.s <sup>-1</sup> ]	$v_2$ [cm.s <sup>-1</sup> ]	$\beta$ [pcm]	$\lambda$ [s <sup>-1</sup> ]
1.82304x10 <sup>7</sup>	4.13067x10 <sup>5</sup>	535	0.08510

The reference solution to the forward problem [i.e. Eq. (2.86)], defined on  $z \in [-a - b; a + b]$  and for two identical point-like 20 Hz perturbations located at the interfaces core/reflector in  $z' = \pm b$ , is given by [21]:

$$\begin{bmatrix} \delta\phi_1(z, \omega) \\ \delta\phi_2(z, \omega) \end{bmatrix} = \begin{cases} A_1 \begin{bmatrix} 1 \\ c_\mu(\omega) \end{bmatrix} \cos[\mu(\omega)z] + A_2 \begin{bmatrix} 1 \\ c_\eta(\omega) \end{bmatrix} \frac{\cosh[\nu(\omega)z]}{\cosh[\nu(\omega)b]} \text{ for } -b \leq z \leq b \\ A_3 \begin{bmatrix} 1 \\ c_\kappa(\omega) \end{bmatrix} \frac{\sinh[\kappa_1(\omega)(|z|-a)]}{\sinh[\kappa_1(\omega)(b-a)]} + A_4 \begin{bmatrix} 0 \\ 1 \end{bmatrix} \frac{\sinh[\kappa_2(\omega)(|z|-a)]}{\sinh[\kappa_2(\omega)(b-a)]} \text{ for } b < |z| < a \end{cases} \quad (2.93)$$

In the previous equations, the different coefficients are given as:

$$\mu^2(\omega) = \frac{1}{2} \left[ - \left( \frac{1}{l_1^2(\omega)} + \frac{1}{l_2^2(\omega)} \right) + \sqrt{\left( \frac{1}{l_1^2(\omega)} + \frac{1}{l_2^2(\omega)} \right)^2 + \frac{4[k(\omega) - 1]}{l_1^2(\omega) \cdot l_2^2(\omega)}} \right] \text{ (defined for } |z| < b) \quad (2.94)$$

$$\nu^2(\omega) = \frac{1}{2} \left[ \left( \frac{1}{l_1^2(\omega)} + \frac{1}{l_2^2(\omega)} \right) + \sqrt{\left( \frac{1}{l_1^2(\omega)} + \frac{1}{l_2^2(\omega)} \right)^2 + \frac{4[k(\omega) - 1]}{l_1^2(\omega) \cdot l_2^2(\omega)}} \right] \text{ (defined for } |z| < b) \quad (2.95)$$

$$\kappa_1(\omega) = \sqrt{\frac{\Sigma_{a,1,0} + \Sigma_{r,0} + \frac{i\omega}{v_1}}{D_{1,0}}} \text{ (defined for } b < |z| < a) \quad (2.96)$$

$$\kappa_2(\omega) = \sqrt{\frac{\Sigma_{a,2,0} + \frac{i\omega}{v_2}}{D_{2,0}}} \text{ (defined for } b < |z| < a) \quad (2.97)$$

with

$$l_1^2(\omega) = \frac{D_{1,0}}{\Sigma_{a,1,0} + \Sigma_{r,0} + \frac{i\omega}{v_1} - \frac{v\Sigma_{f,1,0}}{k_{eff}} \times \left( 1 - \frac{i\omega\beta}{i\omega + \lambda} \right)} \text{ (defined for } |z| < b) \quad (2.98)$$

$$l_2^2(\omega) = \frac{D_{2,0}}{\Sigma_{a,2,0} + \frac{i\omega}{v_2}} \text{ (defined for } |z| < b) \quad (2.99)$$

$$k(\omega) = \frac{\Sigma_{r,0} \times \frac{v\Sigma_{f,2,0}}{k_{eff}} \times \left( 1 - \frac{i\omega\beta}{i\omega + \lambda} \right)}{\left[ \Sigma_{a,1,0} + \Sigma_{r,0} + \frac{i\omega}{v_1} - \frac{v\Sigma_{f,1,0}}{k_{eff}} \times \left( 1 - \frac{i\omega\beta}{i\omega + \lambda} \right) \right] \times \left( \Sigma_{a,2,0} + \frac{i\omega}{v_2} \right)} \text{ (defined for } |z| < b) \quad (2.100)$$

The coupling coefficients are defined as:

$$c_\mu(\omega) = \frac{\Sigma_{r,0}}{\Sigma_{a,2,0} + \frac{i\omega}{v_2} + D_{2,0}\mu^2(\omega)} \text{ (defined for } |z| < b) \quad (2.101)$$

$$c_\nu(\omega) = \frac{\Sigma_{r,0}}{\Sigma_{a,2,0} + \frac{i\omega}{v_2} - D_{2,0}\nu^2(\omega)} \quad (\text{defined for } |z| < b) \quad (2.102)$$

$$c_\kappa(\omega) = \frac{\Sigma_{r,0}}{D_{2,0} \times [\kappa_2^2(\omega) - \kappa_1^2(\omega)]} \quad (\text{defined for } b < |z| < a) \quad (2.103)$$

The coefficients  $A_1 - A_4$  are solutions of the following equation, where the explicit dependence on frequency was dropped for the sake of clarity:

$$\begin{bmatrix} -\cos(\mu b) & -1 & 1 & 0 \\ -c_\mu \cos(\mu b) & -c_\nu & c_\kappa & 1 \\ \mu D_{1,0}^c \sin(\mu b) & -\nu D_{1,0}^c \tanh(\nu b) & \kappa_1 D_{1,0}^r \coth[\kappa_1(b-a)] & 0 \\ c_\mu \mu D_{2,0}^c \sin(\mu b) & -c_\nu \nu D_{2,0}^c \tanh(\nu b) & c_\kappa \kappa_1 D_{2,0}^r \coth[\kappa_1(b-a)] & \kappa_1 D_{2,0}^r \coth[\kappa_1(b-a)] \end{bmatrix} \times \begin{bmatrix} A_1 \\ A_2 \\ A_3 \\ A_4 \end{bmatrix} = \begin{bmatrix} 0 \\ 0 \\ \delta S_1 \\ \delta S_2 \end{bmatrix} \quad (2.104)$$

In this equation,  $D_{1,0}^c$  and  $D_{2,0}^c$  represent the static diffusion coefficients in the core region, for the fast and thermal groups, respectively, whereas  $D_{1,0}^r$  and  $D_{2,0}^r$  represent the static diffusion coefficients in the reflector region, for the fast and thermal groups, respectively. The parameters  $\delta S_1$  and  $\delta S_2$  allow expressing the relative strength of the point-like noise sources in the fast and thermal problems, respectively, and are defined as the difference between the material data of the core and of the reflector (see [21,22] for further details). Such a definition of the noise sources allows representing the moving core/reflector interfaces.

The comparison between the semi-analytical and numerical solutions for one half of the core is given in Fig. 2.5, where a very good agreement can be noticed between both solutions, both for the amplitude and phase of the fast and thermal neutron noise. Although the results are presented in arbitrary units, the analytical and numerical solutions were not scaled between each other. The reason of the out-of-phase behavior of the local component of the thermal neutron noise that can be observed lies with the fact that an increase of the size of the core region (and thus a decrease of the size of the reflector region) is accompanied by increased production of neutrons by fissions (leading to a positive reactivity effect), but at the same time by increased thermal absorptions. Since the core-wise neutron noise is related to the point-kinetic component (i.e. reactivity term) of the neutron noise, the local component of the thermal neutron noise thus exhibits an out-of-phase behavior compared to the core-wise neutron noise. Further explanations of this effect can be found in [21].

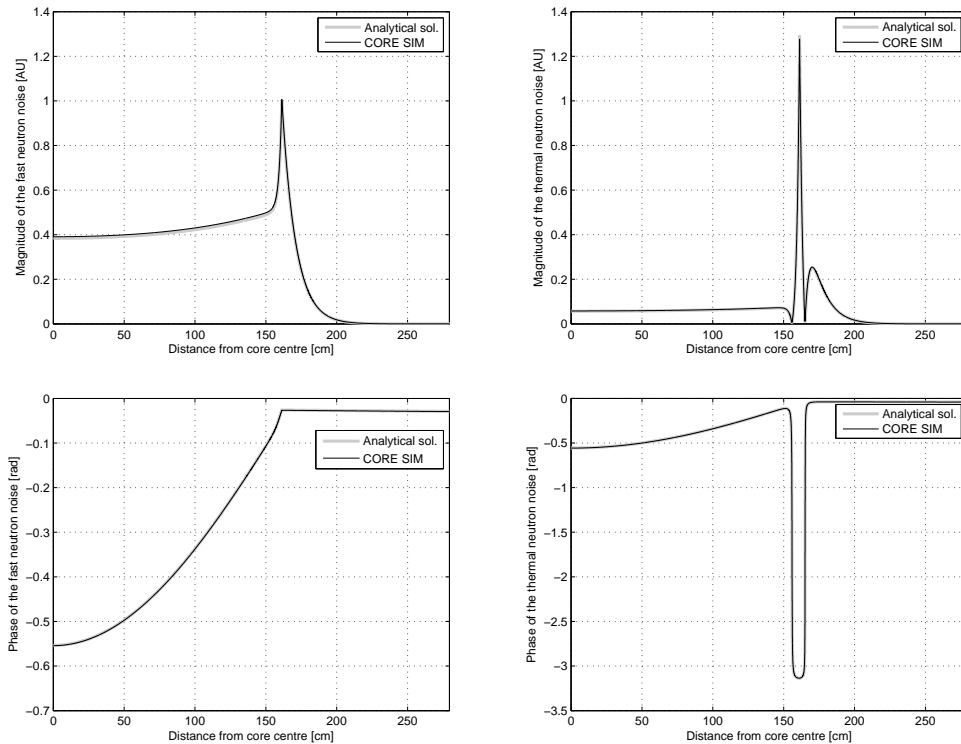


**Figure 2.5:** Results of the dynamic benchmark in case of a one-dimensional two-region critical system (forward problem).

## 2.4 Use and demonstration of the tool

The computational tool presented above is delivered with a complete user's guide [23] explaining the required software/hardware, what the code package contains, the file architecture and required input, the created output, the format of the input and output variables, the variables necessary in the input files, the available variables in the output file, and how to use the code. Some examples are also available within the package.

The main feature of the computational tool is its flexibility and its simplicity in use, since there is no need of writing any input deck. Data input should be provided by the user in a few data files describing the three-dimensional distributions of the macroscopic cross-sections throughout the system, as well as its geometry. Some additional optional files should also be provided for defining possible external neutron sources and their possible fluctuations, for defining possible sources in the static and dynamic adjoint problems, as well as for defining some additional kinetic data necessary for calculating the neutron noise. The presence of such files automatically triggers the corresponding optional calculations.

Prior to use the tool, the user might want to change some default settings and/or fine-tune some parameters related to the numerical techniques implemented in the code. For the latter, the parameters are mostly related to the explicitly-restarted Arnoldi method and to the power iteration method with Wielandt's shift technique. These parameters might need to be changed in case of convergence problems.

After the successful run of the tool, a GUI can be used for visualizing both input and output variables in a rather intuitive manner. The input data include the static two-group macroscopic cross-sections, the possible external neutron sources, and the possible noise sources defined as perturbations of these cross-sections/neutron sources. The output data include the static neutron flux, the different eigenmodes, the induced neutron noise, their adjoints, and the different eigenvalues. Due to the three-dimensional nature of the system, the visualization of the input and output data has to be very flexible, so that the input and output data can be visualized at different locations through the system in a rather intuitive manner. A snapshot of the GUI is presented in Fig. 2.6. A panel allows choosing the row, column, and level at which cross-sections of the chosen input or output variable will be plotted. Furthermore, since the neutron noise is evaluated in the frequency domain and some quantities might thus be complex, the user has to choose whether the magnitude or the phase has to be plotted. An automatic sweep through the whole system can also be performed, in order to find possible local effects corresponding to the computed case. Three plots are given: a three-dimensional plot on the left-hand side (with planar cross-sectional cuts at the chosen row, column, and level), a two-dimensional plot in the middle (at the chosen level), and a one-dimensional plot on the right-hand side (at the chosen row and column).

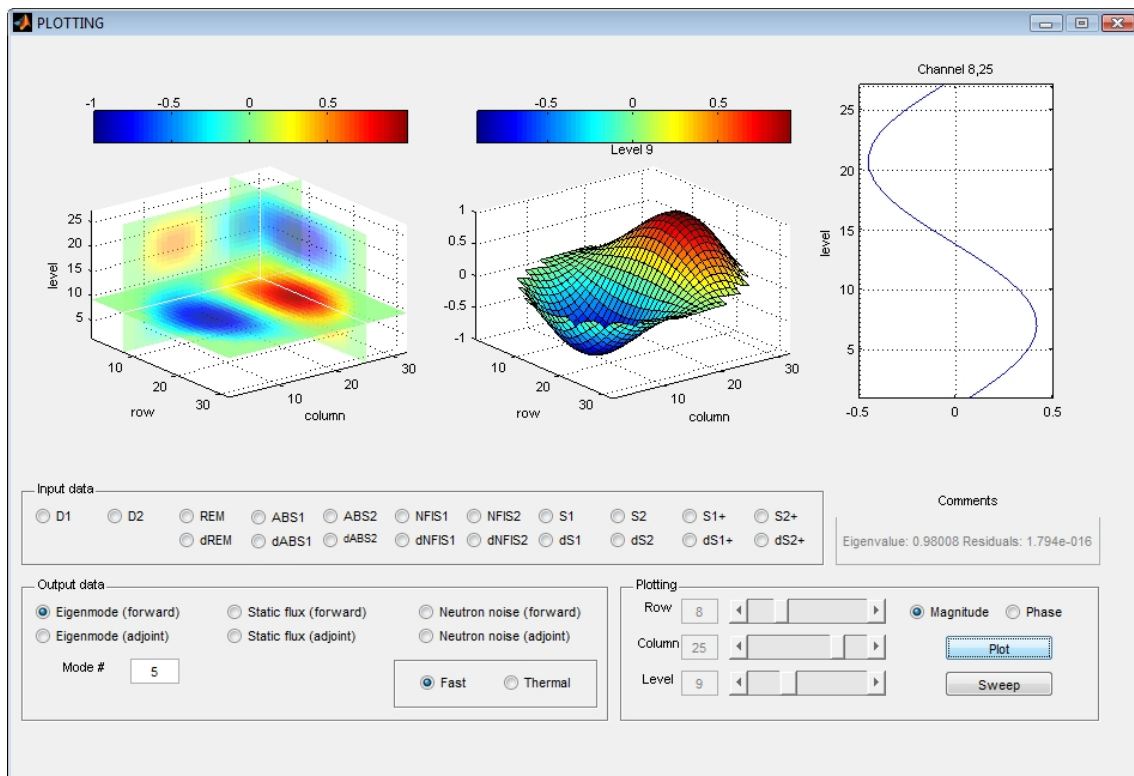


**Figure 2.6:** Overview of the Graphical User Interface (GUI) for the visualization of both input and output data in the computational tool.



# MODELING OF GLOBAL AND REGIONAL INSTABILITIES VIA ROM

A cursory description of the four heated channel reduced order model developed in this project and consisting of three separate submodels for the neutron transport, heat transfer and flow transport, is given hereafter. Some details regarding the development of the ROM are touched upon. Careful attention is paid to the new features implemented, compared to already existing models. Some results of the applications of the ROM to study core-wide instabilities are also discussed.

## 3.1 Neutron kinetic model

This Section gives a brief overview of the neutron-kinetic model, implemented in the ROM. First, the procedure, which is applied to derive the ordinary differential equations from the 3D partial differential reactor-dynamic equations and the assumptions which are needed to be made, are described. One starts with the three-dimensional time-dependent two-energy group diffusion equations, written in the operator (matrix) form as [4,27]:

$$\begin{aligned} \bar{v}^{*-1} \cdot \frac{\partial \bar{\Psi}^*(\bar{r}^*, t^*)}{\partial t^*} &= [(1 - \beta^*) \cdot \bar{F}^*(\bar{r}^*, t^*) - \bar{L}^*(\bar{r}^*, t^*)] \cdot \bar{\Psi}^*(\bar{r}^*, t^*) \\ &+ \sum_{l=1}^6 \lambda_l^* \cdot C_l^*(\bar{r}^*, t^*) \cdot \bar{X}, \end{aligned} \quad (3.1)$$

$$\frac{\partial C_l^*(\bar{r}^*, t^*)}{\partial t^*} \cdot \bar{X} = \beta_l^* \cdot \bar{F}^*(\bar{r}^*, t^*) \cdot \bar{\Psi}^*(\bar{r}^*, t^*) - \lambda_l^* \cdot C_l^*(\bar{r}^*, t^*) \cdot \bar{X}, \quad (3.2)$$

where  $\bar{\Psi}^*(\bar{r}^*, t^*)$  is the neutron flux vector which consists of the fast  $\Psi_1^*(\bar{r}^*, t^*)$  and thermal  $\Psi_2^*(\bar{r}^*, t^*)$  neutron fluxes,  $\bar{L}(\bar{r}, t)$  is the net loss matrix operator, which represents the neutron leakage through diffusion, scattering and absorption,  $\bar{F}(\bar{r}, t)$  is the fission production matrix operator, which represents the neutron production through fission reactions,  $C_l^*(\bar{r}^*, t^*)$  is the concentration for the  $l$ th delayed neutron precursor group and  $\bar{X}$

is a unit vector. The rest of the notations are standard. From now on, an asterisk stands for the dimensional quantities, otherwise they are considered to be dimensionless.

Applying first-order perturbation theory, namely assuming small fluctuations of the neutron flux  $\bar{\Psi}^*(\bar{r}^*, t^*)$  and  $C_l^*(\bar{r}^*, t^*)$  around their steady state values, due to perturbations in both the fission  $\bar{F}^*(\bar{r}^*, t^*)$  and net loss  $\bar{L}^*(\bar{r}^*, t^*)$  operators and taking into account static equations, the following equations for the fluctuating parts  $\delta\bar{\Psi}^*(\bar{r}^*, t^*)$  and  $\delta C_l^*(\bar{r}^*, t^*)$  can be obtained:

$$\bar{v}^{*-1} \cdot \frac{\partial \delta\bar{\Psi}^*(\bar{r}^*, t^*)}{\partial t^*} = [(1 - \beta^*) \cdot \delta\bar{F}^*(\bar{r}^*, t^*) - \delta\bar{L}^*(\bar{r}^*, t^*)] \cdot (\bar{\Phi}_0^*(\bar{r}^*) + \delta\bar{\Psi}^*(\bar{r}^*, t^*)) + \lambda \cdot \delta C_l^*(\bar{r}^*, t^*) \cdot \bar{X} + [(1 - \beta^*) \cdot \bar{F}_0^*(\bar{r}^*, t^*) - \bar{L}_0^*(\bar{r}^*, t^*)] \cdot \delta\bar{\Psi}^*(\bar{r}^*, t^*), \quad (3.3)$$

$$\frac{\partial \delta C_l^*(\bar{r}^*, t^*)}{\partial t^*} \cdot \bar{X} = \beta^* \cdot \delta\bar{F}^*(\bar{r}^*, t^*) \cdot (\bar{\Phi}_0^*(\bar{r}^*) + \delta\bar{\Psi}^*(\bar{r}^*, t^*)) - \lambda \cdot \delta C_l^*(\bar{r}^*, t^*) \cdot \bar{X} + \beta^* \cdot \bar{F}_0^*(\bar{r}^*) \cdot \delta\bar{\Psi}^*(\bar{r}^*, t^*). \quad (3.4)$$

Next, one expands both the space-time dependent neutron flux  $\delta\bar{\Psi}^*(\bar{r}^*, t^*)$ , as well as the space-time dependent concentration of the delayed neutron precursors  $\delta C_l^*(\bar{r}^*, t^*)$  in terms of lambda (reactivity) modes as:

$$\delta\bar{\Psi}^*(\bar{r}^*, t^*) = \sum_{n=0}^{\infty} \bar{P}_n^*(t^*) \cdot \bar{\Phi}_n^*(\bar{r}^*), \quad (3.5)$$

$$\delta C_l^*(\bar{r}^*, t^*) \cdot \bar{X} = \sum_{n=0}^{\infty} C_{nl}^*(t^*) \cdot \bar{F}_0^*(\bar{r}^*) \cdot \bar{\Phi}_n^*(\bar{r}^*) \cdot \Lambda_n^*, \quad (3.6)$$

where  $\bar{\Phi}_n^*(\bar{r}^*)$  is the eigenvector, satisfying the corresponding  $\lambda$  eigenvalue problem.

Substituting Eqs. (3.5) and (3.6) into Eqs. (3.3) and (3.4), multiplying the resulting equation by the adjoint eigenmode  $\bar{\Phi}_m^{\dagger}(\bar{r}^*)$ , assuming one group of delayed neutron precursors, after integration and some rearrangements, one gets the following dimensionless point-kinetic equations:

$$\frac{dP_m(t)}{dt} = \frac{1}{\Lambda_m} (\rho_m^s - \beta) P_m(t) + \frac{1}{\Lambda_m} \sum_{n=0}^2 \rho_{mn}^F(t) P_n(t) + \lambda C_m(t), \quad (3.7)$$

$$\frac{dC_m(t)}{dt} = \frac{\beta}{\Lambda_m} P_m(t) - \lambda C_m(t), \quad (3.8)$$

where  $m = 0, 1, 2$  is the mode number,  $\rho_m^s$  is the static reactivity,  $\rho_{mn}^F$  are the dynamic feedback reactivities and  $\Lambda_m = \Lambda_{mm}$  (for  $m = 0$   $\Lambda_m$  gives the prompt neutron generation time). The dynamic feedback reactivities  $\rho_{mn}^F$  reflect the feedback mechanism between the neutron kinetics and thermal-hydraulics in terms of void fraction and fuel temperature. In the linear approximation, the feedback reactivities for both void fraction and fuel temperature can be expressed, respectively, as:

$$\begin{aligned} \rho_{mn}^F(t) &= \rho_{mn}^V(t)|_{T_f(t)=const} + \rho_{mn}^D(t)|_{\alpha(t)=const} \\ &= \sum_{l=1}^4 C_{mn,l}^V (\alpha_l(t) - \alpha_0) + \sum_{l=1}^4 C_{mn,l}^D (T_{f,l}(t) - T_{f0}), \end{aligned} \quad (3.9)$$

where  $l$  stands for the channel number and  $\alpha_0$  and  $T_{f0}$  are the steady-state void fraction and fuel temperature, correspondingly. The reactivity coupling coefficients  $C_{mn,l}^{*V,T}$  were estimated numerically utilizing the cross-section data from SIMULATE-3 and spatial distribution of the eigenmodes from CORE SIM. A more detailed derivation can be found in [25,26].

## 3.2 Heat transfer model

In the following, the main steps needed to be undertaken to convert the partial differential equations, describing the heat conduction in the fuel rod, into the corresponding ordinary differential equations, are described. The necessary assumptions and mathematical tricks which have to be applied are also discussed. To begin with, the general three-dimensional time-/space-dependent energy balance equation, written for a single fuel rod, reads as [4,24]:

$$\rho^* c_p^* \frac{\partial}{\partial t^*} T^*(\bar{r}^*, t^*) = q^{*''' }(\bar{r}^*, t^*) - \bar{\nabla}^* \cdot \bar{q}^{*'' }(\bar{r}^*, t^*), \quad (3.10)$$

where  $\rho^*$  is the density of the rod fuel,  $c_p^*$  is the specific heat of the fuel rod at constant pressure,  $q^{*''' }(\bar{r}^*, t^*)$  is the volumetric heat production per unit time and per unit fuel rod volume, and  $\bar{q}^{*'' }(\bar{r}^*, t^*)$  is the heat flux from the fuel rod surface area.

Next, neglecting the axial heat conduction and assuming azimuthal symmetry, the fuel pellet temperature distribution can be approximated through two piece-wise quadratic spatial functions with time-dependent expansion coefficients, written as:

$$\Theta_p(r, t) = \begin{cases} T_1(t) + \eta_1(t)r + \eta_2(t)r^2 & \text{if } 0 < r < r_d, \\ T_2(t) + \sigma_1(t)r + \sigma_2(t)r^2 & \text{if } r_d < r < r_p. \end{cases} \quad (3.11)$$

Here, one notes that the time dependent expansion coefficients  $\eta_i(t)$  and  $\sigma_i(t)$ ,  $i = \overline{1, 2}$  can be expressed through the  $T_i(t)$ ,  $i = \overline{1, 2}$  and system (design) parameters, utilizing the discontinuity and boundary conditions.

Then, taking into account that there are three radial regions in the fuel rod (i.e. fuel pellet  $0 < r < r_p$ , fuel gap  $r_p < r < r_g$  and fuel cladding  $r_g < r < r_p$ ), after the application of the variational principle, the following reduced differential equations for  $T_i(t)$ , describing the fuel rod conduction dynamics, are obtained:

$$\frac{dT_{1,l,j\phi}(t)}{dt} = p_{11,j\phi} T_{1,l,j\phi}(t) + p_{21,j\phi} T_{2,l,j\phi}(t) + p_{31,j\phi} c_q \sum_{i=0}^2 \xi_i (P_i(t) - \tilde{P}_i), \quad (3.12)$$

$$\frac{dT_{2,l,j\phi}(t)}{dt} = p_{12,j\phi} T_{1,l,j\phi}(t) + p_{22,j\phi} T_{2,l,j\phi}(t) + p_{32,j\phi} c_q \sum_{i=0}^2 \xi_i (P_i(t) - \tilde{P}_i), \quad (3.13)$$

where  $p_{ij}$  are complicated coefficients which depend on the design and operational parameters,  $j\phi$  stands for the single- ( $1\phi$ ) or two-phase ( $2\phi$ ) regions,  $l$  is the channel number (varying between 1 and 4), and  $\tilde{P}_0$  is the steady state value of the fundamental mode.

### 3.3 Thermo-hydraulic model

In this Section, the description of the thermal-hydraulic model for the present ROM is given. Since there are two axial coolant regions assumed in the channel, namely single-phase and two-phase regions, with a constant flow cross section, the description is performed in two separate sections, respectively. Within the scope of this Section, the procedure to transform the PDEs, describing thermal-hydraulic processes, into simplified ODEs, applying the variational method, is demonstrated.

#### 3.3.1 Single-phase region

One starts with three local conservation equations written for mass, momentum and energy, respectively, as [4, 24]:

$$\frac{\partial \rho^*(\bar{r}^*, t^*)}{\partial t^*} + \bar{\nabla}^* \cdot (\rho^* \bar{v}^*)(\bar{r}^*, t^*) = 0, \quad (3.14)$$

$$\begin{aligned} & \frac{\partial (\rho^* \bar{v}^*)}{\partial t^*}(\bar{r}^*, t^*) + \bar{\nabla}^* \cdot (\rho^* \bar{v}^* \otimes \bar{v}^*)(\bar{r}^*, t^*) \\ &= \bar{\nabla}^* \cdot \bar{\bar{r}}^*(\bar{r}^*, t^*) - \bar{\nabla}^* \cdot (P^*(\bar{r}^*, t^*) \bar{I}) + \rho^*(\bar{r}^*, t^*) \bar{g}^*, \end{aligned} \quad (3.15)$$

$$\begin{aligned} & \frac{\partial (\rho^* e^*)}{\partial t^*}(\bar{r}^*, t^*) + \bar{\nabla}^* \cdot (\rho^* e^* \bar{v}^*)(\bar{r}^*, t^*) = -\bar{\nabla}^* \cdot \bar{q}^{*''}(\bar{r}^*, t^*) \\ & + \bar{q}^{*''''}(\bar{r}^*, t^*) + \bar{\nabla}^* \cdot (\bar{\bar{r}}^* \cdot \bar{v}^*)(\bar{r}^*, t^*) - \bar{\nabla}^* \cdot (P^* \bar{v}^*)(\bar{r}^*, t^*) + (\rho^* \bar{g}^* \cdot \bar{v}^*)(\bar{r}^*, t^*), \end{aligned} \quad (3.16)$$

where  $\otimes$  stands for the tensor multiplication and  $\bar{I}$  is the unit tensor.

Further, assuming the coolant flow mainly in the axial direction (i.e. neglecting radial flow), the time-dependent single-phase enthalpy  $h(z, t)$  can be expressed with a second order polynomial as:

$$h(z, t) \approx h_2(z, t) = h(0, t) + \sum_{i=1}^2 p_i(t) z^i. \quad (3.17)$$

Then, rewriting the energy balance equation in terms of enthalpy, after cross-section averaging, the following dimensionless ODEs can be derived for the corresponding enthalpy time-dependent expansion coefficients  $p_i(t)$  for each of the four heated channels:

$$\frac{dp_{1,l}(t)}{dt} = \frac{6}{\mu_l(t)} [N_\rho N_r N_{pch,1\phi,l}(t) - v_{inlet,l}(t) p_{1,n}(t)] - 2v_{inlet,l}(t) p_{2,l}(t), \quad (3.18)$$

$$\frac{dp_{2,l}(t)}{dt} = -\frac{6}{\mu_l^2(t)} [N_\rho N_r N_{pch,1\phi,l}(t) - v_{inlet,l}(t) p_{1,l}(t)], \quad (3.19)$$

where  $N_r$  and  $N_\rho$  are dimensionless numbers,  $Fr$  is the Froude number and  $N_{pch,1\phi}(t)$  is the so-called time dependent phase change number in the single-phase region which is proportional to the wall heat flux  $q_{1\phi}^{*''}$  and  $\mu(t)$  is the boiling boundary (the axial elevation in the reactor core where boiling starts).

### 3.3.2 Two-phase region

Following the same procedure as in the single-phase region, one starts with the three local conservation equations written for mass, momentum and energy for each coolant phase region, respectively, as [4, 24]:

$$\frac{\partial \rho_k^*(\bar{r}^*, t^*)}{\partial t^*} + \bar{\nabla}^* \cdot (\rho_k^* \bar{v}_k^*)(\bar{r}^*, t^*) = 0, \quad (3.20)$$

$$\begin{aligned} & \frac{\partial (\rho_k^* \bar{v}_k^*)}{\partial t^*}(\bar{r}^*, t^*) + \bar{\nabla}^* \cdot (\rho_k^* \bar{v}_k^* \otimes \bar{v}_k^*)(\bar{r}^*, t^*) \\ &= \bar{\nabla}^* \cdot \bar{\tau}^*(\bar{r}^*, t^*) - \bar{\nabla}^* \cdot (P_k^*(\bar{r}^*, t^*) \bar{I}) + \rho_k^*(\bar{r}^*, t^*) \bar{g}^*, \end{aligned} \quad (3.21)$$

$$\begin{aligned} & \rho^*(\bar{r}^*, t^*) \frac{\partial h^*(\bar{r}^*, t^*)}{\partial t^*} + (\rho^* \bar{v}^*)(\bar{r}^*, t^*) \cdot \bar{\nabla}^* \cdot h^*(\bar{r}^*, t^*) \\ &= -\bar{\nabla}^* \cdot \bar{q}^{*''}(\bar{r}^*, t^*) + q^{*''' }(\bar{r}^*, t^*) + \bar{\tau}^*(\bar{r}^*, t^*) : [\bar{\nabla}^* \otimes \bar{v}^*(\bar{r}^*, t^*)] \frac{\partial P^*(\bar{r}^*, t^*)}{\partial t^*} + \\ & \quad + \bar{v}^*(\bar{r}^*, t^*) \cdot \bar{\nabla}^* P^*(\bar{r}^*, t^*), \end{aligned} \quad (3.22)$$

Here,  $k = l, v$  stands for the coolant phase:  $l$  for the liquid phase and  $v$  for the vapor phase. Further, performing a radial space-averaging on the entire cross-sectional flow area, assuming that both phases are in thermal equilibrium and using a mixture model (homogeneous equilibrium model), replacing the time-dependent flow quality with the following second order polynomial profile:

$$x(z, t) \approx x_2(z, t) = N_\rho N_r (d_1(t)(z - \mu(t)) + d_2(t)(z - \mu(t))^2) \quad (3.23)$$

and implementing the variational method to the resulting equations, after some rearrangements one gets the following dimensionless ODEs for the corresponding quality time-dependent expansion coefficients  $d_i(t)$  for each of the four channels:

$$\frac{dd_{1,l}(t)}{dt} = \frac{1}{f_{2,l}(t)} (f_{3,l}(t)f_{1,l}(t) + f_{4,l}(t)) \quad (3.24)$$

$$\frac{dd_{2,l}(t)}{dt} = \frac{1}{f_{5,l}(t)} (f_{3,l}(t)f_{1,l}(t) + f_{6,l}(t)) \quad (3.25)$$

In the above,  $f_i(t)$ ,  $i = 1, \dots, 6$  are complicated functions of time, depending on the design and operational parameters, as well as phase variables, i.e. inlet velocity  $v_{inlet}(t)$ , pellet temperature time-dependent coefficients  $T_i(t)$ ,  $i = 1, 2$ , phase change number  $N_{pch,2\phi}$ , mixture density  $\rho_m(z, t)$  and boiling boundaries  $\mu(t)$ .

The remaining two equations (3.15) and (3.21), written for the single- and two-phase pressure drops, are used to derive the ODEs for the inlet velocity, using the pressure drop balance and are not given here. We refer instead to [4–7].

## 3.4 ROM modifications

In the following, the major modifications of the present ROM, compared with other existing ROMs developed in the past, are pointed out. These modifications were performed in order to improve the consistency of the ROM with the input data used and to better model the physical behavior of instabilities. The list of the required input parameters for the ROM simulations are given below:

1. the design parameters of the system;
2. the thermal-hydraulic state variables, i.e. saturation temperature, densities, etc.;
3. the operational parameters or conditions, i.e. inlet flow, power, external pressure drop and inlet temperature/enthalpy.

Some of these parameters were extracted from the static core simulator SIMULATE-3 output, providing a detailed description of the BWR core being studied. Others were taken from the technical description of a BWR power plant and water tables.

### 3.4.1 Adjustment of the homogeneous equilibrium model to a higher order model (drift flux model)

From the ROM analysis, it was found that the models currently used, where the homogeneous equilibrium model (HEM) [4,24] is utilized, significantly overestimate the void fraction at the core exit, compared with the one calculated by SIMULATE-3. For comparison, both void fraction profiles are demonstrated in the left plot of Fig. 3.1. From the right plot of Fig. 3.1 where the results of the stability calculations performed with the ROM are shown, one can conclude that the investigated system is very close to an unstable behavior, whereas a stable behavior of the system was proven by system codes where the drift flux model (DFM) [5,6,24] is implemented.

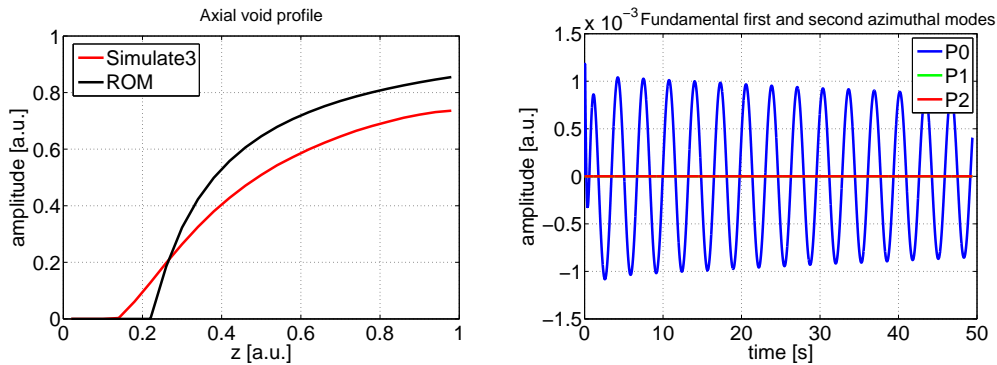


**Figure 3.1:** Axial void profile calculated by SIMULATE-3 (left figure, red line) and by the ROM (left figure, black line) and the corresponding ROM stability analysis (right figure) with the original value of cross-sectional flow area  $A_{actual}^* = 1.3811 \cdot 10^{-4} m^2$ .

To overcome this inconsistency between the HEM and the DFM and not to further complicate the ROM system, the cross-sectional flow area of the heated channel  $A_o^*$  was artificially modified, so that the HEM can reproduce the void profile estimated by higher-order models such as the DFM. The new cross-sectional flow area was estimated by comparing the exit void fraction calculated from the ROM with HEM and the one from SIMULATE-3 with DFM, i.e. the following relationship between the old and the new cross-sectional flow areas was obtained:

$$A_{o,ROMadj}^* = \frac{\frac{1}{1 + \frac{1 - \alpha_{exit,ROM}^* \rho_l^*}{\alpha_{exit,ROM}^* \rho_g^*}} \cdot (h_g^* - h_l^*) - h_{inlet}^* + h_l^*}{\frac{1}{1 + \frac{1 - \alpha_{exit,SIM}^* \rho_l^*}{\alpha_{exit,SIM}^* \rho_g^*}} \cdot (h_g^* - h_l^*) - h_{inlet}^* + h_l^*} \cdot A_{o,SIM}^* \quad (3.26)$$

A more detailed derivation of Eq. (3.26) is given in [25,26]. The axial void profile as calculated from the ROM with adjusted cross-sectional flow area  $A_o^*$  is shown in Fig. 3.2 (left figure). Comparing the ROM stability analysis using the actual cross-sectional flow area  $A_{actual}^*$  [see Fig. 3.1, right figure] with the one performed using the adjusted flow area  $A_o^*$  [see Fig. 3.2, right figure], one can notice that the adjustment of the flow area stabilizes the system due to the reduction of the void fraction at the core outlet.

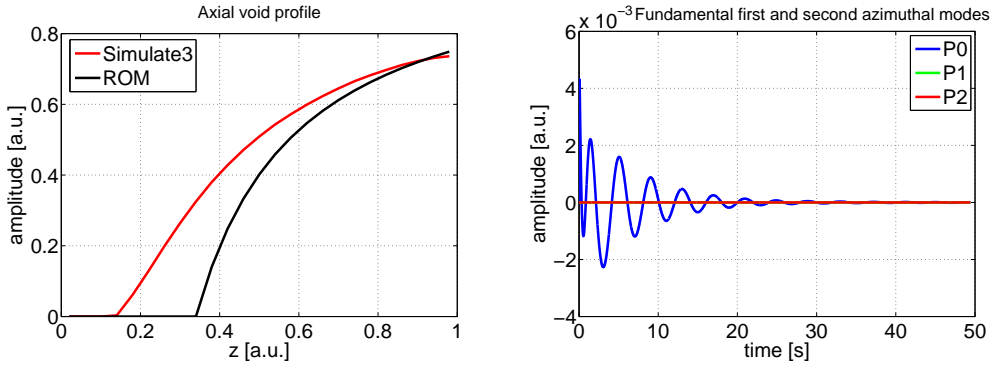


**Figure 3.2:** Axial void profile calculated by SIMULATE-3 (left figure, red line) and by the ROM with uniform power profile (left figure, black line) and result of the corresponding stability analysis (right figure) with the adjusted value of  $A_o^* = 2.049 \cdot 10^{-4} m^2$ .

### 3.4.2 Introduction of a non-uniform power profile

Although the cross-sectional flow area utilized in the ROM was properly adjusted to compensate for the use of the HEM, there is still a significant mismatch observed between the void profile as calculated by the ROM with the corrected  $A_o^*$  and the one calculated in SIMULATE-3. The reason for this mismatch can be explained by the fact that a uniform axial power profile was assumed when calculating the ROM void profile. However, in real commercial BWRs, the axial power profile is always bottom-peaked due to the better moderation properties of the subcooled region. For this reason, a two-step power density representing the separate power production in the single- and two-phase regions was introduced into the ROM. This was achieved by replacing the uniform power density  $c_q^*$  with non-uniform ones  $c_{q,1}^*$  and  $c_{q,2}^*$  for the single- and two-phase regions, respectively, utilizing the realistic axial power profile from the 3D core simulator CORE SIM. The numerical method for estimating  $c_{q,1}^*$  and  $c_{q,2}^*$  is presented in [25,26].

### 3.4.3 Iterative procedure for steady-state calculations

It is worth mentioning that the steady-state solution available from a commercial core simulator together with all necessary input data and parameters for the calculations, cannot be directly used in the ROM since such a steady-state solution will not satisfy the corresponding ROM balance equations, i.e. neutron, heat and flow balance equations. The reason lies with the fact that the ROM equations are fundamentally different from the ones used in core simulators, especially what regards the spatial discretization. Consequently, a steady-state solution consistent with models implemented in the ROM has to be found. For this purpose, an iterative procedure was developed to estimate the

proper steady-state solution. A short description of this procedure is given below.

From the steady-state solution obtained from a commercial core simulator (i.e. SIMULATE-3), the three-dimensional distributions of the macroscopic cross-sections were obtained together with their relative changes due to either void fraction or fuel temperature perturbations. These cross-section distributions were consequently used in CORE SIM to calculate the static flux. Afterwards, using the boiling boundary estimated from the commercial core simulator SIMULATE-3, the CORE SIM solution was used to estimate the power produced in the single- and two-phase regions. Then, the dimensionless heat transfer equations were correspondingly modified in order to account for a non-uniform power profile.

Next, the fuel temperature and flow properties were estimated using the ROM thermal hydraulic model at steady-state. Based on the computed thermal-hydraulic solution, a new set of cross-sections as well as a new boiling boundary were calculated. The process was then repeated until convergence. The results of the iterative procedure for estimating the steady-state axial void profile are given in Fig. 3.3. It can be noticed that the recalculated steady-state profile satisfactorily agrees with the SIMULATE-3 solution.

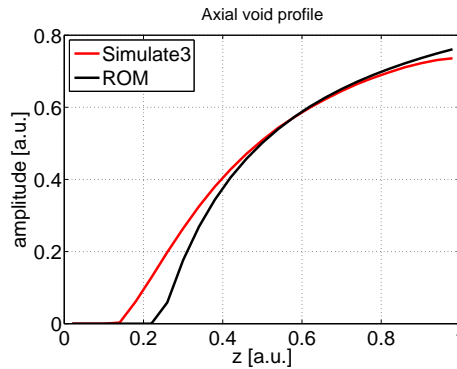


**Figure 3.3:** Axial void profile calculated by SIMULATE-3 (red line) and by the ROM (black line) for the nonuniform power profile after application of the recalculation procedure (update of the cross-sections).

### 3.5 Analysis of the numerical results

In this Section, some of the results of the numerical integration of the resulting 42 ROM ODEs, describing the dynamical behavior of a BWR, are demonstrated. A large number of calculations were made from various artificial operational conditions, out of which only the most interesting ones are shown and discussed below. The term artificial refers to the fact that one of the parameters of the system, namely the cross-sectional flow area  $A_o^*$  was adjusted in such a way that it is possible to simulate different oscillating patterns keeping the other parameters as typical ones for a BWR. The present investigation is mainly focused on the qualitative comparison of the ROM results between different operational points, just to demonstrate the capabilities of the ROM to reconstruct different stability behaviors. Emphasis is put on the coupling between different modes.

Depending on the stability properties of the modes, the following three cases were investigated:

1. both the fundamental and azimuthal modes are stable;
2. the fundamental mode is unstable and the azimuthal modes are stable;
3. both the fundamental and azimuthal modes are unstable (combined instability).

### 3.5.1 Case of a stable system

Here, the case of a completely stable system when all three modes decay relatively fast is considered. The cross-sectional flow area was set to  $A_o^* = 2.249 \cdot 10^{-4} \text{ m}^2$ . For better visibility, the time evolution of the signals for the fundamental, the first and the second azimuthal modes are shown separately in Fig. 3.4. One interesting feature which is observed from these figures is the fact that the amplitude factors of the azimuthal modes are several orders of magnitude smaller compared with the fundamental one. Such a behavior can be explained by the fact that all modes except the fundamental one have eigenvalues much smaller than unity and, hence, bring strongly negative reactivity. For the purpose of comparison, one also shows the time evolution of the inlet velocities in the first and the third channels in Fig. 3.5 which reconstruct the behavior of the corresponding (fundamental) neutronic mode.

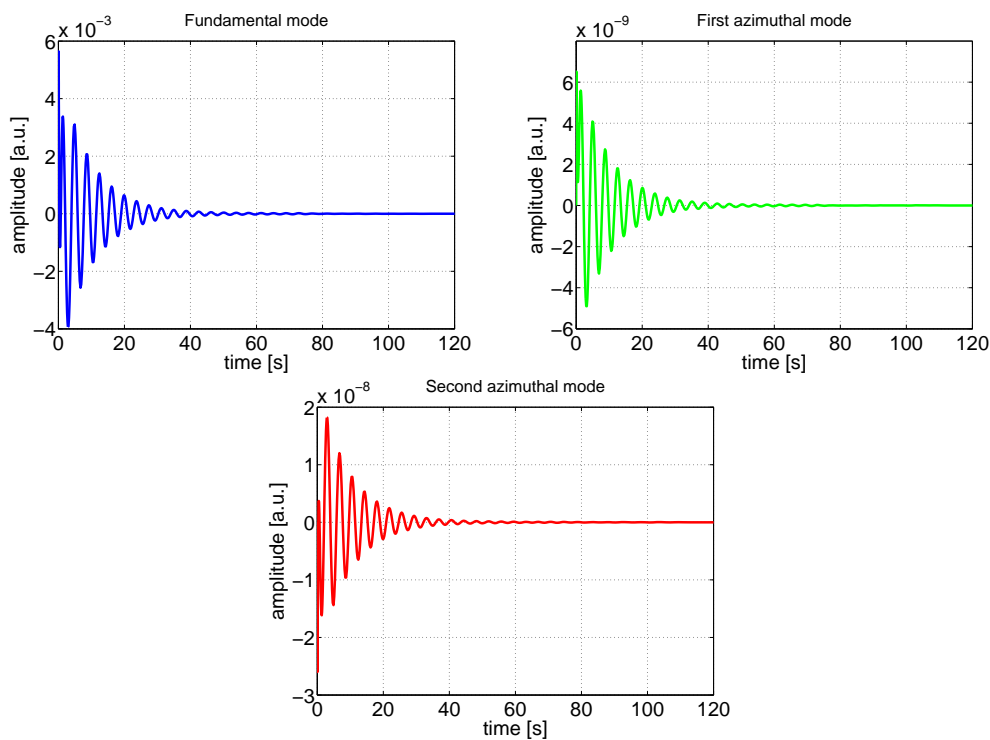


**Figure 3.4:** Time evolutions of the fundamental (upper left figure), the first (upper right) and the second (lower figure) modes for the case of a stable system,  $A_o^* = 2.249 \cdot 10^{-4} \text{ m}^2$ ,  $\delta v_{inlet} = 0.125 \text{ [a.u.]}$ .

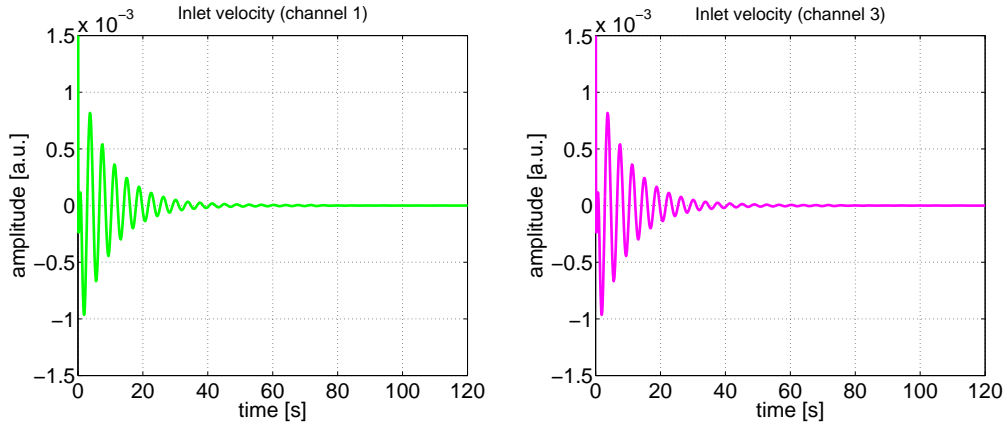


**Figure 3.5:** Time evolutions of the inlet velocities for the first (left figure) and third (right figure), respectively, heated channels for the case of a stable system,  $A_o^* = 2.249 \cdot 10^{-4} m^2$ ,  $\delta v_{inlet} = 0.125 [a.u.]$ .

### 3.5.2 Case of a global instability

Next, one considers the case of a global instability [see Figs. 3.6-3.7] when only the fundamental mode is unstable. The cross-sectional flow area was set to  $A_o^* = 1.8 \cdot 10^{-4} m^2$ . Similarly to the previous case, Fig. 3.6 shows the time evolution of each of the modes separately. The figure clearly indicates the proper excitation of the in-phase oscillations (i.e. the ones corresponding to the fundamental mode). The out-of-phase modes (i.e. the azimuthal modes) also seem to oscillate, however, with amplitudes millions times smaller compared with the amplitude of the fundamental modes. The latter can be interpreted as the result of the coupling between the unstable fundamental mode and the azimuthal modes which are apparently stable. In Fig. 3.7, the time evolution of the corresponding inlet velocities in the first and third heated channels are also shown. It is clear that inlet velocities oscillate in-phase with each other, thus, following the behavior of the fundamental mode.

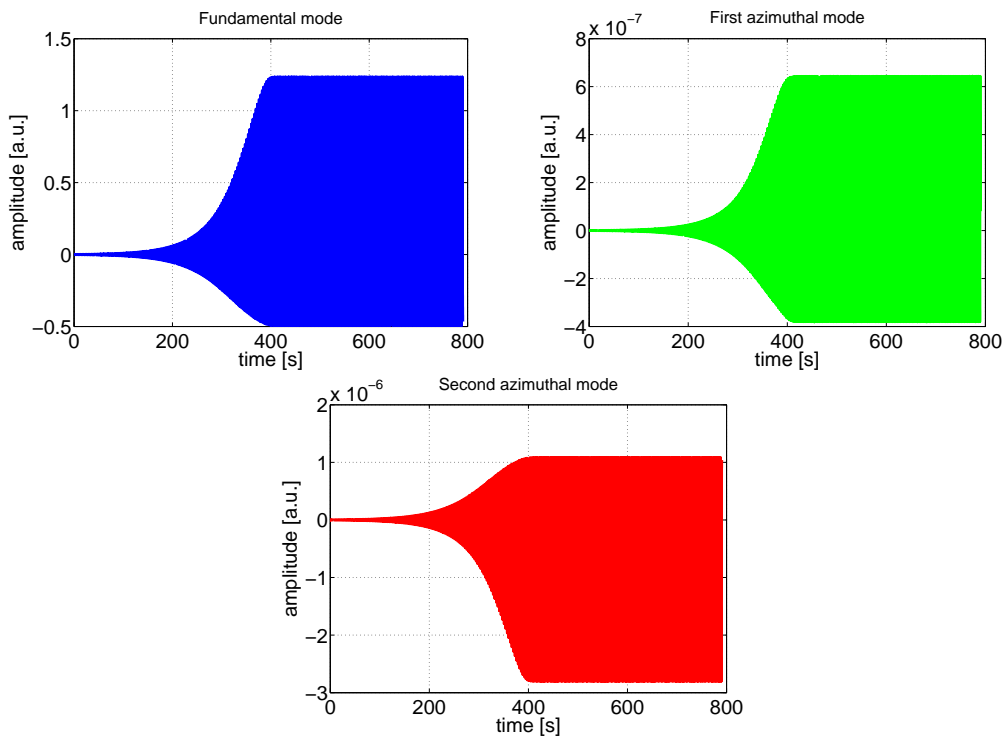


**Figure 3.6:** Time evolutions of the fundamental (upper left figure), the first (upper right figure) and the second (lower right) azimuthal modes for the case of global instability,  $A_o^* = 1.8 \cdot 10^{-4} m^2$ ,  $\delta v_{inlet} = 0.05 [a.u.]$ .

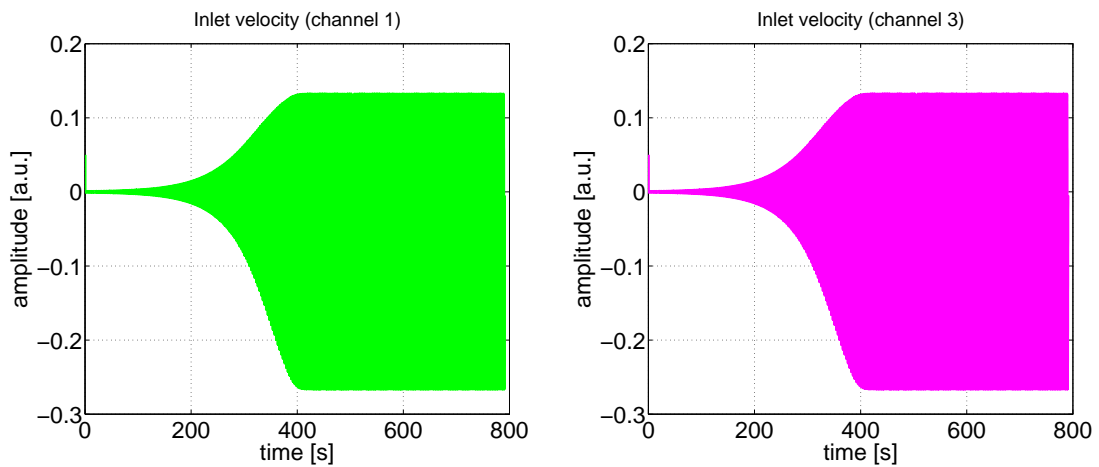


**Figure 3.7:** Time evolutions of the inlet velocities for the first (left figure) and third (right figure), respectively, heated channels for the case of global instability,  $A_o^* = 1.8 \cdot 10^{-4} m^2$ ,  $\delta v_{inlet} = 0.05 [a.u.]$ .

### 3.5.3 Case of a combined instability

Finally, the case of a combined instability, when all three modes are unstable, is discussed. The cross-sectional flow area of the channel was chosen equal to  $A_o^* = 1.8 \cdot 10^{-4} m^2$ . In order to excite both azimuthal modes, several additional modifications of the system parameters were made, namely the criticality of the azimuthal modes was set to zero and some of the reactivity coefficients  $C_{mn}^{*V,D}$  were properly adjusted. Such modifications were required by the fact that the investigated operating point did not exhibit any azimuthal instabilities and, hence, such instabilities should be introduced artificially.

Similarly to the previous two cases, the time evolution of each of the modes is shown in Fig. 3.8. The figure clearly demonstrates the proper excitation of the in-phase and out-of-phase oscillations. The time evolution of the inlet velocities for the corresponding heated channels is also given in Fig. 3.9. From this figure, it can be clearly seen that two (the first and the third channels) out of four heated channels oscillate out-of-phase compared with the other two (the second and the fourth ones), thus representing the time-dependent behavior of the dominant (second) azimuthal mode. Thus, the stability behavior in this particular case is driven by the second azimuthal mode. However, the effect of the other two modes is also significant. The time evolution of the corresponding inlet velocities for each of the four channels can be found in [25,26].

It is interesting to compare the current case with earlier cases reported in the literature. For this purpose, in Fig. 3.10, the time evolution of all three modes for four different cases (A, B, C and D) of mode inclusion is shown. The inclusion of different modes was performed by proper adjustment of the reactivity coefficients  $C_{mn}^{*V,D}$ . From Fig. 3.10 several interesting features can be observed. In the first case (Case A) where the effect of the first azimuthal mode is excluded (upper left plot of Fig. 3.10), the fundamental mode exhibits monotonically oscillating behavior with an amplitude 3 times less than the corresponding second azimuthal mode. On the other hand, in the second case (Case B) where the effect of the second mode is excluded (upper right plot of Fig. 3.10), the behavior of the fundamental mode is not so monotonic, namely it exhibits regular phase jumps of  $180^\circ$  with amplitude 5 times less compared with the first azimuthal mode. Such a peculiar behavior can be clarified by the different values of the  $C_{mn}^{*V,D}$  coefficients corresponding to different modes. From the comparison between these two cases (A and B) and Case C (lower left plot of Fig. 3.10) where both azimuthal modes are excluded, it can also be concluded that the inclusion of the azimuthal modes decreases the amplitude of the fundamental mode almost four times. More details can be found in [25,26].

An even more remarkable case is when both azimuthal modes are included simultaneously as shown in the lower right plot of Fig. 3.10 (Case D). Comparing this case with the first two cases discussed above (Cases A and B), one can notice that in the studied case the amplitude of the first azimuthal mode decreases by increasing the amplitude of the other two modes (the fundamental and the second azimuthal modes). Such interference effects between different modes are of particular importance since they affect the stability characteristics of each of the modes and thus, can lead to an incorrect determination of the stability boundaries if no modal decomposition is applied. Moreover, from this simple analysis one can demonstrate that the inclusion of different azimuthal modes also results in earlier or delayed excitation of the fundamental mode.

To conclude this investigation, another interesting phenomenon, namely the oscillating symmetry line between the first two azimuthal modes, modeled with the present

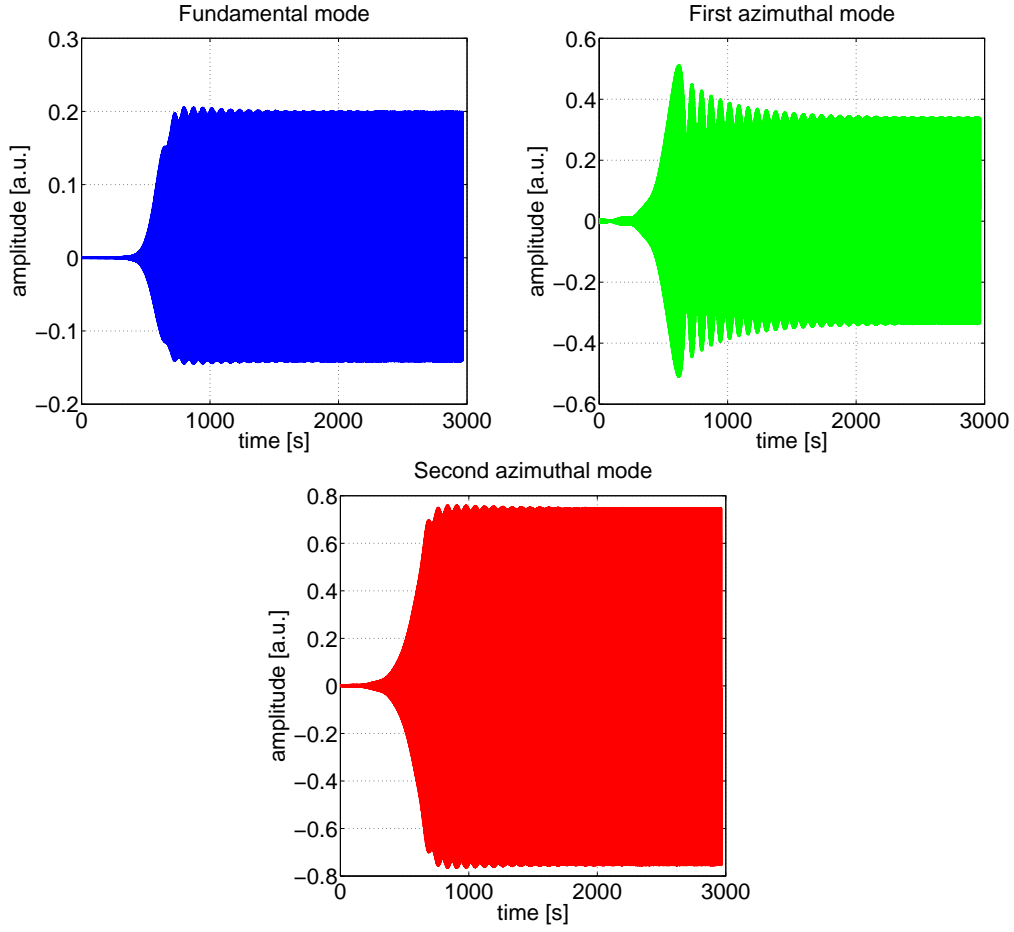


**Figure 3.8:** Time evolutions of the fundamental (upper left figure), the first (upper right figure) and the second (lower figure) azimuthal modes for the case of combined instability,  $\rho_{s1} = \rho_{s2} = 0$ , modified reactivity coefficients  $C_{mn}^{*V,D}$ ,  $A_o^* = 1.8 \cdot 10^{-4} m^2$ ,  $\delta v_{inlet} = 0.1 [a.u.]$ .

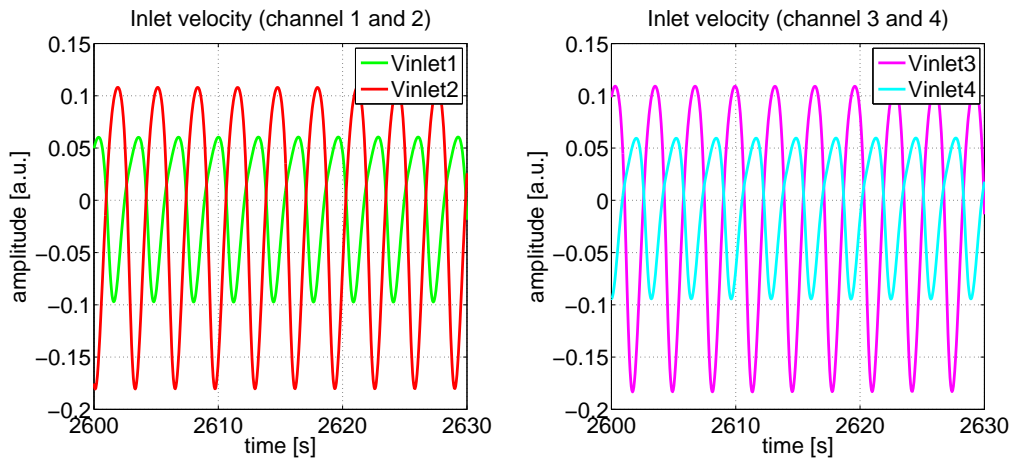


**Figure 3.9:** Time evolutions of the inlet velocities for the first/second (left figure) and third/fourth (right figure), respectively, heated channels for the case of combined instability,  $\rho_{s1} = \rho_{s2} = 0$ , modified reactivity coefficients  $C_{mn}^{*V,D}$ ,  $A_o^* = 1.8 \cdot 10^{-4} m^2$ ,  $\delta v_{inlet} = 0.1 [a.u.]$ .

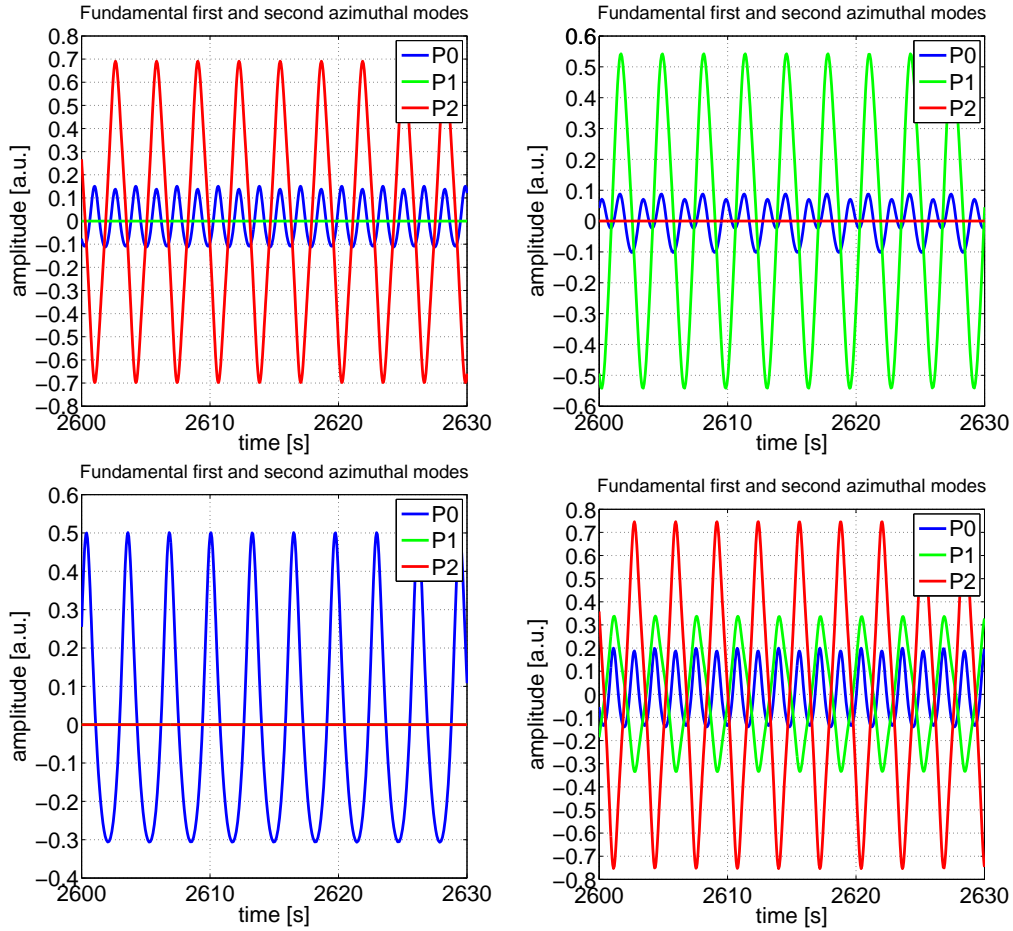


**Figure 3.10:** Time evolutions of the fundamental, the first and the second azimuthal modes for the case of combined instability,  $\rho_{s1} = \rho_{s2} = 0$ , modified reactivity coefficients  $C_{mn}^{*V,D}$ ,  $A_o^* = 1.8 \cdot 10^{-4} \text{ m}^2$ ,  $\delta v_{inlet} = 0.1 \text{ [a.u.]}$ ; case A - upper left figure, case B - upper right figure, case C - lower left figure and case D - lower right figure (the first azimuthal mode is not visible due to its smallness compared with the other two modes).

ROM, is discussed. The oscillating symmetry line has already been observed in some past instability events and several possible explanations of this phenomenon were proposed. Such an oscillating pattern is usually observed when both azimuthal modes are excited and oscillate with close but different frequencies. This difference in the frequencies thus creates a time-dependent phase shift between the modes resulting in the oscillating symmetry line. Intuitively, it is clear that in order to simulate such a behavior, the properties of the heated channels should be different. For this reason, in the ROM, the inlet  $k$ -losses (pressure loss coefficients) were modified resulting in different flow rates in each channel and creating the oscillating pattern. The result of this simulation is given in Fig. 3.11. It should be emphasized that such a time-dependent phase shift between the modes can also lead to an incorrect determination of the stability properties if no modal decomposition is performed.

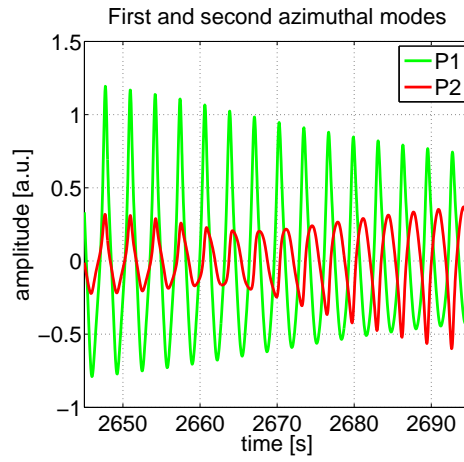


**Figure 3.11:** Time evolutions of the first and the second azimuthal modes for the case of combined instability,  $\rho_{s1} = \rho_{s2} = 0$ , modified inlet pressure loss coefficients  $k_{inlet}$  and reactivity coefficients  $C_{mn}^{*V,D}$ ,  $A_o^* = 1.8 \cdot 10^{-4} \text{ m}^2$ ,  $\delta v_{inlet} = 0.1 \text{ [a.u.]}$ .



# MODELING OF LOCAL INSTABILITIES VIA ROM

A methodology used to model the effect of local instabilities (in particular, the ones caused by density wave oscillations) in reduced order models is described [26,28]. The modified ROM is hereafter applied to analyze a realistic local instability event, i.e. the Forsmark-1 instability event of 1996/1997. A qualitative comparison between the ROM-simulated results and the corresponding power plant stability measurements is performed, out of which some conclusions are drawn.

## 4.1 ROM modifications to account for the effect of local instabilities

Throughout this study, it is assumed that the DWOs are self-sustained and only their effect on the stability properties of the system is investigated. The effect of the core response on the DWOs is thus neglected. Following similar steps as in the case of core-wide instabilities, one starts with the general time- and space-dependent two-group diffusion equations which, after the application of first order perturbation theory (i.e. considering small fluctuations of all quantities around their mean values), can be converted to the following noise equations (i.e. equations for the fluctuating parts):

$$\bar{v}^{*-1} \cdot \frac{\partial \delta \bar{\Psi}^*(\bar{r}^*, t^*)}{\partial t^*} = [(1 - \beta^*) \cdot \delta \bar{F}^*(\bar{r}^*, t^*) - \delta \bar{L}^*(\bar{r}^*, t^*)] \cdot (\bar{\Phi}_0^*(\bar{r}^*) + \delta \bar{\Psi}^*(\bar{r}^*, t^*)) + [(1 - \beta^*) \cdot \bar{F}_0^*(\bar{r}^*, t^*) - \bar{L}_0^*(\bar{r}^*, t^*)] \cdot \delta \bar{\Psi}^*(\bar{r}^*, t^*) + \lambda \cdot \delta C^*(\bar{r}^*, t^*) \cdot \bar{X}, \quad (4.1)$$

$$\frac{\partial \delta C^*(\bar{r}^*, t^*)}{\partial t^*} \cdot \bar{X} = \beta^* \cdot \delta \bar{F}^*(\bar{r}^*, t^*) \cdot (\bar{\Phi}_0^*(\bar{r}^*) + \delta \bar{\Psi}^*(\bar{r}^*, t^*)) + \beta^* \cdot \bar{F}_0^*(\bar{r}^*) \cdot \delta \bar{\Psi}^*(\bar{r}^*, t^*) - \lambda \cdot \delta C^*(\bar{r}^*, t^*) \cdot \bar{X}. \quad (4.2)$$

Eqs. (4.1)-(4.2) describe the system response to any type of perturbations including both the ones induced by core-wide and the ones induced by local perturbations. However, one can study the effect of each perturbation separately using a similar approach in each case. That can be achieved by introducing the corresponding noise sources into the cross-section operators  $\delta \bar{F}^*$  and  $\delta \bar{L}^*$ , i.e.

$$\delta \bar{X} S^*(\bar{r}^*, t^*) = \delta \bar{X} S^{*h}(\bar{r}^*, t^*) + \delta \bar{X} S^{*i}(\bar{r}^*, t^*), \quad (4.3)$$

which give rise to the corresponding fluctuations in the neutron fluxes written as:

$$\bar{\delta}\Psi^*(\bar{r}^*, t^*) = \bar{\delta}\Psi^{*h}(\bar{r}^*, t^*) + \bar{\delta}\Psi^{*i}(\bar{r}^*, t^*), \quad (4.4)$$

$$\delta C^*(\bar{r}^*, t^*) = \delta C^{*h}(\bar{r}^*, t^*) + \delta C^{*i}(\bar{r}^*, t^*), \quad (4.5)$$

where  $i$  stands for inhomogeneous (i.e. local oscillations) and  $h$  for homogeneous (core-wide oscillations). The solution to this kind of problem can be found by first determining the response of the core to a pure local oscillations  $\bar{\delta}\Psi^{*i}(\bar{r}^*, t^*)$ , i.e. solving the inhomogeneous problem (derived from Eqs. (4.1)-(4.2)) defined as:

$$\begin{aligned} \bar{v}^{*-1} \cdot \frac{\partial \bar{\delta}\Psi^{*i}(\bar{r}^*, t^*)}{\partial t^*} &= [(1 - \beta^*) \cdot \bar{\delta}\bar{F}^{*i}(\bar{r}^*, t^*) - \bar{\delta}\bar{L}^{*i}(\bar{r}^*, t^*)] \cdot \bar{\Phi}_0^*(\bar{r}^*) \\ &+ [(1 - \beta^*) \cdot \bar{F}_0^*(\bar{r}^*, t^*) - \bar{L}_0^*(\bar{r}^*, t^*)] \cdot \bar{\delta}\Psi^{*i}(\bar{r}^*, t^*) + \lambda^* \cdot \delta C^{*i}(\bar{r}^*, t^*) \cdot \bar{X}, \end{aligned} \quad (4.6)$$

$$\begin{aligned} \frac{\partial \delta C^{*i}(\bar{r}^*, t^*)}{\partial t^*} \cdot \bar{X} &= \beta^* \cdot \bar{\delta}\bar{F}^{*i}(\bar{r}^*, t^*) \cdot (\bar{\Phi}_0^*(\bar{r}^*) + \bar{\delta}\Psi^{*i}(\bar{r}^*, t^*)) + \beta^* \cdot \bar{F}_0^*(\bar{r}^*) \cdot \bar{\delta}\Psi^{*i}(\bar{r}^*, t^*) \\ &- \lambda^* \cdot \delta C^{*i}(\bar{r}^*, t^*) \cdot \bar{X}, \end{aligned} \quad (4.7)$$

where the second order terms were left out. The general solution of Eqs. (4.6)-(4.7) can be found by assuming delta-function (localized) perturbations in the cross-sections and, thus reads as:

$$\bar{\delta}\Psi^{*i}(\bar{r}^*, t^*) = \bar{B}^* \cdot \exp^{i\omega^* t^*} \cdot \bar{\psi}^{*i}(\bar{r}^*, \bar{r}_0^*, \omega^*), \quad (4.8)$$

$$\delta C^{*i}(\bar{r}^*, t^*) \cdot \bar{X} = \bar{C}^* \cdot \exp^{i\omega^* t^*} \cdot \bar{\psi}^{*i}(\bar{r}^*, \bar{r}_0^*, \omega^*), \quad (4.9)$$

where  $\bar{r}_0^*$  stands for the location of the local perturbation in the cross-sections, and  $\bar{A}^*$ ,  $\bar{B}^*$  and  $\bar{C}^*$  are matrix coefficients. Combining Eqs. (4.8)-(4.9) with Eqs. (4.6)-(4.7), one gets the explicit solutions for the neutron flux  $\bar{\delta}\Psi^{*i}(\bar{r}^*, t^*)$  and the concentration of the delayed neutron precursors  $\delta C^{*i}(\bar{r}^*, t^*)$  of the inhomogeneous problem (4.6)-(4.7).

Next, subtracting Eqs. (4.6)-(4.7) with known solutions (4.8)-(4.9) from the generic equations (4.1)-(4.2) and neglecting small terms, one obtains the equation for the homogeneous problem  $\bar{\delta}\Psi^{*h}(\bar{r}^*, t^*)$  given as:

$$\begin{aligned} \bar{v}^{*-1} \cdot \frac{\partial \bar{\delta}\Psi^{*h}(\bar{r}^*, t^*)}{\partial t^*} &= [(1 - \beta^*) \cdot \bar{\delta}\bar{F}^{*h}(\bar{r}^*, t^*) - \bar{\delta}\bar{L}^{*h}(\bar{r}^*, t^*)] \cdot (\bar{\Phi}_0^*(\bar{r}^*) + \bar{\delta}\Psi^{*h}(\bar{r}^*, t^*)) \\ &+ [(1 - \beta^*) \cdot \bar{F}_0^*(\bar{r}^*, t^*) - \bar{L}_0^*(\bar{r}^*, t^*)] \cdot \bar{\delta}\Psi^{*h}(\bar{r}^*, t^*) + \lambda^* \cdot \delta C^{*h}(\bar{r}^*, t^*) \cdot \bar{X}, \end{aligned} \quad (4.10)$$

$$\begin{aligned} \frac{\partial \delta C^{*h}(\bar{r}^*, t^*)}{\partial t^*} \cdot \bar{X} &= \beta^* \cdot \bar{\delta}\bar{F}^{*h}(\bar{r}^*, t^*) \cdot (\bar{\Phi}_0^*(\bar{r}^*) + \bar{\delta}\Psi^{*h}(\bar{r}^*, t^*)) \\ &+ \beta^* \cdot \bar{F}_0^*(\bar{r}^*) \cdot \bar{\delta}\Psi^{*h}(\bar{r}^*, t^*) - \lambda^* \cdot \delta C^{*h}(\bar{r}^*, t^*) \cdot \bar{X}, \end{aligned} \quad (4.11)$$

where  $\bar{\delta}\Psi^{*h}(\bar{r}^*, t^*)$  and  $\delta C^{*h}(\bar{r}^*, t^*)$  are defined as:

$$\bar{\delta}\Psi^{*h}(\bar{r}^*, t^*) = (\bar{\delta}\Psi^* - \bar{\delta}\Psi^{*i})(\bar{r}^*, t^*),$$

$$\delta C^{*h}(\bar{r}^*, t^*) = (\delta C^* - \delta C^{*i})(\bar{r}^*, t^*).$$

The solution of Eqs. (4.11)-(4.12) can be found by applying traditional mode expansion, similarly to the one used in earlier calculations. Thus, taking only the first three eigenmodes of the flux expansion into account, the full solution to Eqs. (4.1)-(4.2) is given as:

$$\delta\bar{\Psi}^*(\bar{r}^*, t^*) = \sum_{n=0}^2 \bar{P}_n^*(t^*) \cdot \bar{\Phi}_n^*(\bar{r}^*) + \sum_{k=1}^{N_s} \bar{B}_k^* \cdot \exp^{i\omega_k^* t^*} \cdot \bar{\psi}_k^*(\bar{r}^*, \bar{r}_0^*, \omega_k^*), \quad (4.12)$$

where  $\bar{\Phi}_n^*(\bar{r}^*)$  is the solution of the corresponding eigenvalue problem,  $k$  stands for an index representing any local source and  $N_s$  is the total number of such local sources in the investigated problem.

It is interesting to point out that, from a mathematical point-of-view, Eqs. (4.10)-(4.11) look exactly the same as the ones solved for the case of pure homogeneous (core-wide) perturbations (see Section 3.1) since there is no explicit presence of the local sources in the equations. On the other hand, from a physical point-of-view, the effect of local perturbations is taken into account implicitly via the feedback term  $[(1 - \beta^*) \cdot \delta\bar{F}^{*h}(\bar{r}^*, t^*) - \delta\bar{L}^{*h}(\bar{r}^*, t^*)] \cdot \delta\bar{\Psi}^{*h}(\bar{r}^*, t^*)$  where the effect of both the core-wide and local sources is included.

In addition, from Eq. (4.12), one can also conclude that the presence of the local sources simply leads to some extra heating terms in the power oscillations due to the change of the cross-sections resulting from the neutron noise induced by a DWO.

To sum it up, since the power oscillations strongly influence the fuel temperature, one only needs to modify the heat transfer equations to correctly simulate the effect of local perturbations in the ROM compared with the case of core-wide instabilities. The remaining of the ROM can be kept unchanged. The corresponding changes in the fuel temperature and of the resulting void production will induce perturbations in cross-sections, expressed as  $\delta\bar{F}^{*h}$  and  $\delta\bar{L}^{*h}$ , thus creating an additional thermal-hydraulic feedback effect in the neutron-kinetic model. Thus, the modified heat transfer equations with the effect of local instabilities included, read as:

$$\begin{aligned} \frac{dT_{1,l,j\phi}(t)}{dt} &= p_{11,j\phi} T_{1,l,j\phi}(t) + p_{21,j\phi} T_{2,l,j\phi}(t) \\ &+ p_{31,j\phi} [c_q(P_{0,j}(t) - \tilde{P}_{0,j}) + c_q \xi_1 P_{1,j}(t) + c_q \xi_2 P_{2,j}(t) + c_q \sum_{k=1}^{N_s} \gamma_{k,l} \sin(\omega_k t + \varphi_{k,l})], \end{aligned} \quad (4.13)$$

$$\begin{aligned} \frac{dT_{2,l,j\phi}(t)}{dt} &= p_{12,j\phi} T_{1,l,j\phi}(t) + p_{22,j\phi} T_{2,l,j\phi}(t) \\ &+ p_{32,j\phi} [c_q(P_{0,j}(t) - \tilde{P}_{0,j}) + c_q \xi_1 P_{1,j}(t) + c_q \xi_2 P_{2,j}(t) + c_q \sum_{k=1}^{N_s} \gamma_{k,l} \sin(\omega_k t + \varphi_{k,l})], \end{aligned} \quad (4.14)$$

where  $l = 1..4$ ,  $j = 1, 2$ ,  $P_{0,j}$ ,  $P_{1,j}$ , and  $P_{2,j}$  take a non-uniform axial power profile into account, and  $\gamma_{k,l}$  is defined as:

$$\gamma_{k,l} = \frac{\int_{V_l^*} \bar{F}_0^*(\bar{r}^*) \bar{\psi}_k^*(\bar{r}^*, \bar{r}_0^*, \omega_k^*) d\bar{r}^*}{\int_{V_{core}^*} \bar{F}_0^*(\bar{r}^*) \bar{\Phi}_0^*(\bar{r}^*) d\bar{r}^*}. \quad (4.15)$$

## 4.2 Analysis of the measurements

In this Section, the neutron flux measurements taken during the stability tests to study the Forsmark-1 local instability event of 1996/1997, are investigated [2, 29, 30]. First, a brief introduction into the instability event itself is given.

The event took place in 1996 when start-up tests were carried out at the Swedish BWR Forsmark-1 for the fuel cycle 16. During these tests, some unstable operational conditions at reduced power and reduced flow, were detected. Later on, in January 1997, new stability measurements were performed, in order to investigate the instability event. In one of them, when the reactor was operated at 63.3 % of power and at a core flow of 4298 kg/s, the same instability pattern was again observed with an oscillation frequency around 0.5 Hz. The appearance of this instability was somewhat surprising since all earlier stability calculations indicated a completely stable core [2, 29, 30].

During these stability measurements, the lower axial plane of the core was well equipped with LPRMs, placed at 36 different radial positions on 2 axial levels. The signals from only 27 were recorded at a sampling frequency of 12.5 Hz. As an illustration of these measurement tests, one of the signals, pass-band filtered between 0.4-0.6 Hz and corresponding to the strongest detector response, is shown in Fig. 4.1.

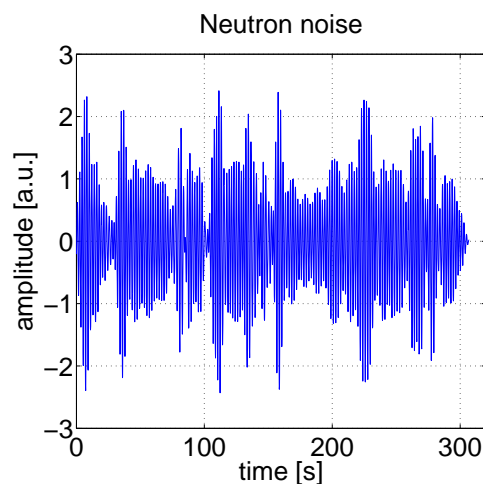


**Figure 4.1:** Time evolution of the filtered neutron noise, measured by LPRM7.

After a spectral analysis of the measurements, several even more interesting features were discovered. The first one is related to the space-dependence of the decay ratio, namely one half of the core oscillated with  $DR=0.6$  whereas the other half with  $DR=0.9$  [2, 29, 30]. However, in all previous studies, the DR was always assumed to be a global stability indicator and, hence, space-independent. Another interesting feature is the rotating symmetry line between the first two azimuthal modes which was observed as a result of the modal decomposition of the corresponding measurements. The time evolution of the first three modes after the decomposition, namely the fundamental, the first and the second azimuthal modes, is given in Fig. 4.2. For the purpose of comparison, both azimuthal modes are shown in the same plot. As one can see from these figures, both global and regional instabilities corresponding to the fundamental and the first two azimuthal modes, respectively, are present. An even more remarkable feature

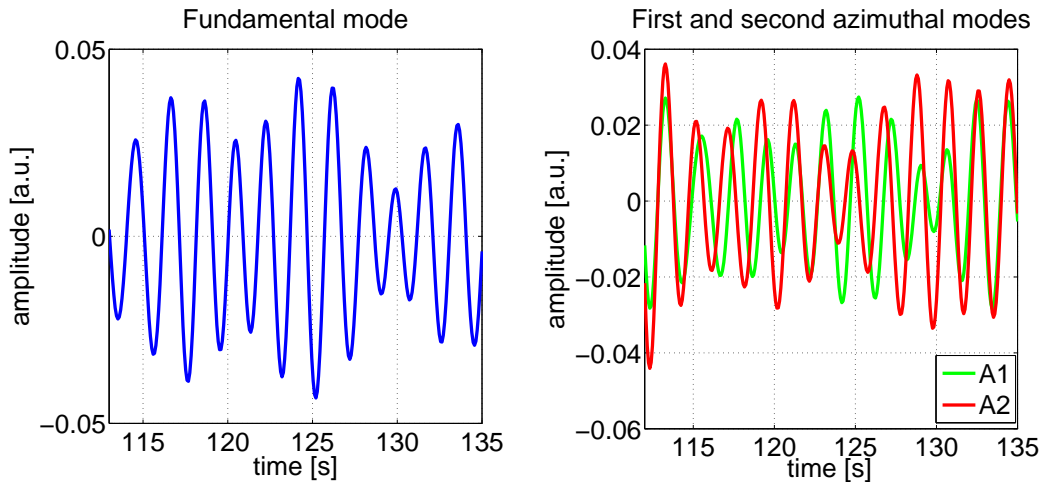


**Figure 4.2:** Time evolution of the fundamental, first and second azimuthal modes after modal decomposition of the measurement data.

which can be clearly seen from the right of Fig. 4.2, is the changing phase shift between the azimuthal modes, resulting in a rotating symmetry line of the regional oscillations.

Further studies of the measurements indicated that the instability was driven by most likely two or even more local noise sources. Later on, it was suggested that these local noise sources are presumably caused by unseated fuel assemblies leading to density wave oscillations and, hence, to local power oscillations.

### 4.3 ROM simulation of the local instabilities

In the following, the results of the simulation of the Forsmark-1 channel instability event using the extended ROM are presented. The time-dependent amplitude factors for each of the three modes were calculated by numerical integration of 42 ROM ODEs.

First, the case without the introduction of any DWO, i.e. the case when only core-wide instabilities may occur, is considered. The corresponding results are given in Fig. 4.3. As this figure shows, for this specific case, the ROM predicts a stable core, both with respect to in-phase and out-of-phase oscillations, and no oscillating symmetry line is observed. This simulation perfectly agrees with earlier stability calculations performed by the utility according to which the core was proven to be stable.

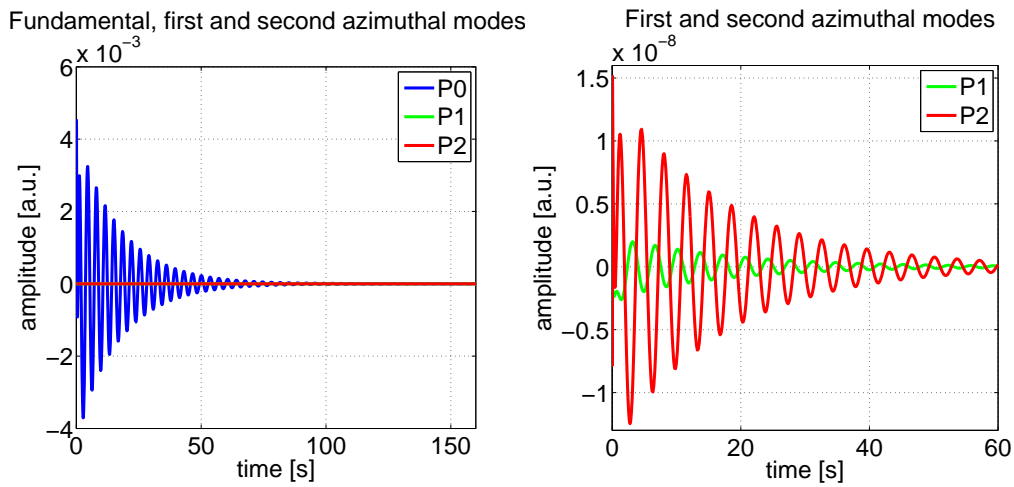


**Figure 4.3:** Time evolutions of the fundamental, the first, and the second azimuthal modes, as computed by the ROM,  $\delta V_{inlet} = 0.1[a.u.]$ .

Next, the case when three local sources were introduced into the ROM is discussed. Some results of this simulation are shown in Fig. 4.4. The dynamical characteristics of the corresponding sources together with their spatial distributions and locations in the core are given in [26,28].

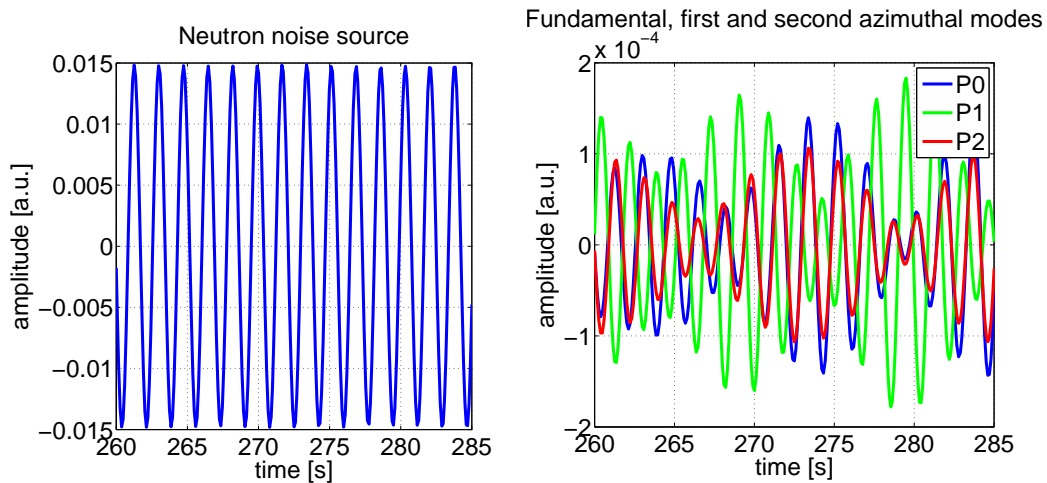


**Figure 4.4:** Time evolutions of the neutron noise source (left figure) and of the induced neutron noise decomposed into the fundamental, the first, and the second azimuthal modes (right figure), as computed by the ROM.

In Fig. 4.4, the time-dependence of the strongest local noise source is given, as well as the decomposition of the corresponding induced neutron noise into the fundamental, the first and the second azimuthal modes. It is worth to point out that all three modes are oscillating with a DR of unity. This is explained by the fact that all modes are driven by

the external local sources.

For the purpose of comparison, in Fig. 4.5, the time evolution of the first three modes, obtained as a result of the modal decomposition of the real measurements, together with the strongest neutron noise, is given. From Figs. 4.4-4.5, it can be clearly seen that both

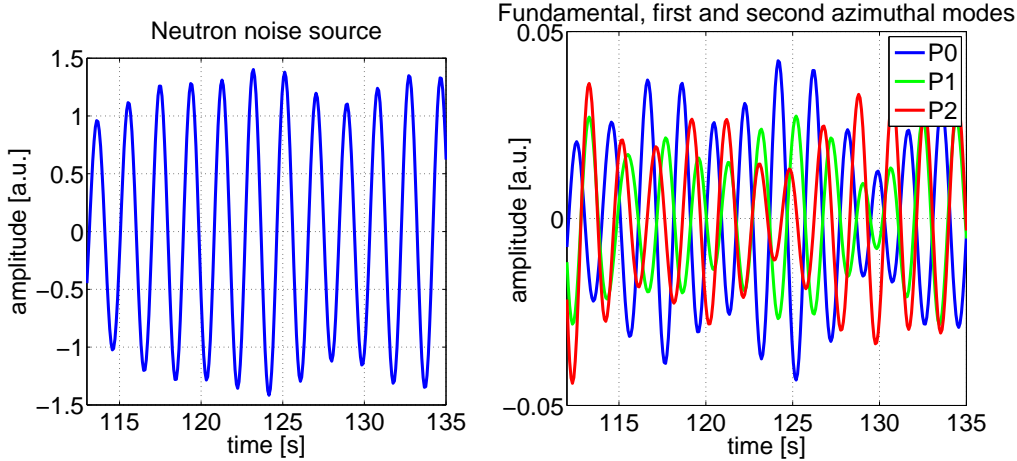


**Figure 4.5:** Time evolutions of the neutron noise source (left figure) and of the induced neutron noise decomposed into the fundamental, the first, and the second azimuthal modes (right figure), as determined from the measurements.

cases exhibit qualitatively a similar behavior. Namely, all modes are properly excited and oscillate with comparable amplitudes. Furthermore, the mode amplitudes have approximately the same ratio, compared with the respective strongest source. Another interesting feature which can be seen in both the ROM simulation and the measurements is the oscillating symmetry line. For better visibility, both azimuthal modes as calculated from the ROM are shown separately in Fig. 4.6.

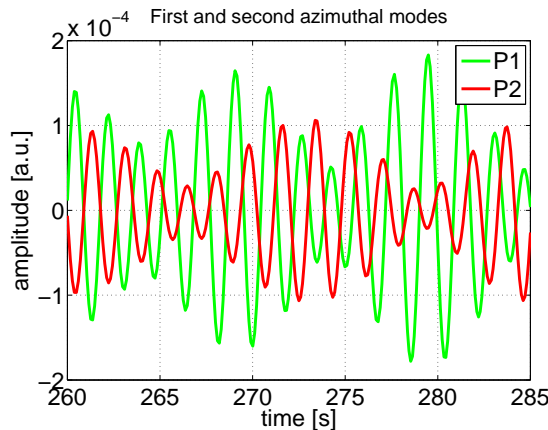


**Figure 4.6:** Time evolution of the first and the second azimuthal modes, as computed by the ROM.

In order to better understand this instability event, it is also instructive to perform two additional ROM simulations which are presented in Fig. 4.7. In this figure, the system response neglecting any possible DWO (lower figure) and the neutron noise induced by

the local sources alone (i.e. the system response is excluded) (upper figure) are given. In both cases, the decomposition into the first three modes is represented. It is clearly seen that the effect of the system dynamics (i.e. pure system response) onto the total neutron noise is quite negligible. This can be explained by the fact that the core-wide modes are, alone, stable, as confirmed both by the stability calculations performed by the utility and the ROM analysis. The latter means that the apparent excitation of the global and regional oscillation modes is due to the inability of a modal decomposition of fully representing the spatial dependence of the neutron noise induced by extremely-localized phenomena, such as DWOs. One can thus conclude that the full system response is mainly driven by the local power oscillations induced by the DWOs, and that the contribution of the system dynamics in terms of global and regional oscillations is negligible, since such modes are inherently stable. Similar conclusions can be drawn from the comparison between Fig. 4.6 and the upper figure of Fig. 4.7 where the amplitudes of the first and second azimuthal modes are given for the case when both contributions from the system and the local sources are included and for the case when only local sources are taken into account (i.e. the system response being excluded), respectively. Obviously, in both cases the signals are almost identical, which supports the earlier conclusions.

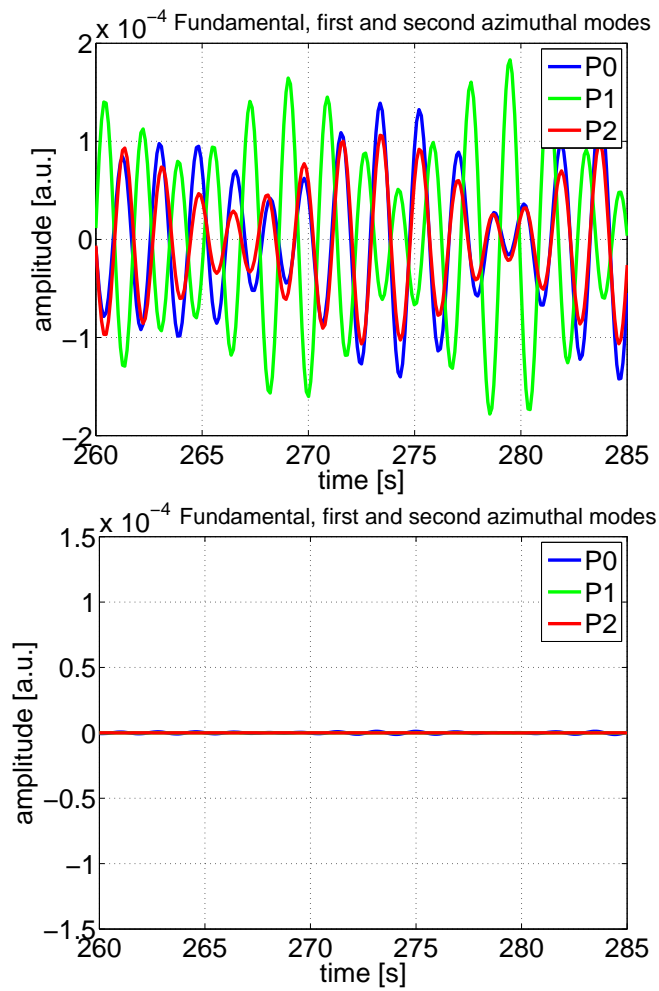


**Figure 4.7:** Time evolutions of the induced neutron noise (without any contribution from the system response, upper figure) and of the corresponding system response (effect of the local sources excluded, lower figure), decomposed into the fundamental, the first, and the second azimuthal modes, as computed by the ROM.



# INVESTIGATION OF BWR STABILITY INDICATORS OTHER THAN THE DECAY RATIO

A careful examination of the balance equations in the ROM developed in this project demonstrates that the behavior of the system is entirely defined by the  $C_{mn}$  coefficients, if one does not consider the case of a pure DWO, which is a thermal-hydraulic instability not directly coupled to the neutronic properties of a given core. As a matter of fact, different core designs lead to different values of the  $C_{mn}$  coefficients, which are the essential parameters appearing in the ROM ODEs. It is thus intuitive to believe that these coefficients could give an indication of the stability of a given system. This Chapter investigates this possibility. First, a qualitative analysis is performed, i.e. the  $C_{mn}$  coefficients are varied and time-dependent simulations, both using the ROM and SIMULATE-3K are carried out to determine whether the system is stable or unstable. Thereafter, a more quantitative analysis is conducted by again varying the  $C_{mn}$  coefficients and estimating the DR from the time-signatures provided by the ROM only.

## 5.1 Qualitative analysis of the stability properties as a function of $C_{mn}$ coefficients.

In this section, a qualitative analysis of the stability property of a system as a function of the corresponding behavior of the void reactivity (i.e.  $C_{mn}$ ) coefficients is presented. For this purpose, series of calculations of the  $C_{mn}$  coefficients for different stability conditions were performed and analyzed. In order to simulate different conditions for the ROM analysis, one of the cross-sections was artificially perturbed. The perturbation was varying between  $-10\%$  to  $+10\%$  with respect to the nominal (reference) value. The study was done for all types of cross-sections as well as for the simultaneous perturbation of all cross-sections. However, the results for only two of the most interesting cases are discussed below. Here, it should be pointed out that such an analysis is more qualitative than quantitative. In order to provide more accurate results from a quantitative point-of-view, the calculations should be performed for each operational condition separately, i.e. by recalculating the steady-state cross-sections each time. Further, for each case studied, the  $C_{mn}$  coefficients should be estimated following the same methodology as was earlier

described.

The results for perturbations of the thermal absorption-cross section are given in Table 5.1. In order to reduce the number of analyzed data, the investigation was made for a homogeneous core, i.e. all cross-sections were homogenized throughout the entire core. Then, using these cross-sections, the corresponding flux was estimated from CORE SIM, and the corresponding  $C_{mn}$  coefficients for all three modes of interest were calculated. As a result, the  $C_{mn}$  coefficients will have the same absolute value for all four channels and, therefore, the  $C_{mn}$  coefficients for only one heated channel are shown in Table 5.1. Then, the corresponding stability properties of the system for various cases were analyzed using the unmodified ROM (i.e. without any update of the steady-state cross-section data). For the analysis, it was assumed that the system is stable if its  $DR$  is less than unity (such a case is designated with the latter "S", i.e. "stable", in the tables). Otherwise, i.e. if the  $DR$  is higher than unity, the system was considered to be unstable (such a case is designated with the latter "U", i.e. "unstable", in the tables). The determination of the  $DR$  being larger or smaller than unity was performed in a qualitative manner, by simply observing whether the oscillations were growing or decreasing, respectively, in amplitude. The cases referred to as "-" in the tables correspond to cases where the ROM was unable to perform the numerical integration of the equations. As one can see from Table 5.1, there is a strong correlation between the stability properties of the system and the behavior of  $C_{mn}$  coefficients, namely for deeply subcritical systems (i.e. for values of  $C_{mn}$  smaller than  $-1$ ), the system becomes unstable whereas for  $C_{mn}$  values between  $-1$  and  $0$  the system is stable. A third behavior can be observed when the numerical integration of the equations is impossible. This is due to a fast divergence resulting from a physically unstable system, since the  $C_{mn}$  coefficients are then positive, corresponding to a void reactivity feedback being positive.

**Table 5.1:** Correlation between the void reactivity coefficients and the stability behavior of the system (from the ROM analysis, homogeneous core).

$\delta\Sigma_{A2}\%$	$P_0$	$P_{1,2}$	$C_{11}$	$C_{12}$	$C_{13}$	$C_{21}$	$C_{22}$	$C_{23}$	$C_{31}$	$C_{32}$	$C_{33}$
-10	-	-	1.93	1.53	1.55	2.10	2.22	1.71	1.57	1.05	1.91
-5	-	-	0.96	0.76	0.77	1.04	1.10	0.84	0.78	0.52	0.94
-1	-	-	0.17	0.14	0.14	0.19	0.20	0.15	0.14	0.09	0.17
-0.1	S	S	-0.003	-0.002	-0.002	-0.005	-0.005	-0.004	-0.004	-0.002	-0.004
-0.05	S	S	-0.012	-0.010	-0.010	-0.015	-0.016	-0.012	-0.011	-0.008	-0.014
0	S	S	-0.022	-0.018	-0.018	-0.026	-0.027	-0.021	-0.019	-0.013	-0.24
0.05	S	S	-0.032	-0.025	-0.026	-0.037	-0.039	-0.029	-0.027	-0.018	-0.033
0.1	S	S	-0.042	-0.033	-0.033	-0.047	-0.050	-0.038	-0.035	-0.024	0.043
1	S	S	-0.22	-0.17	-0.18	-0.23	-0.25	-0.19	-0.18	-0.12	-0.22
5	S	S	-1.00	-0.79	-0.80	-1.09	-1.15	-0.89	-0.82	-0.55	-1.00
7	U	U	-1.39	-1.103	-1.12	-1.52	-1.60	-1.23	-1.13	-0.75	-1.38
10	U	U	-1.98	-1.57	-1.59	-2.16	-2.27	-1.75	-1.61	-1.08	-1.96

A similar analysis but for the case when only the removal cross-section was perturbed is given in Table 5.2. As can be seen from this table, the behavior of the  $C_{mn}$  coefficients has the same tendency as in the previous case. It is worth to mention that the simultaneous perturbation of all cross-sections will probably bring the same result, however the amplitude of the perturbation can be different.

### 5.1. Qualitative analysis of the stability properties as a function of $C_{mn}$ coefficients.

**Table 5.2:** Correlation between the void reactivity coefficients and the stability behavior of the system (from the ROM analysis, homogeneous core).

$\delta\Sigma_R\%$	$P_0$	$P_{1,2}$	$C_{11}$	$C_{12}$	$C_{13}$	$C_{21}$	$C_{22}$	$C_{23}$	$C_{31}$	$C_{32}$	$C_{33}$
-15	<i>U</i>	<i>U</i>	-1.50	-1.19	-1.20	-1.73	-1.83	-1.41	-1.30	-0.87	-1.57
-13	<i>U</i>	<i>U</i>	-1.30	-1.03	-1.05	-1.51	-1.59	-1.22	-1.13	-0.75	-1.36
-10	<i>S</i>	<i>S</i>	-1.00	-0.80	-0.80	-1.17	-1.23	-0.95	-0.87	-0.58	-1.06
-5	<i>S</i>	<i>S</i>	-0.52	-0.41	-0.41	-0.60	-0.63	-0.48	-0.45	-0.30	-0.54
-1	<i>S</i>	<i>S</i>	-0.12	-0.10	-0.10	-0.14	-0.15	-0.1	-0.11	-0.07	-0.13
-0.1	<i>S</i>	<i>S</i>	-0.032	-0.025	-0.026	-0.037	-0.039	-0.030	-0.028	-0.019	-0.034
-0.05	<i>S</i>	<i>S</i>	-0.027	-0.021	-0.022	-0.032	-0.033	-0.026	-0.024	-0.016	-0.029
0	<i>S</i>	<i>S</i>	-0.022	-0.018	-0.018	-0.026	-0.027	-0.021	-0.019	-0.013	-0.24
0.05	<i>S</i>	<i>S</i>	-0.017	-0.014	-0.014	-0.020	-0.021	-0.017	-0.015	-0.010	-0.018
0.1	<i>S</i>	<i>S</i>	-0.012	-0.010	-0.010	-0.015	-0.015	-0.012	-0.011	-0.007	0.013
0.5	–	–	0.027	0.021	0.022	0.031	0.033	0.025	0.023	0.015	0.028
1	–	–	0.076	0.060	0.061	0.088	0.093	0.071	0.066	0.044	0.08
5	–	–	0.47	0.37	0.38	0.54	0.57	0.44	0.41	0.27	0.49
10	–	–	0.96	0.76	0.77	1.11	1.17	0.90	0.83	0.56	1.01

Similar calculations were also performed using the SIMULATE-3/3K package where the  $C_{mn}$  coefficients were estimated together with the DR for a number of different cases and where the thermal absorption cross-section was modified by changing the position of the control rods. The results are summarized in Table 5.3. As seen from this Table, the behavior of the stability properties of the system as a function of the  $C_{mn}$  coefficients is very similar to the one obtained by the ROM analysis, i.e the system is stable for  $-1 < C_{mn} < 0$ , otherwise it is unstable.

**Table 5.3:** Correlation between the reactivity coefficients and the stability behavior of the system (from SIMULATE-3/3K, homogeneous core).

$P_0$	$P_{1,2}$	$C_{11}$	$C_{12}$	$C_{13}$	$C_{21}$	$C_{22}$	$C_{23}$	$C_{31}$	$C_{32}$	$C_{33}$
<i>S</i>	<i>S</i>	-0.089	-0.070	-0.70	-0.079	-0.089	-0.057	-0.79	-0.057	-0.089
<i>S</i>	<i>S</i>	-0.18	-0.14	-0.14	-0.16	-0.18	-0.12	-0.16	-0.12	-0.18
<i>S</i>	<i>S</i>	-0.44	-0.35	-0.35	-0.39	-0.45	-0.28	-0.39	-0.28	-0.45
<i>S</i>	<i>S</i>	-0.61	-0.49	-0.49	-0.54	-0.62	-0.39	-0.54	-0.39	-0.62
<i>U</i>	<i>U</i>	-0.75	-0.60	-0.60	-0.66	-0.76	-0.49	-0.66	-0.49	-0.76

Such a correlation between the  $C_{mn}$  coefficients and the stability behavior, observed both via the ROM and SIMULATE-3/3K analyses, is very valuable as a means of estimating the stability characteristics of a given core without the need to perform full three-dimensional time-dependent calculations. A more careful estimation of this behavior is presented in the following section, where a quantitative evaluation of the stability of the system in terms of the DR as a function of the  $C_{mn}$  coefficients is performed.

## 5.2 Quantitative analysis of the stability properties as a function of $C_{mn}$ coefficients.

### 5.2.1 Dependence of the decay ratio on the reactivity coefficients ( $C_{mn}$ coefficients)

The ROM, developed and described earlier in Section 2, is applied to more carefully expedite the dependence between the DR and the coupling reactivity coefficients  $C_{mn}$ . A number of different cases where the  $C_{mn}$  coefficients were manually modified are analyzed. For each case studied, the DR corresponding to the fundamental mode is numerically estimated [26,31]. The corresponding dependence of the DR on the  $C_{mn}$  coefficients is shown in Fig. 5.1

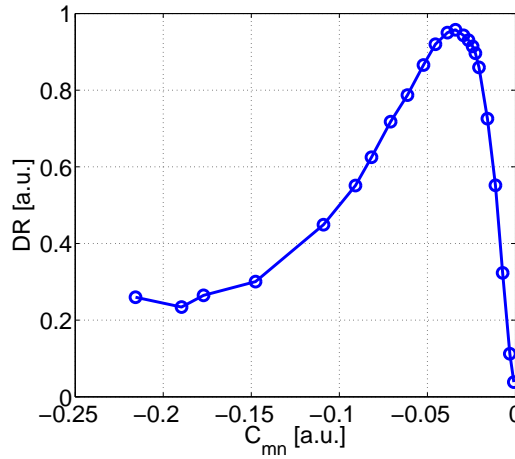


Figure 5.1: Dependence of the Decay Ratio on the reactivity  $C_{mn}$  coefficients.

As Fig. 5.1 demonstrates, the dependence between the DR and the  $C_{mn}$  coefficients is not monotonic over the whole range of the  $C_{mn}$ -coefficients. First the DR increases with increasing amplitude of the  $C_{mn}$  coefficient (following a conventional behavior of the DR), whereas at approximately  $C_{mn} = -0.0361$  a.u., the DR suddenly starts to decrease approaching a low-value region at around  $C_{mn} = -0.2$  a.u.

### 5.2.2 Estimation of the dynamical properties of the system (amplitude, phase, frequency and decay ratio)

To provide some insight into the origins of the sudden drop in the DR curve, a curve-fitting procedure is applied to all physical quantities available from the ROM, where it is assumed that the behavior of a BWR can be described as a second-order decaying oscillator, i.e. fitted to the following decaying sine-function:

$$\phi(t) = A \exp(-\gamma t) \sin(\omega t + \varphi) \quad (5.1)$$

Such a curve-fitting procedure is applied to the time-signals generated for four given configurations, i.e. for four different sets of  $C_{mn}$  values, thus providing information about

## 5.2. Quantitative analysis of the stability properties as a function of $C_{mn}$ coefficients.

the amplitude  $A$ , frequency  $\omega$ , decay constant  $\gamma$  and phase  $\varphi$  of some key parameters, i.e. void fraction  $\alpha$ , averaged surface fuel temperature  $T_{fs}$ , power  $P$  and inlet pressure drop  $\delta P_{inlet}$ . The corresponding results (except for the phase) are shown in Figs. 5.2, respectively.

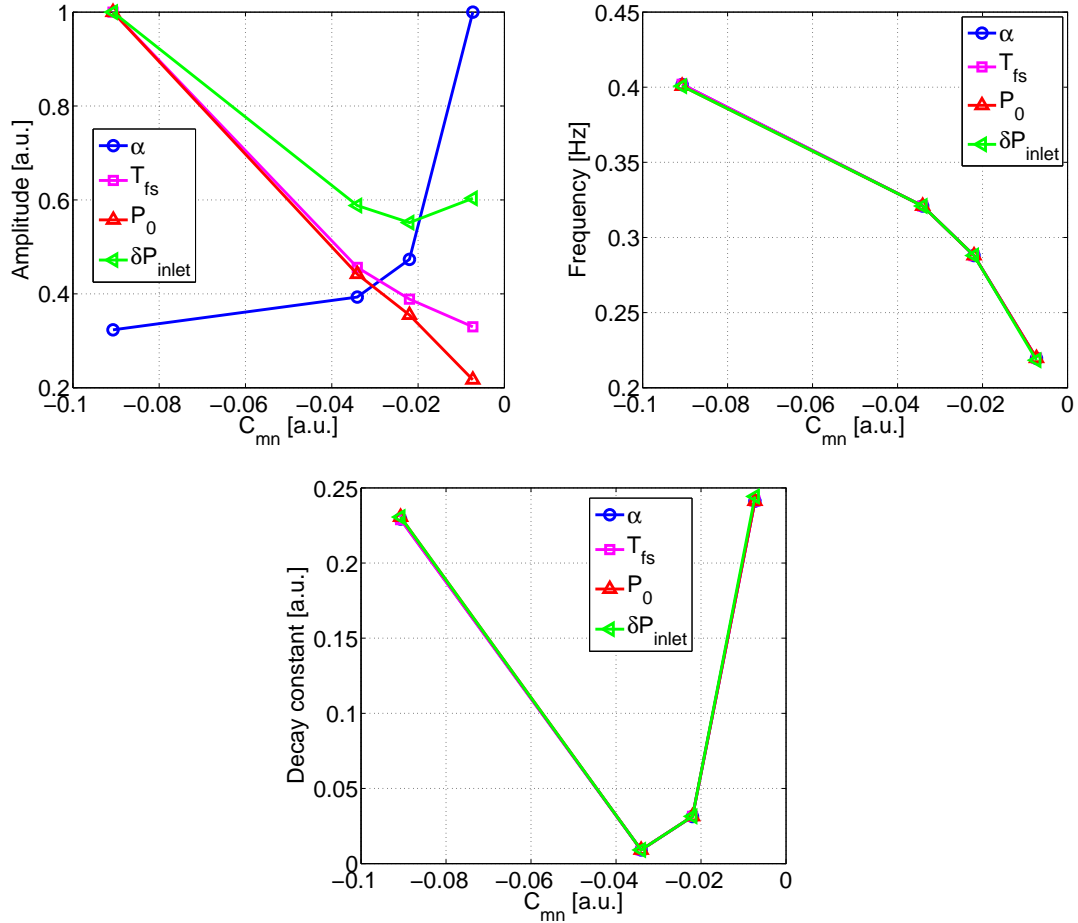


**Figure 5.2:** Dependence of the amplitudes  $A$ , frequency  $\omega$  and decay constant  $\gamma$  of the void fraction  $\alpha$ , averaged surface fuel temperature  $T_{fs}$ , power  $P$  and inlet pressure drop  $\delta P_{inlet}$  on the  $C_{mn}$  coefficients; for the amplitude, all the quantities were weighted to their corresponding maximum values.

A careful analysis of the upper left part of Fig. 5.2 shows that, as the  $C_{mn}$  coefficients decrease down to  $-0.0341$  a.u., the amplitude change in the void oscillations and the power oscillations is significantly larger compared with the ones in the surface fuel temperature and the inlet pressure drop oscillations. This leads to the conclusion that most of the produced fuel heat is transferred into the change of the void fraction. However, for  $C_{mn}$  values between  $-0.034$  a.u. and  $-0.0907$  a.u., the situation is reversed, namely the amplitudes of the surface fuel temperature as well as the inlet pressure drop oscillations experience a drastic jump whereas the amplitude of the oscillations in the void fraction do not change so much.

Such a peculiar behavior of the quantities can be interpreted as if all the heat from

the fuel is converted into an increase of the amplitudes of the surface fuel temperature and the inlet pressure drop oscillations, leaving the void change mostly unaffected. The increase in the amplitude of the inlet pressure drop oscillations apparently stabilizes the system (due to the phase delay between the power change and the feedback which becomes closer to  $-180^\circ$ ) and thus contributes to the decrease in the DR. Such an unexpected transition of the energy transfer from the void change into the surface fuel temperature/inlet pressure drop change can be explained by the inertia of the heat transferred between the fuel and the coolant (i.e. the time for the heat to be transferred from the fuel to the coolant) leading to some time delay between the change in the power and the corresponding change in the feedback.

One can also show that for the last two cases, i.e.  $C_{mn} = -0.034$  a.u. and  $C_{mn} = -0.0907$  a.u., the characteristic time of the power oscillations is less than the time it takes for the system to transfer heat from the fuel to the coolant. As a result, for a certain critical value (in our case  $C_{mn} = -0.036$  a.u.), the changes in the power (which frequency is a function of  $C_{mn}$ ) become too fast for the system to be able to transfer all the heat into the coolant, but instead the energy oscillations are mostly transferred into changes in the surface fuel temperature and the inlet pressure drop. Such a phenomenon might then lead to an additional stabilization of the system and thus a decrease of the DR.

Thus, one can conclude that the dependence between the DR and the reactivity coefficients ( $C_{mn}$  coefficients) is not as trivial and monotonic as expected, i.e. the DR experiences some peculiar drop at a certain critical value of the  $C_{mn}$  coefficient. It can nevertheless be noticed that for typical values of the void reactivity coefficient, the  $C_{mn}$  are sufficiently negative, and a monotonic behavior between the DR and the absolute value of the  $C_{mn}$  coefficients can again be observed. For sufficiently negative values, it thus means that the DR increases for  $C_{mn}$  coefficients becoming more negative.

## CONCLUSIONS

This report presented the work performed at Chalmers University of Technology within NORTHNET and devoted to the investigation of BWR stability and ways of assessing the stability of such systems. The estimation of the stability of a nuclear core is usually performed using time-dependent three-dimensional neutron kinetic solvers possibly coupled to a thermal-hydraulic solver. Such state-of-the art approaches rely on complex models and input decks. Although these simulations lead to accurate and reliable results, they are computationally expensive, and most importantly they seldom allow getting physical insight into the mechanism driving a given instability. This project was thus aimed at developing an alternative approach based on ROM, in which the partial differential balance equations describing neutron transport, heat transfer, and fluid dynamics are replaced by sets of ordinary differential equations. The transformation of the balance equations is carried out by expanding the space- and time-dependent distributions of the relevant fields onto proper sets of functions describing the spatial dependence throughout the system. Because of the excitation of the fundamental and first azimuthal modes in case of global and regional oscillations, respectively, the functions of choice to perform the spatial expansion of the neutron flux are the eigenfunctions of the nuclear core.

The first part of the project was thus devoted to developing three-dimensional computational capabilities to estimate such eigenmodes using two-group diffusion theory. The corresponding tool, called CORE SIM, has the ability to not only estimate the eigenmodes and their adjoint functions for any heterogeneous core, but also to calculate the neutron noise induced by any type of perturbations directly expressed as fluctuations of the macroscopic cross-sections in the frequency domain.

The second part of the project was targeted at developing a ROM that has the ability to model global, regional, as well as local oscillations. The novelty of the work lies with the fact that a four heated channel model was created, and the ROM can thus handle regional oscillations where the two first azimuthal modes are excited. This is of particular interest for investigating the relative excitation of the two first azimuthal modes that might lead to a rotating neutral line delimiting the two lobes of the resulting spatial dependence. In addition, the ability of the model to simulate local oscillations and their effect on both the global and regional oscillations make the model unique. This ROM was thereafter used to investigate the possibility of deriving new stability indicators other than the classical DR. After careful examination of the governing equations in the neutron kinetic model of the ROM, it was found that the stability behavior of the system is entirely determined by the  $C_{mn}$  coefficients. Such coefficients define the effect of the variation of the void

fraction onto pairs of eigenmodes. ROM simulations clearly demonstrated that when such coefficients are positive, the system is unstable. This is explained by the fact that positive  $C_{mn}$  coefficients are only possible when the void reactivity feedback is positive, which leads to instabilities. In addition, and most importantly, it was also noticed that strongly negative  $C_{mn}$  coefficients also lead to unstable behavior. Such a behavior was also confirmed by SIMULATE-3K calculations.

A more detailed investigation of the relationship between the amplitude of the  $C_{mn}$  coefficients and the DR nevertheless demonstrated that a non-monotonic relationship seems to exist between the two. More explicitly, for  $C_{mn}$  coefficients becoming more negative but still being small in amplitudes, the DR first increases, and decreases, and finally increases again. This behavior might be explained by a stabilization of the system by an increase in pressure drops when the feedback becomes more negative. Such a phenomenon only exists for small variations of the void reactivity feedback.

This non-monotonic behavior of the DR on the amplitude of the  $C_{mn}$  coefficients is only present for a void reactivity feedback being only slightly negative. In most practical cases, and as the SIMULATE-3K calculations also confirm, the void reactivity feedback is sufficiently negative for this non-monotonic behavior to be completely shadowed. It thus means that the  $C_{mn}$  coefficients can be used to assess the stability of nuclear cores in a predictive manner, i.e. the calculations of the  $C_{mn}$  coefficients for two different core configurations allow assessing which of the two cores is the most stable. This is of prime importance for core design, when many core loadings have to be considered. The estimation of the  $C_{mn}$  coefficients only requires the computation of the eigenmodes of the corresponding cores, and no time-dependent simulations is required.

More systematic investigations on a variety of core loadings and designs would be necessary to confirm these findings.

# ACKNOWLEDGEMENTS

Drs. Carsten Lange and Dieter Hennig from the Technical University of Dresden, Germany and Prof. Imre Pázsit from Chalmers University of Technology, Sweden are acknowledged for useful discussions and comments about this work. The help and advices received from Drs. Lange and Hennig should be particularly underlined since those lead to the successful completion of the project. The support from Vattenfall Nuclear Fuel, Sweden, and in particular from Dr. Hongwu Cheng, for providing SIMULATE-3 data was very much appreciated.

We also extend our appreciation to the Nordic Thermal Hydraulic Network (NORTH-NET) for the financial support to this project [research contracts: 4500131026 (Forsmark Kraftgrupp AB), 581422-025 (Ringhals AB), SKI 2007/1588/200705015 (Swedish Radiation Safety Authority SSM-formerly the Swedish Nuclear Power Inspectorate), and SE 08-018 (Westinghouse Electric Sweden AB)].



# NOMENCLATURE

<b>ROM</b>	Reduced Order Model
<b>BWR</b>	Boiling Water Reactor
<b>DFM</b>	Drift Flux Model
<b>DR</b>	Decay Ratio
<b>DWO</b>	Density Wave Oscillation
<b>HEM</b>	Homogeneous Equilibrium Model
<b>ODE</b>	Ordinary Differential Equation
<b>PDE</b>	Partial Differential Equation



# References

- [1] Kruners M., "Analysis of instability event in Oskarshamn-3, Feb. 8, 1998, with SIMULATE-3K," *SKI Report 98:42*, Statens Kärnkraftinspektion (Swedish Nuclear Power Inspectorate), Stockholm, Sweden, 1998.
- [2] Oguma R., "Application of noise analysis for the study of core local instability at Forsmark-1," *SKI Report 97:42*, Statens Kärnkraftinspektion (Swedish Nuclear Power Inspectorate), Stockholm, Sweden, 1997.
- [3] Pázsit I., "Determination of reactor stability in case of dual oscillations," *Annals of Nuclear Energy*, **22** (6), pp. 377-387 (1995).
- [4] Karve A. A., "Nuclear-coupled thermal-hydraulic stability analysis of Boiling Water Reactors," *Ph.D. Dissertation*, Virginia University, USA, 1998.
- [5] Dokhane A., "BWR stability and bifurcation analysis using a novel Reduced Order Model and the system code RAMONA," *Ph.D. Dissertation*, EPFL, Switzerland, 2004.
- [6] Lange C. "Advanced nonlinear stability analysis of boiling water nuclear reactors," *PhD thesis*, TU Dresden, Germany, 2009.
- [7] Dykin V., "The effect of different perturbations on the stability analysis of Light Water Reactors," *Licentiate Dissertation*, Chalmers University of Technology, Sweden (2010).
- [8] Larsson V. and Demazière C., "Comparative study of 2-group P1 and diffusion theories for the calculation of the neutron noise in 1D 2-region systems," *Annals of Nuclear Energy*, **36** (10), pp. 1574-1587 (2009).
- [9] Lamarsh J. R. , "Introduction to nuclear reactor theory," *American Nuclear Society*, LaGrange Park, IL, USA, 2002.
- [10] Nakamura S., "Computational methods in engineering and science with applications to fluid dynamics and nuclear systems," *John Wiley & Sons, Inc.*, New York, NY, USA, 1977.
- [11] Demazière C., "Description of the models and algorithms used in the CORE SIM neutronic tool," CTH-NT-241 report, Chalmers University of Technology, Department of Applied Physics, Division of Nuclear Engineering, Gothenburg, Sweden (2011).

- [12] Davis T. A., "UMFPACK version 4.6 user guide," Department of Computer and Information Science and Engineering, University of Florida, Gainesville, FL, USA (2002).
- [13] Demazière C. and Pázsit I., "Power reactor noise," lecture notes, *Workshop on Neutron Fluctuations, Reactor Noise, and their Applications in Nuclear Reactors*, International Centre for Theoretical Physics, Trieste, Italy, September 22-26, 2008, International Atomic Energy Agency (2008).
- [14] Pázsit I. and Demazière C., "Noise techniques in nuclear systems," chapter in the *Handbook of Nuclear Engineering*, by Cacuci D. (Ed.), ISBN 978-0-387-98150-5, Springer, Vol. 3 (2010).
- [15] Arnoldi W.E., "The principle of minimized iterations in the solution of the matrix eigenvalue problem." *Quarterly of Applied Mathematics*, **9** (1), pp. 17-29 (1951).
- [16] Saad Y., "Iterative methods for sparse linear systems - Second edition," Society for Industrial and Applied Mathematics, Philadelphia, PA, USA (2003).
- [17] Zinzani F., Demazière C., and Sunde C., "Calculation of the eigenfunctions of the two-group neutron diffusion equation and application to modal decomposition of BWR instabilities," *Annals of Nuclear Energy*, **35** (11), pp. 2109-2125 (2008).
- [18] Anderson E., Bai Z., Bischof C., Blackford S., Demmel J., Dongarra J., Du Croz J., Greenbaum A., Hammarling S., McKenney A., and Sorensen D., "LAPACK user's guide," Third Edition, Society for Industrial and Applied Mathematics, Philadelphia, PA, USA (1999).
- [19] Ericsson T., personal communication, Chalmers University of Technology, Gothenburg, Sweden (2008).
- [20] Demazière C. and Sunde C., "Calculation of the eigenfunctions and corresponding eigenvalues of the two-group diffusion equation in heterogeneous systems," In: *Proceedings of the Joint International Topical Meeting on Mathematics & Computation and Supercomputing in Nuclear Applications (M & C + SNA 2007)*, Monterey, California, April 15-19, 2007, American Nuclear Society (2007).
- [21] Sunde C., Demazière C. and Pázsit I., "Calculation of the neutron noise induced by shell-mode core-barrel vibrations in a 1-D 2-group 2-region slab reactor model," *Nuclear Technology*, **154** (2), pp. 129-141 (2006).
- [22] Demazière C. and Pázsit I., "Numerical tools applied to power reactor noise analysis," *Progress in Nuclear Energy*, **51** (1), pp. 67-81 (2009).
- [23] Demazière C., "User's manual of the CORE SIM neutronic tool," CTH-NT-243 report, Chalmers University of Technology, Department of Applied Physics, Division of Nuclear Engineering, Gothenburg, Sweden (2011).
- [24] Todreas N. E. and Kazimi M. S., "Nuclear System I. Thermal-Hydraulic Fundamentals," *Hemisphere*, New York, NY, USA, 1990.

- 
- [25] Dykin V., Demazière C., Lange C. and Hennig D., "Investigation of global and regional BWR instabilities with a four heated-channel Reduced Order Model," *Annals of Nuclear Energy*, **53**, pp. 381-400 (2013).
- [26] Dykin V., Noise applications in Light Water Reactors with traveling perturbations, *PhD thesis*, CTH-NT-263, Chalmers University of Technology, Gothenburg, Sweden (2012).
- [27] Bell G. I. and Glasstone S., "Nuclear Reactor Theory," *Van Nostrand-Reinhold Company*, New York, USA, 1970.
- [28] Dykin V., Demazière C., Lange C. and Hennig D., "Investigation of local BWR instabilities with a four heated-channel Reduced Order Model," *Annals of Nuclear Energy*, **53**, pp. 320-330 (2013).
- [29] Demazière C. and Pázsit I., "On the possibility of the space-dependence of the stability indicator (decay ratio) of a BWR," *Annals of Nuclear Energy*, **32** (12), pp. 1305-1322 (2005).
- [30] Analytis G. Th., Hennig D., and Karlsson J. K.-H.. "The general mechanism of core-wide and local instabilities at the Forsmark-1 BWR," *Nuclear engineering and design*, **205** (1-2), pp. 91-105 (2001).
- [31] Dykin V., Demazière C. and Vinai P., "On the possible dependence of the Decay Ratio on the void reactivity feedback," *Transactions of the American Nuclear Society*, **107**, San Diego, CA, USA, November 11-15, 2012 (2012).